THE A-DEPENDENCE OF LEADING PARTICLE PRODUCTION BY 800 GeV PROTONS*

A Dissertation Presented

by

Ioanis Kourbanis

to

The Department of Physics

in partial fulfillment of the requirements

for the degree of

Doctor of Philosophy

in the field of

Physics

Northeastern University

Boston, Massachusetts

December 1989

* Work supported in part by the National Science Foundation

NORTHEASTERN UNIVERSITY

Graduate School of Arts and Sciences

Dissertation Title: The A-dependence of Leading Particle Production by 800 GeV protons

Author: Ioanis Kourbanis

Department: Physics

Approved for Thesis Requirements of Doctor of Philosophy Degree

David Garelick	12/11/89
William Faissler	12/11/89
Toman Taylor	12/11/89
G. Alverson	11 Dec 89
Thesis Commitee	Date
S. Reucroft	11 Dec. 1989.
Head of Department	Date

Graduate School Notified of Acceptance

Dean	Date

Copy Deposited in Library

Signed	Date

NORTHEASTERN UNIVERSITY

Graduate School of Arts and Sciences

Dissertation Title: The A-dependence of Leading Particle Production by 800 GeV protons.

Author: Ioanis Kourbanis

Department: Physics

Approved for Thesis Requirements of Doctor of Philosophy Degree

David Garelick	12/11/89
William Faissler	12/11/89
Tomas Taylor	12/11/89
G. Alverson	11-Dec-89
Thesis Commitee	Date
S. Reucroft	11 Dec. 1989.
Head of Department	Date

ABSTRACT

We have measured the production of secondary particles in collisions of 800 GeV protons with various nuclei. Previous experiments have measured leading particle production by protons up to 400 GeV. A differential Cherenkov counter was used to tag the secondary particles as pions, kaons, protons or antiprotons. Target nuclei used were beryllium, aluminum and tungsten. Most of this production data were taken at ±530 GeV, although a small amount was also obtained at -200GeV and at -400 GeV. Negative particle data were taken at a production angle of θ=0 mrad; positive data were taken at θ=1.4 mrad. Angular acceptance was typically $\delta\theta = \pm 0.5$ mrad. The tuning, the performance and the characteristics of the new Fermilab MW-beamline which was used in this study are discussed. The differential Cherenkov counter is also described along with its use to tag the minority particles. Finally the results on yields and A-dependence are presented along with a comparison with the existing data from other experiments and the predictions of current theoretical models.

To the Memory of my Father

Αναστασιος Κουρμπανις

Acknowledgments

I would like to take this opportunity to thank all the E706 collaborators for their work and their participation in the experiment. There some people who I would like to thank them by name.

First I would to thank Dr. W. Baker, and Dr. C. Johnstone from Fermilab without whom this work would have not been possible. They were both my second advisors during my stay at Fermilab. I am greatfully indebted to both of them and I am looking forward to working with them again in the near future.

I would like also to thank my advisor Professor D. Garelick who first introduced me to high Energy Physics, for his support, encouragement, advice and help through out my graduate carrier. His comments and suggestions on my thesis were really invaluable. I thank also Professor M. Glaubman of Northeastern for his support and valuable advice during my stay at Fermilab. Many thanks also to Northeastern Professors W. Faissler and G. Alverson for their help and their comments on my thesis.

I would like to thank all my fellow graduate students and postdocs whose hard work and enthusiasm turned E706 from nice drawings into a successful experiment. Special thanks to Alecos Sinanidis and his wife Eleni for their frienship and all the good and hard moments we shared together. Thanks also to Dr. George Fanourakis and his wife Penelope for their frienship, hospitality, support and advice since my first day at Fermilab. Thanks also to Dr. Takahiro (Taka) Yasuda, and Armando Lanaro for their frienship and for the useful discussions we had together.

I also have to acknowledge the help of the Fermilab Technical personnel of Lab 6 and Lab 8 for their invaluable help in building the hadron and the EM calorimeter. Special thanks to B. Koecker who was also eager to help me and had an good advice in every technical matter. Many thanks to J. Tweed for his beautiful job in the Cherenkov gas system and for his help in the Cherenkov control system. Many thanks also to Dr.

D. Carey and R. Tokarek of Fermilab for the many useful discussions on beamlines and beam optics.

Finally, I would like to thank my mother Efrossini and my sister Vasso, for their love, encouragement and support during all my years in the States.

Table of Contents

1. INTRODUCTION 1
2. MW-BEAMLINE AND E-706 SPECTROMETER 12
   2.1 MW-Beamline 12
   2.2 E-706 Spectrometer 24
   2.3 Modes of operation 31
3. MW-BEAMLINE STUDIES AND PARTICLE YIELDS . . . 37
   3.1 Beam Optics 37
   3.2 First-Order Matrix Formalism 42
   3.3 Magnetic Elements 47
   3.4 Computer analysis and Design Considerations 57
   3.5 Particle Yields 69
   3.6 Absolute Beam Momentum 77
4. MW-CHERENKOV COUNTER 81
   4.1 Introduction 81
   4.2 Performance Characteristics of a Cherenkov Counter . . 86
   4.3 The MW Cherenkov Detector 96
   4.4 Monte Carlo Simulation and Counter Performance . . 117
5. PARTICLE PRODUCTION DATA ANALYSIS 137
   5.1 Introduction 137
   5.2 Beam Momentum 138
   5.3 Acceptance Calculations 140
   5.4 Background Subtraction 141
   5.5 Particle Decays and Absorption in the Beam 143
   5.6 Muon and Electron Contamination 144
   5.7 Accidental Coincidences 147
   5.8 Target Thickness Correction 147
   5.9 SEM Calibration 149
   5.10 Estimation of Particle Ratios 157
6. RESULTS AND CONCLUSIONS 159

6.1 Calculations of Cross Sections 159
6.2 Systematic Errors 160
6.3 Cross Sections at -200 and -400 GeV 161
6.4 Cross Sections at ±530 GeV 162
6.5 Energy Dependence 164
6.6 A-Dependence 164
6.7 Conclusions 173

LIST OF FIGURES

1) Hadron Nucleus Collision as viewed in the rest frame particle groups for three different cases (target is indicated at the right and the beam projectile at the left in these figures.): (top): Beam fragmentation region. (middle): Central region. (bottom): Target fragmentation region. (5)

2) Diagrams of proton-nucleus interactions with two projectile collisions in the Additive Quark Model (top) and in the Dual Parton Model (bottom).(9)

3) (top): R(y) is the ratio of the cross-section on the nuclear target to that of hydrogen. Comparison of streamer chamber data with additive quark model calculations (from Busza[3]). . (bottom): Comparison of data of Barton et al.[24] for the differential multiplicities for $\pi^{\pm}$ production with the dual parton model calculations[10]. (10)

4) MW Beamline Components plotted in horizontal position versus longitudinal position. (17)

5) Beamline component symbols. (18)

6) (top): MW Beamline components in the different enclosures. (bottom): The spill cycle. (22)

7) (top): Zero production angle for the MW Primary target. (bottom): Non zero production angle for the MW Primary target. (25)

8) (top): Layout of the MW spectrometer. (bottom): Layout of the Silicon Strip Detector. (27)

9) (top): A view of the electromagnetic calorimeter. (bottom): a) A view of one of the readout planes in the Hadron calorimeter. b) The structure of a

---

The page where the figure can be found in the text is indicated in parenthesis at the end of the figure listings.

cookie. (29)

10) (top): The overall gantry and cryostat of the LAC. The beam is incident from the left. (bottom): View of the Forward Calorimeter. (30)

11) Run numbers during the second calibration run, superimposed in the front face of the LAC. (35)

12) Curvilinear coordinate system used in derivation of the equation of motion[46]. (39)

13) (top): Dimensions of a two-dimensional phase space ellipse in terms of ellipse matrix elements. (bottom): The two-dimensional ellipse (a) after traversing a drift space becomes ellipse (b). (47)

14) (top): Dipole magnet cross section showing **B** and **Force** components and the central trajectory coordinates. (bottom): Charged particle path in the bending plane of a dipole magnet. (50)

15) MW secondary beam bend points. (51)

16) (top): Cross sectional configuration of a quadrupole magnet showing the **B** components (top), and the **Force** components (bottom). (53)

17) (top): Unsymmetric focusing by a quadrupole doublet. (middle): Point-to-point focusing with a quadrupole doublet. (bottom): Point-to-parallel focusing with a quadrupole doublet(all from Sedman[56]) (56)

18) R_{12}, R_{34} matrix for the MW-beamline plotted versus the longitudinal distance s along the beamline. (60)

19) R_{16} matrix element for the MW-beamline plotted versus the longitudinal distance s along the beamline. (61)

20) $\sqrt{\sigma_{11}}$ and $\sqrt{\sigma_{33}}$ matrix elements for the MW-beamline plotted versus the longitudinal distance s along the beamline. (62)

21) Profile of the Primary 800 GeV proton beam before the MW-Primary target. (top): Horizontal plane. (bottom): Vertical plane. (64)

22) Beam profiles at the experimental target for the negative running mode. (top): TURTLE calculations. (bottom): SSD profiles. (65)

23) Beam profiles at the experimental target for the positive running mode. (top): TURTLE calculations. (bottom): SSD profiles. (66)

24) Beam momentum distribution for the negative running mode calculated by TURTLE. (67)

25) Beam momentum distribution for the positive running mode calculated by TURTLE. (68)

26) Berylium target production efficiency f versus L/λ_s. (72)

27) Calculated particle yields for the MW-Beamline (3/4 interaction length Al target), normalized to E706 measurements at 530 GeV. (75)

28) (top): Energy deposited in the whole calorimeter for the 50 GeV calibration run. (bottom): Energy deposited in the electromagnetic calorimeter for the 50 GeV calibration run. (77)

29) (top): Energy deposited in the whole calorimeter for the 100 GeV calibration run. (bottom): Energy deposited in the electromagnetic calorimeter for the 100 GeV calibration run. (78)

30) (top): Energy deposited in the whole calorimeter for the 200 GeV calibration run. (bottom): Energy deposited in the electromagnetic calorimeter for the

200 GeV calibration run. (79)

31) Basic Types of Cherenkov Detectors. (84)

32) MW Cherenkov Counter. (98)

33) The Cherenkov Counter Gas System. (102)

34) Parts of the Conical Reflector. (top): Main cylinder. (bottom): Cylindrical Cap. (104)

35) A partial cross section of the Conical Reflector assembly. (105)

36) Optical Transmission of the Ultrasil Windows. (113)

37) Quantum Efficiency versus Wavelength for the HAMAMATSU R1332X Phototubes. (114)

38) Cherenkov Trigger Logic. (116)

39) Pressure Curve at -200 GeV. (118)

40) Pressure Curve at -400 GeV. (119)

41) Pressure Curve at -530 GeV. (120)

42) Pressure Curve at 530 GeV. (121)

43) Effect of the beam divergence on the resolution of the Cherenkov counter at -530 GeV. Solid line: Perfect counter. Dashed line: Counter with only beam divergence (0.025 mrad). (123)

44) Effect of the beam momentum bite on the resolution of the Cherenkov counter. Solid line: Perfect counter. Dashed line: Counter with 10%(FWHM) momentum bite. (124)

45) Effect of the chromatic dispersion on the resolution of the Cherenkov counter.

Solid line: Perfect counter. Dashed line: Counter with only chromatic dispersion. (125)

46) Comparison of the Monte Carlo pressure curve to the experimental data one at -530 GeV for the 3/4 interaction length Al target and the $D5\overline{V2}$ coincidence level. (126)

47) Comparison of the Monte Carlo pressure curve to the experimental data one at 530 GeV for the 3/4 interaction length Al target and the $D5\overline{V2}$ coincidence level. (127)

48) Effect of the accepted wavelength range on the resolution of the Cherenkov counter at -530 GeV. Solid line: 300-600 nm Dashed line: 220-600 nm. (129)

49) Comparison of the Monte Carlo pressure curve to the experimental data one at -530 GeV for the 3/4 interaction length Al target and the $D4\overline{V2}$ coincidence level. (130)

50) π^- contamination under the K^- peak at -530 GeV for the 3/4 interaction Al target and the $D4\overline{V2}$ coincidence level. (131)

51) Comparison of the Monte Carlo pressure curve to the experimental data one at 530 GeV for the 3/4 interaction length Al target and the $D3\overline{V2}$ coincidence level. (133)

52) K^+ contamination under the π^+ peak at 530 GeV for the 3/4 int. length Al target and the $D3\overline{V2}$ coincidence level. (134)

53) p contamination under the π^+ peak at 530 GeV for the 3/4 int. Al target and the $D3\overline{V2}$ coincidence level. (135)

54) Typical target scan. (142)

55) Monte Carlo fit for the $D5\overline{V2}$ Be pressure curve at -530 GeV. (151)

56) Monte Carlo fit for the $D5\overline{V2}$ Al pressure curve at -530 GeV. (152)

57) Monte Carlo fit for the $D5\overline{V2}$ W pressure curve at -530 GeV. (153)

58) Monte Carlo fit for the $D5\overline{V2}$ Be pressure curve at 530 GeV. (154)

59) Monte Carlo fit for the $D5\overline{V2}$ Al pressure curve at 530 GeV. (155)

60) Monte Carlo fit for the $D5\overline{V2}$ W pressure curve at 530 GeV. (156)

61) The invariant differential cross section for p $A \rightarrow \pi^-$ X plotted as a function of x_F (165)

62) The invariant differential cross section for p $A \rightarrow K^-$ X plotted as a function of x_F (166)

63) The invariant differential cross section for p $A \rightarrow \bar{p}$ X plotted as a function of x_F (167)

64) The measured invariant differential cross sections for p Al$\rightarrow \pi^-$ X compared with the ones from Barton et al.[24] at 100 GeV for various values of x_F. (168)

65) The measured invariant differential cross sections for p Al$\rightarrow K^-$ X compared with the ones from Barton et al.[24] at 100 GeV for various values of x_F. (169)

66) The measured invariant differential cross sections for p Al$\rightarrow \bar{p}$ X compared with the ones from Barton et al.[24] at 100 GeV for various values of x_F. (170)

67) Particle ratios for Al as a function of the secondary momentum. (171)

68) Particle ratios of W as a function of the secondary momentum. (172)

69) Invariant differential cross sections for negative particles with fits of the form

$\sigma_0 A^\alpha$. (174)

70) Invariant differential cross sections for positive particles with fits of the form $\sigma_0 A^\alpha$. (175)

71) A-dependence: π^-, π^+ production. The middle thick line represents the theoretical prediction of additive quark model. The upper and lower thin lines represent the theoretical predictions with two different sets of input parameters. (176)

72) A-dependence: K^-, K^+ production The middle thick line represents the theoretical prediction of additive quark model. The upper and lower thin lines represent the theoretical predictions with two different sets of input parameters. (177)

73) A-dependence: p, $\bar{p}$ production The middle thick line represents the theoretical prediction of additive quark model. The upper and lower thin lines represent the theoretical predictions with two different sets of input parameters. (178)

LIST OF TABLES

1: MW Beamsheet. (14)

2: Negative particle yields for 10^{12} incident 800 GeV primary protons on the 3/4 interaction length Al target. (73)

3: Positive particle yields for 10^{12} incident 800 GeV primary protons on the 3/4 interaction length Al target. (74)

4: Electron yields for 10^{12} incident primary 800 GeV protons on the 3/4 interaction length Al target. (74)

5: Quoted and calculated values of the beam momentum. (80)

6: Values of the parameter ν for some commonly used gas radiators. (90)

7: Performance characteristics of the MW-Cherenkov counter at 530 GeV. (99)

8: Variation of the index of refraction of He and the Cherenkov angle of different 700 GeV particles with the wavelength. The index of refraction of He was calculated at a pressure of 5.54 psi and at 20°. (109)

9: Variation of the index of refraction of He and the Cherenkov angle of different 530 GeV particles with the wavelength. The index of refraction of He was calculated at a pressure of 5.55 psi and at 20°. (110)

10: Variation of the index of refraction of He and the Cherenkov angle of different 530 GeV particles with the wavelength. The index of refraction of He was calculated at a pressure of 5.86 psi and at 20°. (111)

11: Physical Dimensions of the various targets used for the particle production data. (137)

12: Beam momentum values. (139)

The page where the table can be found in the text is indicated in parenthesis at the end of the table listings.

13: Collimator openings and acceptances for the various beam configurations used. (141)

14: Measured background at each beam momentum. (143)

15: Probability for the πs and Ks to reach the end of the Cherenkov counter. (144)

16: Material at the MW-beamline up to the end of the Cherenkov counter, expressed as a fraction of the proton nuclear interaction length λ_I and the radiation length L_R. (145)

17: Percentange of electrons and muons in the beam for the different beam momenta. (146)

18: Production efficiencies for the different production targets and secondary particles. (148)

19: Positive particle contents of the beam for various targets at 530 GeV. (150)

20: Negative particle contents of the beam for the different targets and momenta. (150)

21: Values of $A/\rho l N_0$ for each target. (160)

22: Calculated invariant differential cross sections for Al and W at -200 and -400 GeV. (161)

23: Particle ratios for Al and W at -200 and -400 GeV. (162)

24: Particle ratios at -530 GeV. (162)

25: Particle ratios at 530 GeV. (163)

26: Invariant cross sections at 530 GeV. (163)

27: Invariant cross sections at -530 GeV. (163)

28: Parameters obtained by fitting the invariant differential cross sections to the form $\sigma_0 A^\alpha$ (173)

1. INTRODUCTION

For many years it has been realized that studying hadron-nucleus collisions at high energies provides important and unique insights into strong interaction physics[1],[2]. Due to intranuclear rescatterings, the nucleus is the only tool available for the experimental study of: the space-time development of particle production; the interaction of resonances with nucleons; and the interactions of 'almost' free quarks.

In this introduction I will discuss an intuitive picture of the hadron-nucleus interaction due to Busza[3] and then give a review of the theoretical models and recent experiments closely related to my thesis work. I first start by defining a few parameters which are extensively used in the hadron-nucleus literature and which are very useful in interpreting the data.

A measure of the average multiplication of particles inside a nucleus is given by:

$$R_A = \frac{< n >_A}{< n >_p} \tag{1.1}$$

where $< n >_A$ is the average number of charged relativistic particles ($\beta \geq 0.7$) produced in an inelastic incoherent interaction between a hadron and nucleus A. $< n >_p$ is the average number of charged particles produced in an inelastic collision of the same hadron with a proton.

A parameter that reflects the nuclear thickness, and at the same time takes

account the differing opacities for different incident hadrons (h) is $\bar{\nu}$, defined as:

$$\bar{\nu} = \frac{A\sigma_{hp(inelastic)}}{\sigma_{hA(inelastic)}} \tag{1.2}$$

$\bar{\nu}$ can be thought of as the average number of inelastic collisions h would make with nucleons in the nucleus if, following each collision, it remained as a single hadron h. From experimental measurements it turns out that:

For protons[20]:

$$\bar{\nu} \simeq 0.7A^{0.31} \tag{1.3}$$

For pions[20]:

$$\bar{\nu} \simeq 0.74A^{0.25} \tag{1.4}$$

in agreement with a naive nucleus model with large A and radius $R \sim A^{1/3}$.

A convenient parameter for describing the longitudinal motion of relativistic particles is the rapidity, y, defined in any frame by:

$$y = \frac{1}{2}\ln\frac{E + p_{\|}}{E - p_{\|}} \tag{1.5}$$

where E is the total energy of the particle and $p_{\|}$ its longitudinal momentum in that frame. A Lorentz transformation to another frame traveling with speed $v = \beta c$ along the rapidity axis corresponds to a rapidity y^*, in the new frame:

$$y^* = y - \frac{1}{2}\ln\frac{(1+\beta)}{(1-\beta)} \tag{1.6}$$

Thus, the shape of a rapidity distribution will be invariant under such a parallel Lorentz boost.

In some experiments on particle production, only laboratory angles are measured. In those cases the pseudorapidity variable η is used:

$$y^{lab} \simeq \eta^{lab} = -\ln(\tan\theta_{lab}/2) \tag{1.7}$$

The approximation is excellent provided:

$$\frac{p - p_{\|}}{E - p_{\|}} \simeq 1. \tag{1.8}$$

One way to look at hadron-nucleus interactions is to consider the interactions as viewed in the rest frames associated with the groups of particles produced[3]. We consider three cases: 1) the secondaries have rapidity near that of the beam projectile (within ± 1.5 units); 2) the secondaries are at rest in the center of mass of the projectile and the target (rapidity far from either projectile or target) and; 3) the secondaries have rapidity close to that of the nucleons in the target nucleus. In the first case, since the beam particle rapidity is close to that of the reference frame, the beam particle is moving very slowly. The target nucleus however is far away in rapidity, moving very quickly through the interaction and is highly Lorentz contracted (Fig. 1(top)). In this figure, each line represents a contracted nucleon in the nucleus, and the circle represents the beam particle. The secondaries in this region will be "produced" at a time after the nucleus has passed through the beam particle and hence will not have the chance to interact in the nucleus. However, the secondaries can recombine with pieces of the beam particle since these fragments move slowly in this frame. Another way to describe this case is that the formation length, increases with momentum[4]. At high energy the formation length is greater than the absorption length or even the radius of the

nucleus. The beam particle, unlike the secondaries, itself can interact repeatedly with different nucleons. In this rapidity region we observe, first, secondaries which could not have reinteracted in the nucleus, and, second, fast beam fragments. This rapidity range is called the leading particle or beam fragmentation region. The measurements made for my thesis work are in this kinematic region.

In the second case, secondaries are at rest in the center of mass system. Both the beam and the target are highly Lorentz contracted and move rapidly through the interaction (Fig. 1(middle)). Secondaries produced in this rapidity region will recombine without reinteracting. Also, there will be no beam or target fragments to help the hadronization. Particles produced in this rapidity region, called the central or central field region, should not depend on the beam or target type but only on the amount of energy left by the fields of the passing beam and target.

In the third case, the nucleus has rapidity close to that of the reference frame and will be moving slowly while the beam particle will be highly contracted (Fig. 1(bottom)). Secondaries produced in this rapidity region will be formed inside the nucleus. They will have the chance to interact with other nucleons before leaving the nucleus, each interaction producing slow secondaries which can themselves interact. Thus, the presence of these particles can lead to a cascade of interactions that will depend on the size of the nucleus and somewhat on the impact parameter of the original hadron-nucleus interaction. This rapidity region, called the target fragmentation region, contains slow particles, most of which come from secondary interactions inside the nucleus.

The discussion above emphasizes the important distinction between projectile and secondary collisions inside the nucleus. A projectile collision is an interaction

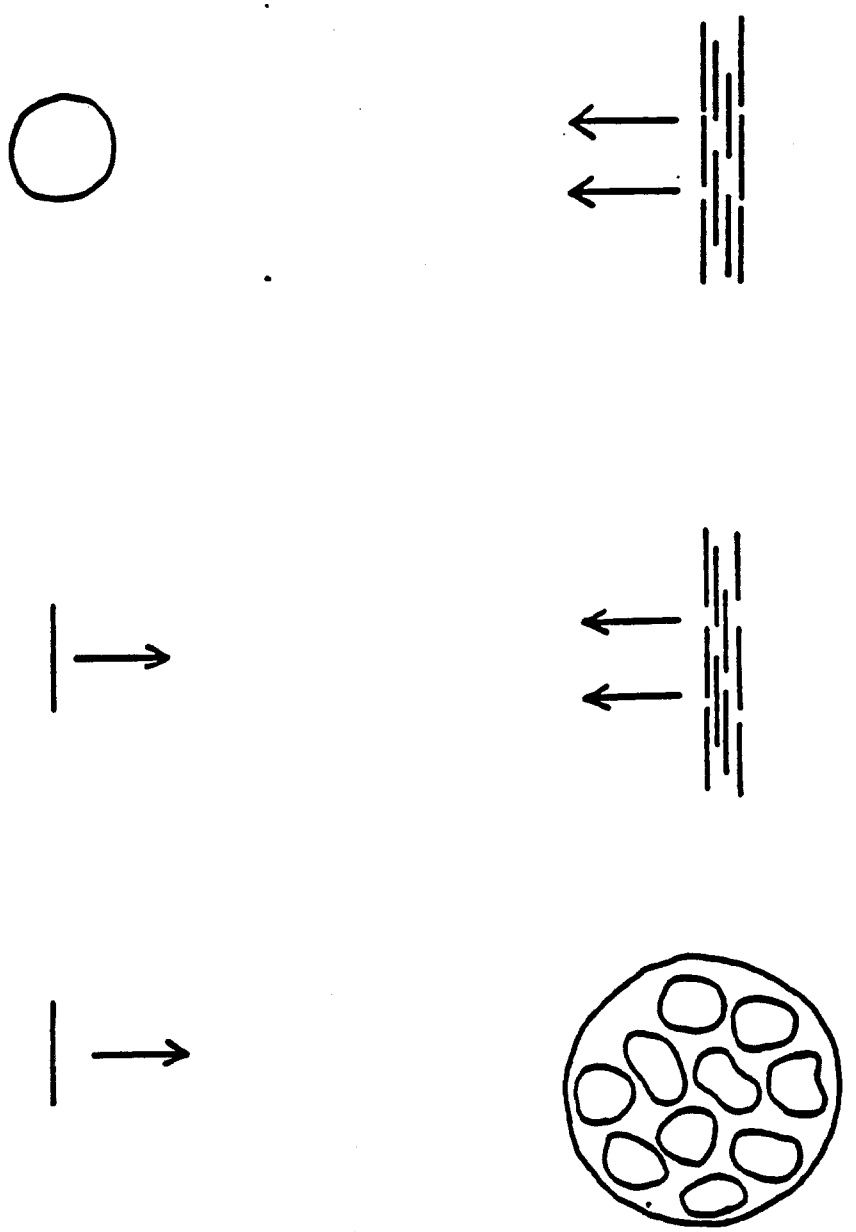

Figure 1: Hadron Nucleus Collision as viewed in the rest frame particle groups for three different cases: (target is indicated at the right and the beam projectile at the right in these figures.) a) Beam fragmentation region. (middle): Central region. (bottom): Target fragmentation region.

between the incident beam particle and a nucleon in the nucleus; the projectile may collide with more than one nucleon and in general it does. The number of projectile collisions is a measure of the thickness of the nucleus along the line of the interaction. The impact parameter is related to the number of the projectile collisions. A small impact parameter means that the beam interacted near the center of the nucleus and so statistically will have the maximum number of projectile collisions. In projectile collisions, the difference in rapidity between the projectile and target is large. Secondary collisions usually occur when a particle produced in a projectile collision has rapidity close to that of the target so that it is formed inside the nucleus and then interacts before leaving.

Theories of hadron-nucleus interactions may be grouped into general categories depending on how they treat the projectile collisions. Collective models[5],[6] treat the interaction as having only one collision between the incoming hadron and some "effective target" which depends on how many nucleons were struck in the nucleus. Finally there are models which treat the collisions explicitly as quark-quark (or parton-parton) interactions.

The collective models arrive at predictions without specifying any dynamical properties of the hadrons and most of the times don't agree with the data. Thus, I will concentrate in describing two parton models that offer the hope of a complete description of hadron-nucleus interactions based on the "Standard Model"[7].

The additive quark model of Nikolaev and Ostapcheck[8] and the dual parton model of Capella and Tran Thanh Van[9] [10] are both based on interactions between single partons in the beam particle with single partons in the target nucleus (see Fig. 2 (top)). The additive quark model views a hadron, h, as consisting of a

definite number of spatially separated constituent quarks, whose flavour quantum numbers are the same as those of the corresponding valence quarks[11]. The sea quarks, sea antiquarks and gluons form a virtual cloud of a constituent quark. In any of hadron-hadron, hadron-nucleus or nucleus-nucleus collision, some quarks from the projectile interact inelastically with quarks from the target losing a considerable fraction of their initial momenta. The remaining quarks in both the projectile and the target pass through as the leading or spectator quarks, retaining their initial momenta. The hadronization process can be broken into steps which have different characteristic lengths. First, new quarks will be formed with probabilities described by the fragmentations functions that depend both on the quarks in the collision and the spectator quarks. Second, the quarks recombine to form hadrons. The characteristic length for the second process is long compared to that of the first, so the two are treated separately. The formation length for the quarks, as was discussed earlier, may be longer or shorter than the nucleus depending on the momentum of the quark being produced. In this model each quark in the projectile may only interact once in the nucleus. The hadrons produced in the projectile fragmentation region are dominated by the products of the hadronization (fragmentation and recombination) of the leading quarks from the projectile. The additive quark model was developed further by many people[12],[14],[14],[16] and can explain most of the features of hadron-hadron and hadron-nucleus collisions data. In the last chapter of this thesis the additive quark model predictions as calculated by Dar and Takagi[12],[13], for the A-dependence of the inclusive reactions p+A$\rightarrow$ c+anything (c=$\pi^{\pm}$, $K^{\pm}$, p and $\bar{p}$) in the projectile fragmentation region, are compared with my data.

In the dual parton model (Fig. 2 (bottom)), as a consequence of the interaction

each colliding hadron splits into two colored systems, a quark and antiquark system (in the case of a meson) and quark and diquark systems (in the case of a baryon). Together these two systems carry all the momentum of the colliding hadrons. In a case of n inelastic collisions of the projectile with n nucleons of the target there will be 2n quark-antiquark chains and only two chains can be initiated by colored systems containing valence quarks of the projectile. The remaining 2n-2 chains will be initiated by quarks or antiquarks of the projectile sea.

The main difference between the additive and dual parton models, is indicated in Fig. 2 which shows a hadron-nucleus interaction with two projectile collisions in each model. Unlike the additive quark model, in the dual parton model the quark-antiquark chain between the projectile and target quarks appears twice (the outside chains). Each additional collision adds two more chains between a sea quark and the target and a sea antiquark and the target (the inside chains). Final particle rapidity distributions are formed by summing up the contributions from each chain. To do this one needs to know the momentum distribution of the end quarks in the chain. This requires knowing the distribution in the beam, target and sea, and the fragmentation function of quarks into hadrons. Some examples of the predictions of the dual parton model and the additive quark model, are compared with the data in Fig. 3. It should be mentioned that both models have sufficient flexibility to encompass most of the current data.

Many reviews of the experimental data on hadron-nucleus collisions have been published recently [3],[17],[18],[19],[20]. Previous experiments have measured leading particle production by protons up to 400 GeV [21],[22],[23],[24],[26]. Barton et. al.[24], measured the inclusive production of $\pi^{\pm}$, $K^{\pm}$, p and $\bar{p}$ in 100-GeV proton collisions

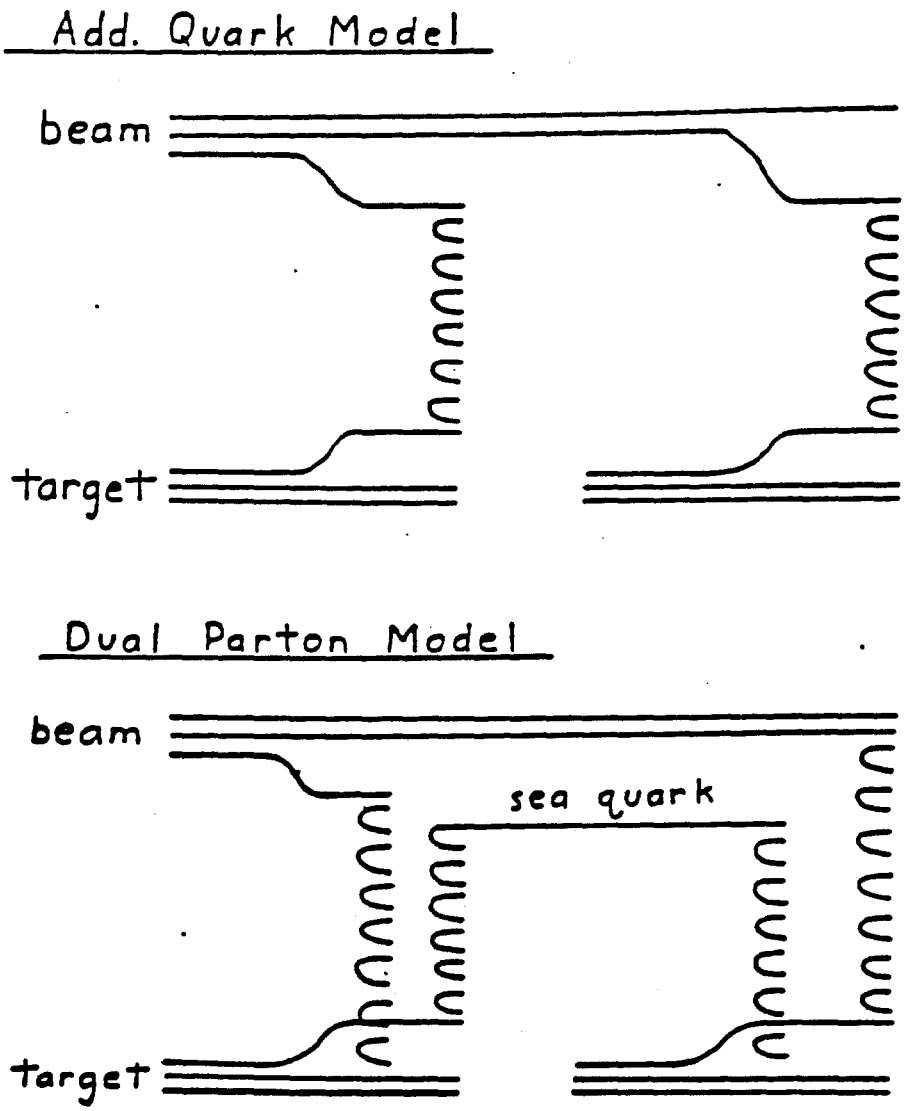

Figure 2: Diagrams of proton-nucleus interactions with two projectile collisions in the Additive Quark Model (top) and in the Dual Parton Model (bottom).

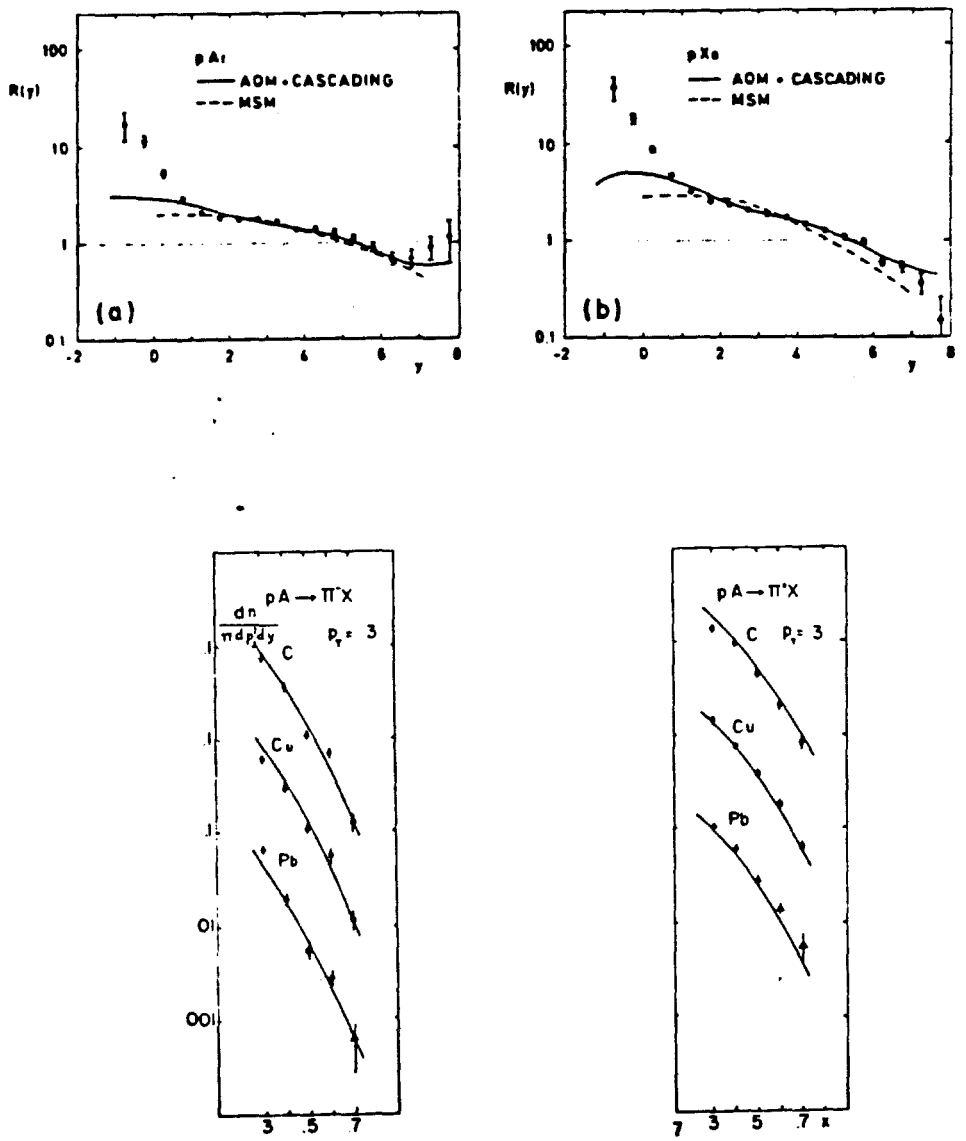

Figure 3: (top): R(y) is the ratio of the cross-section on the nuclear target to that of hydrogen. Comparison of streamer chamber data[25] with additive quark model calculations (from Busza[3]). (bottom): Comparison of data of Barton et al.[24] for the differential multiplicities for $\pi^{\pm}$ production with the dual parton model calculations[10].

with C, Al, Cu, Ag, and Pb targets and made a compilation of the world data on the A-dependence of leading particles produced in high energy proton collisions. We measured the inclusive leading particle production in 800-GeV proton collisions with Be, Al, and W. The last chapter of this thesis compares our results with other experiments. Except from the A-dependence of the inclusive cross-sections the hypothesis of limiting fragmentation[27] can be tested by comparing our incident proton data at 800 GeV with those of Barton et al.[24] at 100 GeV. According to this hypothesis, one expects the measured inclusive cross sections in the projectile fragmentation region to scale with energy, that is, to be functions of only the p_T and the Feynman x (x_F).

The parts of the E706 I was primarily involved with were: a) Construction of the hadronic part of the E706 Liquid Argon Calorimeter; b) Construction and operation of the differential beam Cherenkov counter; c) Bringing into operation, tuning and understanding the MW-beamline; d) Developing the Monte Carlo program to simulate the performance of the Cherenkov counter so to be able to separate π from K at 530 GeV; e) Acquisition of the data employed in this thesis; f) Analyzing the data for the A-dependence presented in this thesis.

2. MW-BEAMLINE AND E-706 SPECTROMETER

In this chapter I describe the MW-Beamline and the E-706 spectrometer. I also give an overview of the different modes of operation used in the beamline.

2.1. MW-BEAMLINE

The Meson West (MW) beamline is one of the newest fixed target beamlines at Fermilab. It is a reasonably high intensity secondary beamline with mass definition provided by a Cherenkov counter. Two experiments have been approved to use this beamline: the Direct Photon Experiment, E706, and the Hadron Jet Experiment, E672. The initial beam requirements of the E706 experiment were, $\sim 10^7$ π^-/sec in a -530 GeV secondary beam and a beam spot of $\sim$ 1cm^2 plus the capability of tagging π^+ in the positive 530 GeV beam[37].

Design of the MW beamline began at the end of 1982. The beamline was designed to transport secondaries with energies between 1000 Gev and 25 Gev. First beam on target was recorded on 17 June 1987.

Preliminary tunes of magnet current settings, were done to maximize yields, reduce losses and optimize beam profiles at the E706 experimental target. Tunes for several energies required by E706 were determined at the beginning of the run period (Jun. 1987).

There were two primary running modes, positive and negative, which were different from each other for safety reasons. In addition during the 1987-88 run there was a dedicated calibration run. All the beam running modes will be described in detail in the following chapters.

2.1.1 Beam configuration

The spatial coordinates (x, y, and z) used to describe the MW-beamline are specified as follows: The z axis points along the direction of motion of the primary proton beam (that is, it points downstream). Looking downstream, positive x points in the horizontal direction to the left and positive y points up in the vertical direction.

The exact location of beamline components and the origin of the z coordinate system is determined by the survey personnel. The position of the MW beamline components and their associated device names are listed on the MW beamsheet in Table 1. The locations given in Table 1are those of the geometric centers of each component. The horizontal displacement of the MW-beamline components is plotted as x versus z in Fig. 4. Commonly used symbols for beamline devices are shown in Fig. 5, along with an explanation of the beam device names.

The MW-beam is a secondary beam since it is used to transport particles of a fixed energy that are produced by colliding the proton beam, directly from the accelerator, onto a production target. The polarity and the momentum selection of the particles transported by the MW-beamline is initially done by the first

MW SECONDARY

Z CENT.	X CENT.	POSITION ELEMENT CODE	POWER SUPPLY
1424.0	32.70	BEGINNING OF BEAM	
1430.2	32.93	EARTLY BEND MAGNET	MW6W-1
1444.2	33.30	EARTLY BEND MAGNET	MW6W-2
1450.2	33.09	EARTLY BEND MAGNET	MW6W-3
1477.1	34.25	DUMP COLLIMATOR - 239"	
1494.0	34.70	S1 SPOILER - 150 X 62 X 60	MW7S-1
1506.0	35.09	3Q120	MW7Q1-1
1517.0	35.45	3Q120	MW7Q1-2
1530.0	35.84	SPOILER - 144 X 90 X 130	MW7S-2
		WC1 - 2 MM VACUUM SWIC	MW7WC1
		BEAM STOP	MW7BS
1555.3	36.66	VERTICAL COLLIMATOR - 96"	MW7CV1
1564.3	36.88	HORIZONTAL COLLIMATOR - 96"	MW7CH1
1575.3	37.20	3Q120	MW7Q2-1
1591.8	37.70	B2 BEND MAGNET 4 X 2 X 240	MW7W1
1600.3	38.24	3Q120	MW7Q2-2
1619.0	38.61	3Q120	MW7Q3-1
1631.3	38.99	3Q120	MW7Q3-2
1676.3	40.47	3Q120	MW7Q4-1
1687.0	40.85	3Q120	MW7Q4-2
1699.2	41.22	3Q120	MW7Q5
1707.2	41.49	VERTICAL VERNIER , X 4 X 30	MW7V-1
1711.2	41.62	VERTICAL VERNIER , X 4 X 30	MW7V-2
1716.2	41.78	HORIZONTAL VERNIER 4 X 4 X 30	MW7H
1779.5	43.83	SWIC - 2MM, VACUUM	MW7WC2
1783.7	44.00	VERTICAL COLLIMATOR - 96"	MW7CV2
1792.7	44.30	HORIZONTAL COLLIMATOR - 96"	MW7CH2
1803.2	44.64	3Q120	MW7Q6-1
1814.7	45.02	3Q120	MW7Q6-2
1831.7	45.58	S3 - SPOILER - 36 X 36 X 240	MW7S-3
1859.2	46.49	B2 BEND MAGNET 4 X 2 X 240	MW7W2-1
1886.0	47.25	B2 BEND MAGNET 4 X 2 X 240	MW7W2-2
1901.7	48.03	S4 - SPOILER - 36 X 36 X 240	MW7S-4
1934.1	49.25	3Q120	MW8Q1-1
1946.6	49.69	3Q120	MW8Q1-2
1957.1	50.12	3Q120	MW8Q2
1975.1	50.90	S5 - SPOILER - 36 X 36 X 204	MW7S-5
1990.1	51.36	3Q120	MW8Q3-1

Table 1: MW Beamsheet

2001.0	51.79	3Q120	MW8Q3-2
2013.1	52.23	3Q120	MW8Q4
2020.5	52.06	B2 BEND MAGNET 4 X 2 X 240	MW7W2-3
2042.3	53.36	VERTICAL VERNIER , 4 X 4 X 30	MW8V1-1
2046.3	53.52	VERTICAL VERNIER , 4 X 4 X 30	MW8V1-2
2050.0	53.67	2 MM VACUUM SWIC - AIR	MW8WC1
2132.4	56.97	DIFF. CERENKOV COUNTER - 158 FT.	
2219.0	60.44	2 MM VACUUM SWIC - AIR	MW8WC2
2224.9	60.68	VERTICAL COLLIMATOR - 96"	MW8CV
2234.4	61.06	HORIZONTAL COLLIMATOR - 96"	MW8CH
2244.2	61.45	3Q120	MW8Q5-1
2255.7	61.91	3Q120	MW8Q5-2
2272.6	62.59	VERT. CALIB. MAG. - 3 X 6 X 120	MW8D
2300.6	63.71	3Q120	MW8Q6-1
2312.1	64.17	3Q120	MW8Q6-2
2323.6	64.63	3Q120	MW8Q7
2363.6	66.24	3Q120	MW8Q8-1
2375.1	66.70	3Q120	MW8Q8-2
2386.6	67.16	3Q120	MW8Q9
2394.6	67.48	VERTICAL VERNIER, 4 X 4 X 30	MW8V2-1
2398.6	67.64	VERTICAL VERNIER, 4 X 4 X 30	MW8V2-2
2403.6	67.84	HORIZONTAL VERNIER, 4 X 4 X 30	MW8H
2450.0	69.70	1 MM SWIC	~~MW8WC~~
2453.0	69.82	END OF BEAM LINE -- EXPERIMENTAL TARGET	

Table 1: (Continued)

string of dipole magnets (MW6W). By adjusting the currents in these magnets, the secondaries with the desired polarity and momentum are bent west through the hole of a dump collimator and then transported through the beamline.

2.1.2 Naming Convention for Beamline Devices

All the beamline components are monitored and controlled remotely through the experimental areas central PDP-11 computer, using the Experimental Areas Beamline Control System (EPICS)[28]. CAMAC electronics were used for the physical connection between the central computer and the beamline devices. Fermilab uses its own non-standard serial communications CAMAC electronics.

Beam line components are given device names in the EPICS computer's memory which are used when they are controlled remotely. Each device name has the format A B C DDDN-M which specifies at least four types of information[29] :

(1) A - Area in which the device is located.

(2) B - Beamline in which the device is located.

(3) C - Enclosure (building) in which the device is located.

(4)- DDDN-M - Type, function, and label, N-M, of the device. Device types and functions are designated by the following codes:

Q = Quadrupole magnet

W = Dipole bending magnet that bends to the west

E = Dipole bending magnet that bends to the east

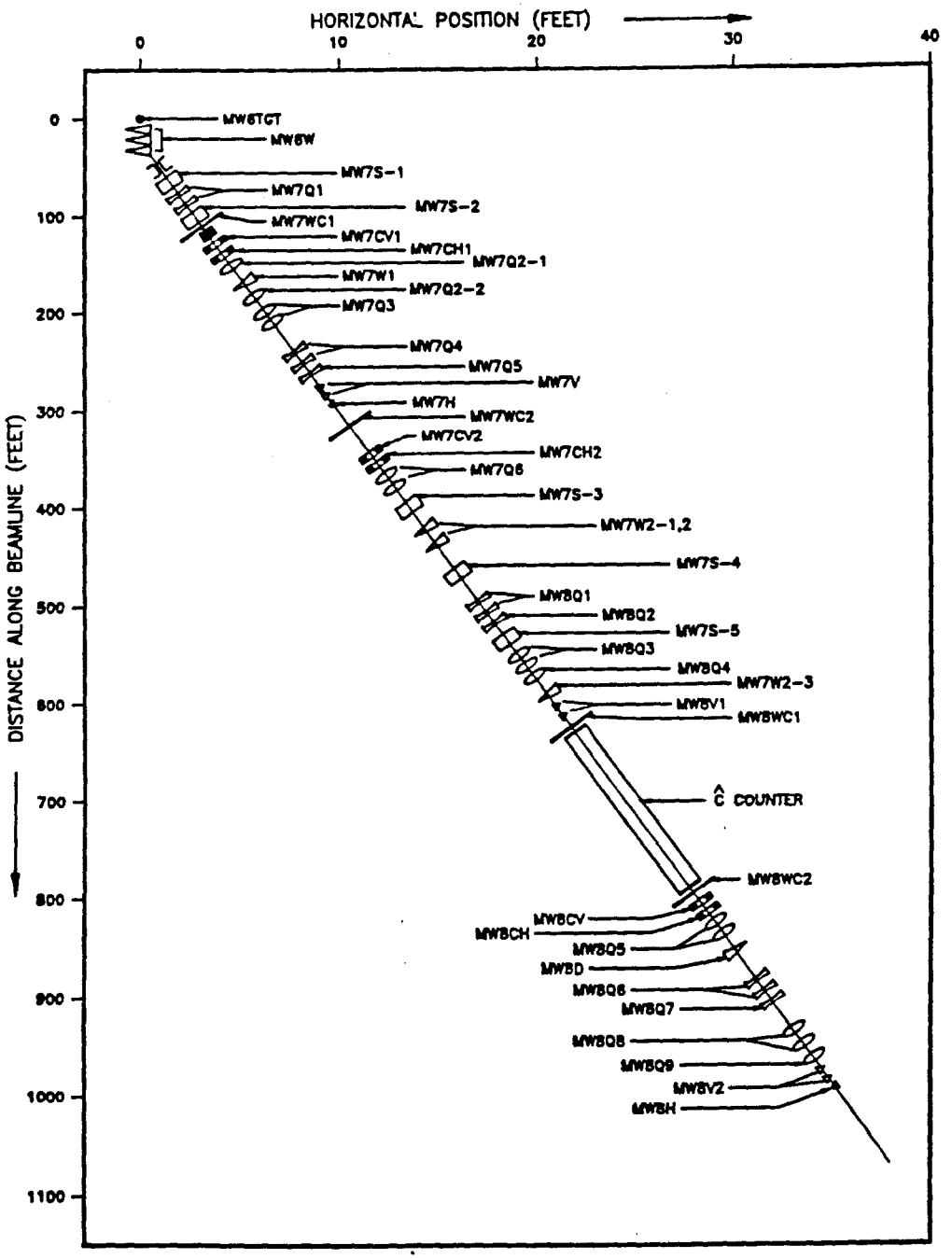

Figure 4: MW Beamline Components plotted in horizontal position versus longitudinal position.

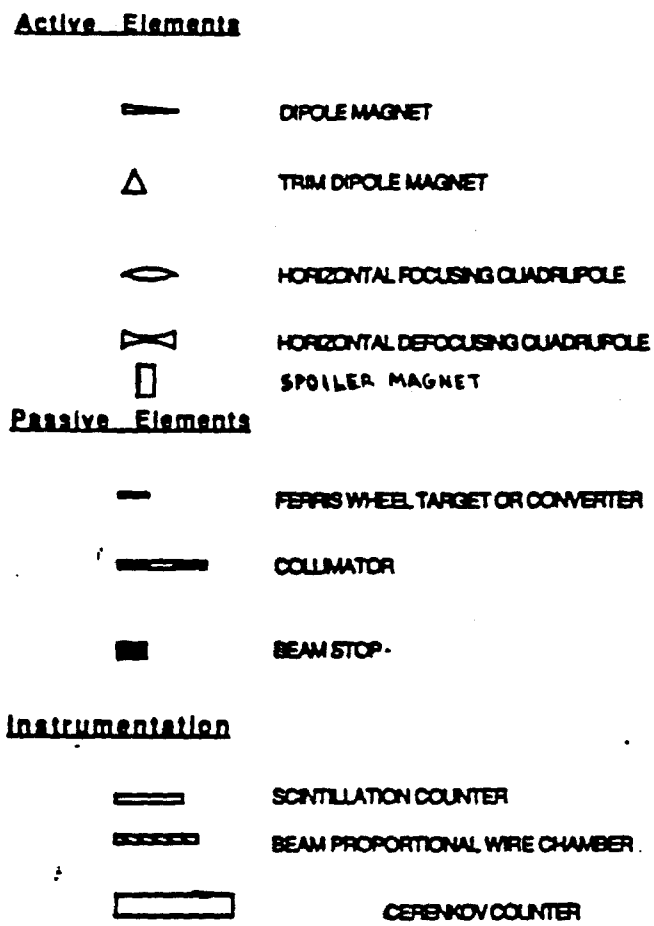

Figure 5: Beamline component symbols.

U = Dipole bending magnet that bends the beam up

D = Dipole bending magnet that bends the beam down

V = Trim magnet that bends in the vertical plane

H = Trim magnet that bends in the horizontal plane

S = Spoiler magnet

CH = Collimator with horizontal collimating jaws

CV = Collimator with vertical collimating jaws

TGT = Target

PWC = Proportional wire chamber

SEM = Secondary emission monitor

SC = Scintillation counter

CC = Cherenkov counter

SRD = Synchrotron radiation detector

BS = Beam stop

BD = Beam dump

A typical device name would be MW7W1-1, where:

M = Meson area

W = West beamline

7 = Enclosure 7

W = Dipole magnet that bends to the west

1-1 = First magnet in the magnet string MW7W1.

In most of the beamlines magnets are employed in strings, or series of magnets. All magnets in a string have the same current setting, and are connected to the same power supply.

For radiation safety purposes, the beamlines are in underground tunnels and are divided into sections identified by the enclosure which allows access to that region of the beamline. The MW-beamline is divided into two sections, enclosures MW7 and MW8 (Fig. 6 (top)). The experimental hall is in the enclosure MW9.

2.1.3. Critical Devices

Critical devices are beamline components which can shutdown the beam in case of an emergency. In the case of the MW beamline the MW6W magnet string, MW7Q1, and MW7BS are the critical devices[30],[31]. These devices are the only components in the MW secondary beamline that cannot be controlled by the beam users (i.e the E706 experimenters) only by the Experimental Areas Operations personnel. If safety gates or doors are opened, or radiation safety safety limits exceeded, the critical devices are used to shut off the beam. Failure of any of the MW critical devices would trip both the magnet string MW1W and the MW2BS beamstop (used as backups) assuring that no primary beam is reaching the MW primary target.

For any controlled accesses in the MW9 enclosure, the Experimental Areas Operations personnel had to shut off MW6W and MW7Q1 and close the MW7BS beamstop. Any controlled access in the MW7 or MW8 enclosures required the

additional closing of the MW2BS.

2.1.4. The Spill Cycle

Beam is sent to the experimental areas on a cyclic basis, called the "spill cycle". Protons are accelerated in a series of bunches in the Tevatron until they reach 800 GeV. They are then extracted from the Tevatron ring into the Switchyard, where the primary proton beam is split and distributed to the experimental areas.

The spill cycle is 57.2 sec long, and is divided into six precise segments called T-times (see Fig. 6 (bottom)). The actual "spill" of beam to the experimental areas begins at the start of T5 and is complete by the beginning of T6, a time span of 23 sec. Beam intensity should remain constant throughout the spill, but this is not always true.

To conserve energy and reduce the chance of overheating, most beamline magnets are operated with the desired current only when the beam spill is present and no current at other times. This is called "ramping" because of the characteristic nature of an oscilloscope display of the current in these magnets.

2.1.5 Radiation Safety

There are two categories of radiation safety considerations, both of interest to the experimenters[32],[33]. One concern is the muon halo which must be kept below

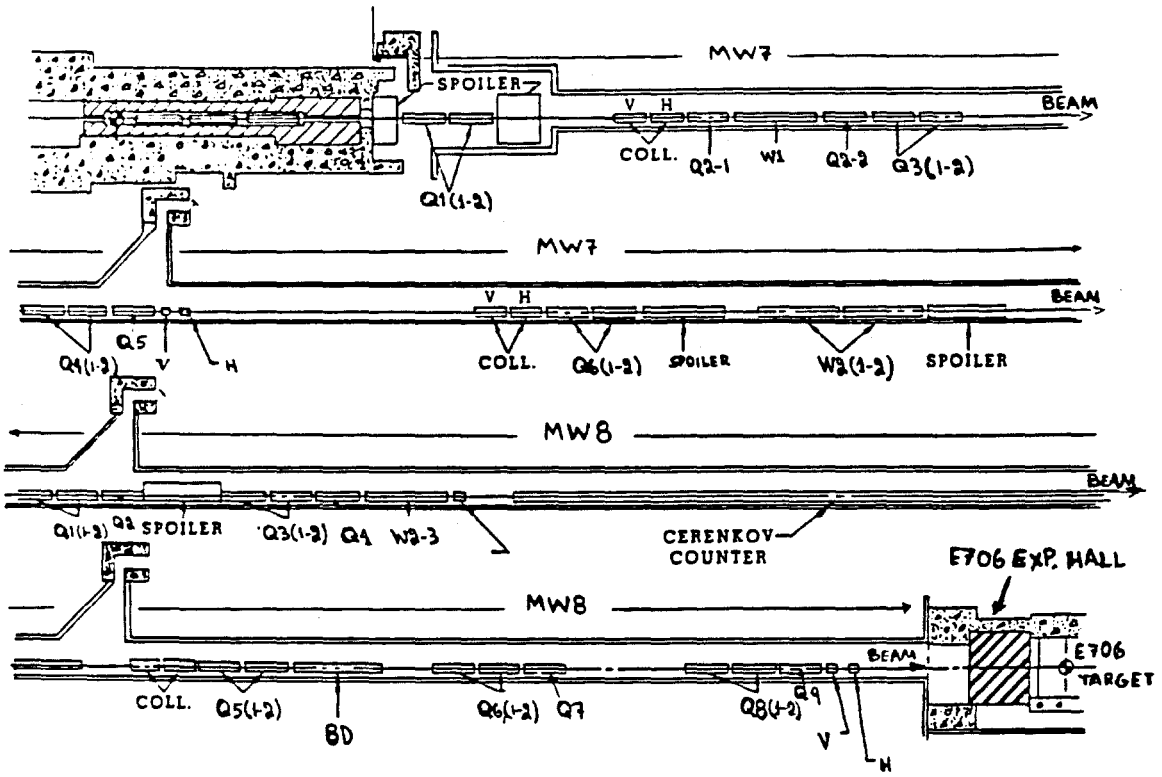

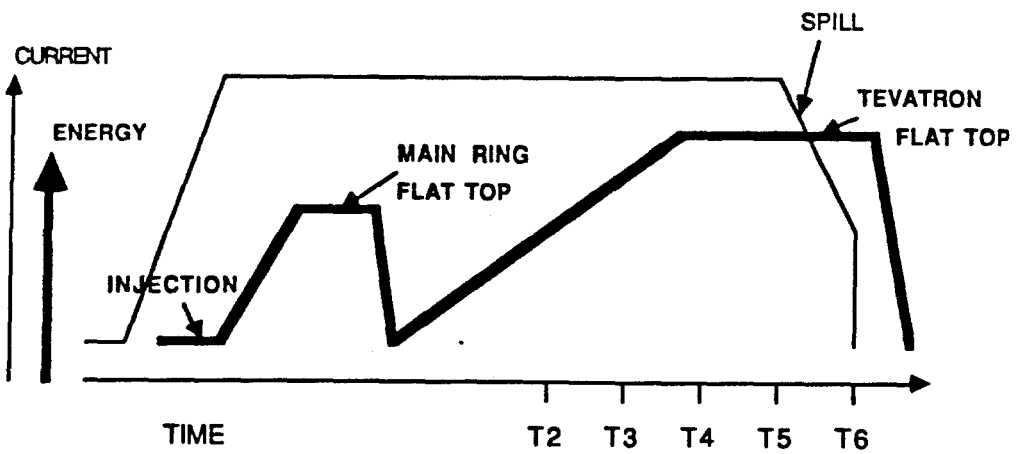

Figure 6: (top): MW Beamline components in the different enclosures. (bottom): The spill cycle.

some nominal average level to meet the integrated long term human dose limits. The other is the single pulse accident scenario by which levels cannot exceed a one pulse limit. In this scenario it is assumed that the full Tevatron intensity somehow strikes the MW primary target giving rise to an intense secondary beam that interacts along the beamline. In this scenario it is assumed that the intensity from the accelerator is at its maximum of 3×10^{13} particles per spill. This could give a secondary intensity of up to 3×10^{10}, thus some way to dump the primary beam upstream must be used.

The background muons in the MW Spectrometer hall come from π^- and π^+ which are produced at the primary target and decay. Other sources are K decays and μs produced directly in the primary target. The muon levels are reduced with spoilers which deflect the muons in the vertical plane; negatives up and positives down. Averaging over some reasonable area in the MW Hall shows a muon background of 0.1 mrad or less, which satisfies safety requirements. However, this muon flux limits the integrated intensity of primary protons to the MW target to 5.7×10^{17} protons per calendar year[34].

During the negative mode of operation the dump magnets MW6W bend the 530 GeV negatives 6 mrads west along the dump collimator aperture (Fig. 7 (top)). The 800 GeV primary protons bend east, away from the dump collimator aperture by 5.3 inches[35]. Increasing the dump magnet current increases the separation, so there is no need for an overcurrent trip on the MW6W power supply.

If the MW primary beamline for the positive running were the same way as for the negative running mode, the separation between the primary 800 GeV proton beam and the dump aperture would be only 0.27 inches for a secondary beam of

530 GeV. This would be dangerous from a radiation safety point of view. This is because the dump magnets must steer the positive secondary beam towards the dump aperture and as the secondary energy approaches the primary energy so does the primary beam approach the aperture (Fig. 7(top)). Any small excursion of the pre-target quad or trim magnet current, or any over-current on the dump magnets could aim the primary proton beam into the MW secondary beamline. The solution to this potential radiation hazard is simply to aim the beam away from the dump aperture and accept a non - zero degree production angle for the secondary beam[36] (Fig. 7(bottom)).

2.2. E-706 Spectrometer

The E706 spectrometer (Fig. 8 (top)) consists of a set of silicon strip detector (SSD) planes, upstream and downstream of the experimental target, an analyzing magnet (p_T^{kick}=450 MeV), a set of multiwire proportional chambers (PWC), a liquid argon calorimeter (LAC) with both electromagnetic and hadronic sections, and a forward calorimeter. Downstream of the forward calorimeter is a muon measurement system provided by E672 consisting of a toroid, PWC's, scintillation counters, and absorbers. An iron hadron shield is positioned in front of the spectrometer to attenuate hadronic halo. The hadron shield is 4.7 m long and has a 10 cm wide vertical slot along the beamline. The two iron slabs that fill the slot are removable by overhead crane allowing the beam to be scanned in the vertical direction during calibration. Two arrays of scintillation counters (VW) shadow

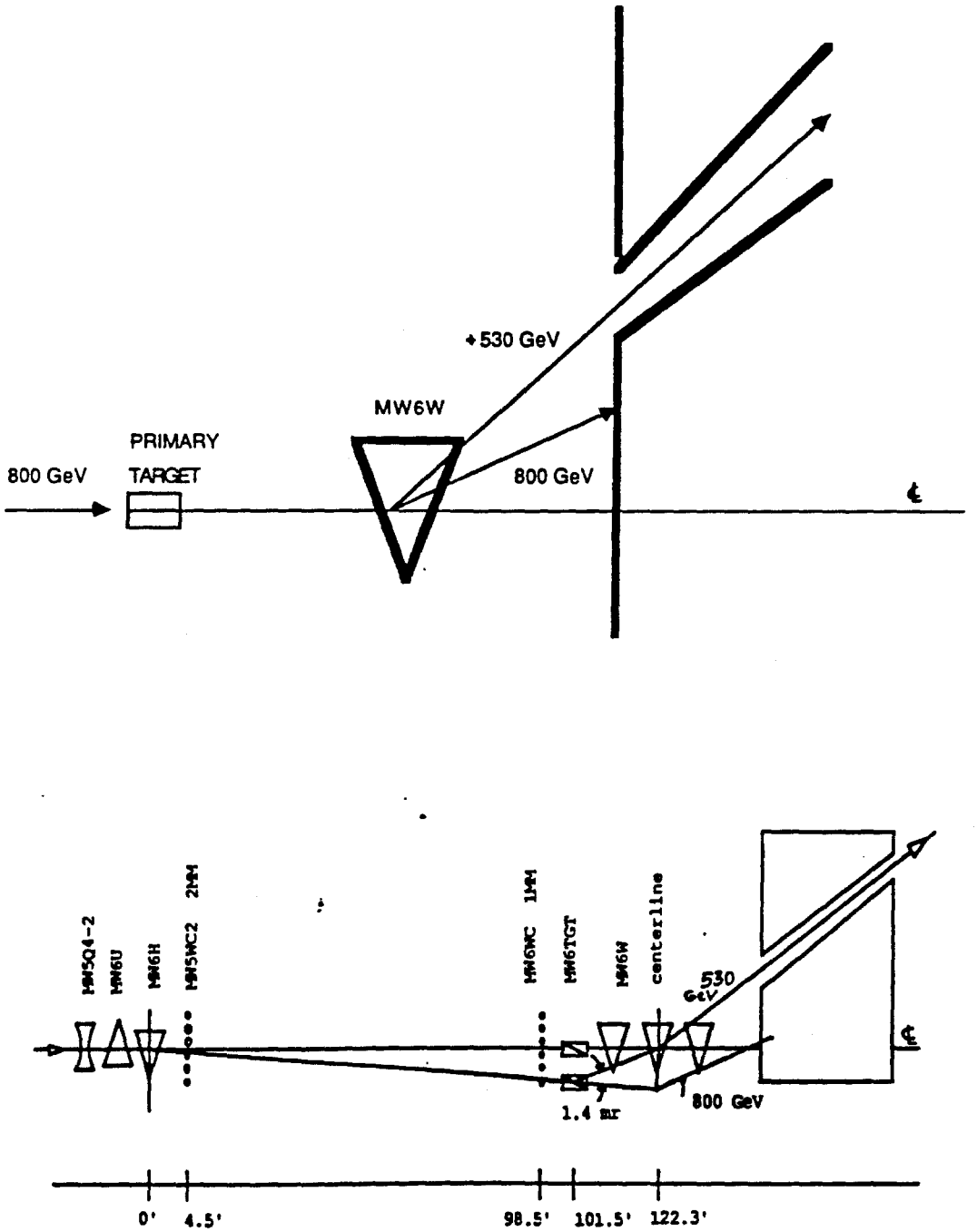

Figure 7: (top): Zero production angle for the MW Primary target. (bottom): Non zero production angle for the MW Primary target.

the spectrometer and are used to reduce the contamination of triggers by halo muons.

The SSD's[38],[39] consist of 7 X-Y modules (14 planes), with a total of 7,120 active strips. All SSD's have a 50 μm pitch and a thickness of 300 μm. Three of the X-Y modules, consisting of 9 cm^2 wafers, are located before the target, and are used to define the trajectory of the beam particle. The other four modules, one made of 9 cm^2 wafers and the other three made of 25 cm^2 wafers, are positioned after the target and measure the trajectories of the produced particles in front of the analyzing magnet (Fig. 8 (bottom)).

E706 has an active target consisting of a target material and silicon wafers. During most of the data run, the actual target consisted of twenty 2 mm-thick beryllium plates separated by 1.6 mm gaps. The center of the experimental target is 1029.0 ft (313.64 m) downstream of the primary target.

The PWC's[42] consist of 4 sets of XYUV modules (16 planes in total) with a total of 13,400 instrumented channels and a 2.54 mm pitch. The dimensions are: 1 (1.22 m$\times$1.63 m); 2 (2.03 m$\times$2.03 m); and 1 (2.44 m$\times$2.44 m). The PWC's are used to determine the momenta and the directions of the charged particles in conjunction with the SSDs. They had a rate capability greater than 1 Mhz and an angular segmentation smaller than 1 mr as seen from the target.

The electromagnetic calorimeter[40],[41] (EMLAC) is used to measure the positions and energies of all particles showering electromagnetically (γ, e^-, e^+). It has a transverse size of 3.1 m and is divided into quadrants. Each quadrant contains 66 layers of 2 mm-thick lead plates interleaved with 1.6 mm thick G10 radial (r) or azimuthal (ϕ) anode readout boards (r and ϕ each have 33 readout boards).

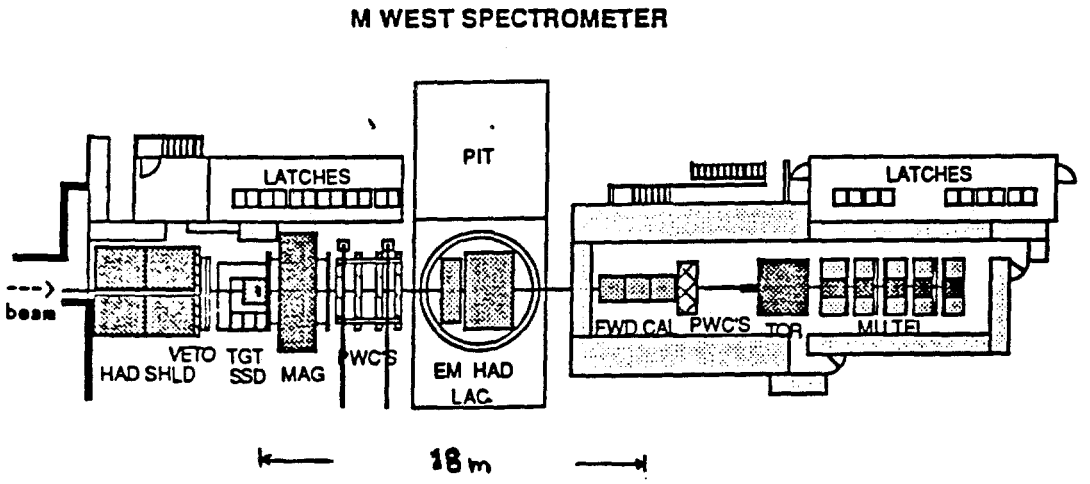

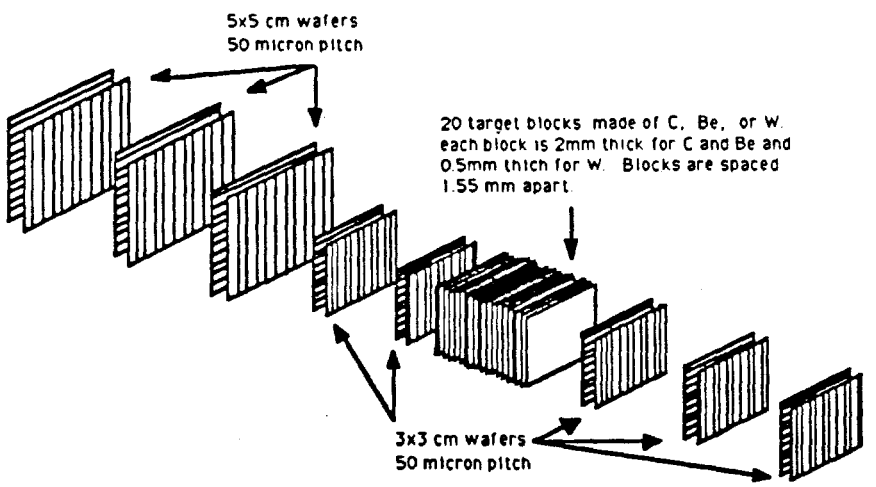

Figure 8: (top): Layout of the MW spectrometer. (bottom): Layout of the Silicon Strip Detector.

The anode boards are further subdivided into octants (Fig. 9 (top)). The argon gaps are 2.5 mm thick. An r-coordinate readout board consists of 254 concentric radial strips each 5.5 mm wide. The strips of sequential layers focus on the target. The ϕ-coordinate strips are divided into inner and outer regions. Each inner ϕ strip subtends an azimuthal angle of 16.4 mrad while each outer ϕ strip covers an angle of 8.2 mrad. The readout of the electromagnetic calorimeter is divided longitudinally into two sections: the front section consists of 22 layers (10 radiation lengths) and the back section has 44 layers (20 radiation lengths). The front face of the ELAC is 1057.7 ft downstream of the primary target.

The hadron calorimeter is used to measure the positions and energies of hadrons. It consists of 52 one inch thick stainless steel plates, interleaved with 53 readout units called "cookies". The hadron calorimeter has a tower readout structure with each tower consisting of a series of triangular readout pads (Fig. 9 (bottom)). The triangles grow in size in proportion to the distance from the target from a height of 4.4 inches in the front to a height of 5.5 inches in the back. The hadron calorimeter is also segmented longitudinally into a front section (two interaction lengths) and a back section (six interaction lengths).

The two LAC sections are mechanically independent of each other and reside within a common cryostat (Fig. 10 (top)). The two calorimeters are attached with steel rods to a gantry structure which can move transverse to the beamline, a feature essential for the assembly and the calibration of the calorimeters. A helium filled beam pipe, about 40 cm in diameter, passes through the center of the LAC. A thin-walled steel vessel, filled with low density foam (Rohacell), is fastened in the cryostat in front of the detector to reduce the number of interactions lengths

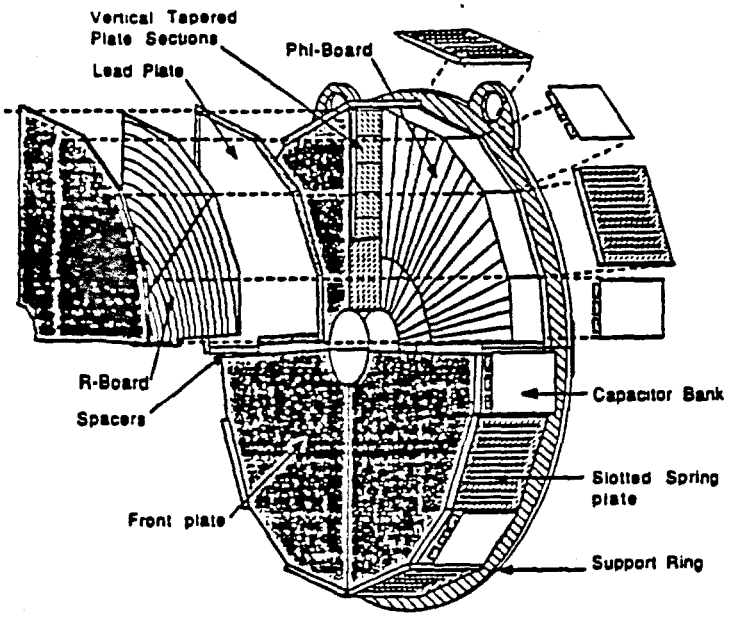

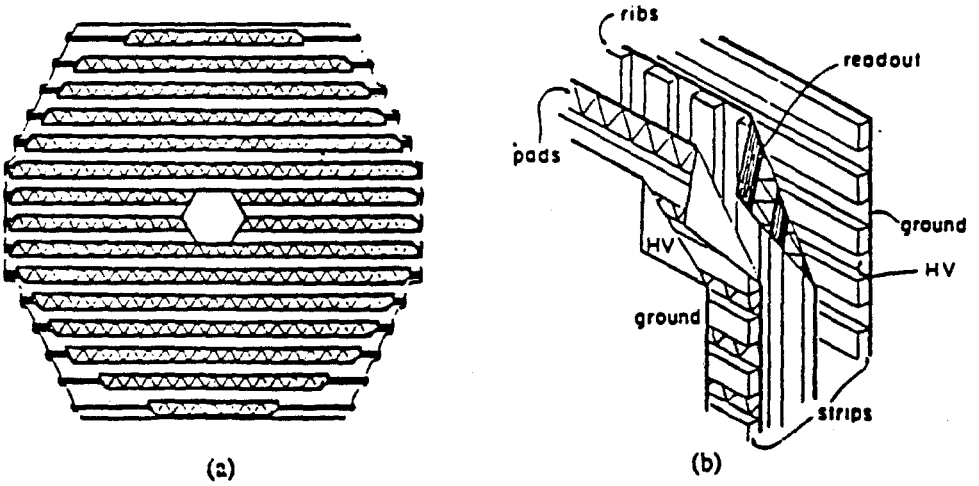

Figure 9: (top): A view of the electromagnetic calorimeter. (bottom): a) A view of one of the readout planes in the Hadron calorimeter. b) The structure of a cookie.

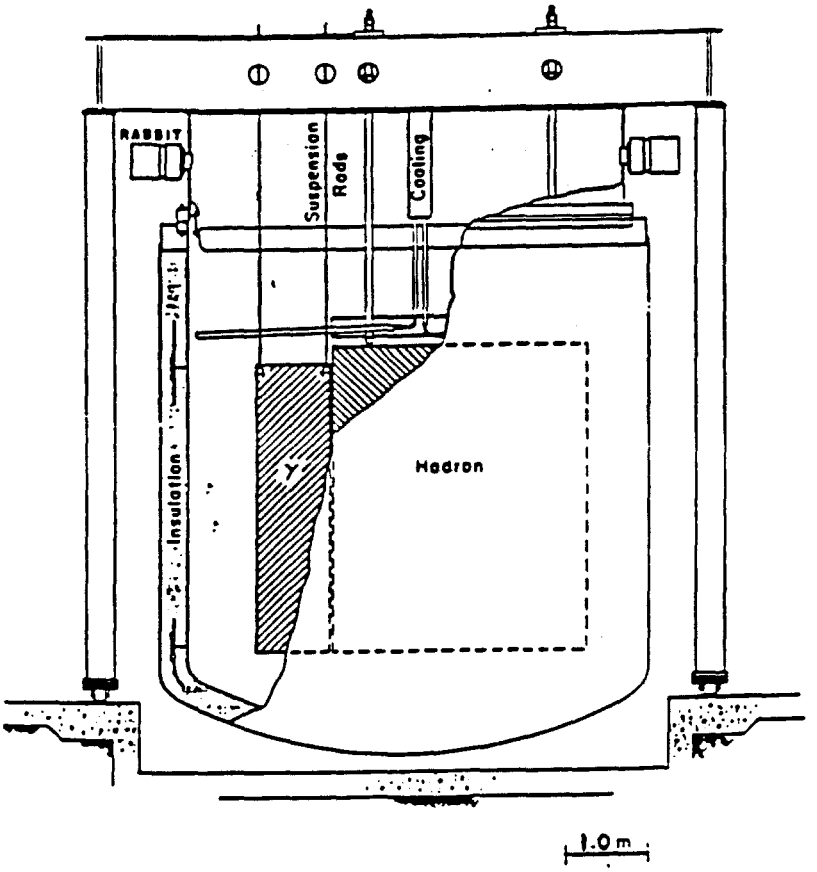

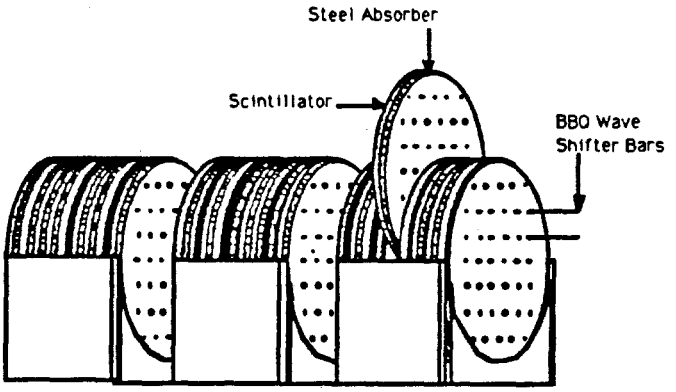

Figure 10: (top): The overall gantry and cryostat of the LAC. The beam is incident from the left. (bottom): View of the Forward Calorimeter.

in front of the calorimeters.

The forward calorimeter[43] is a steel and scintillator calorimeter divided longitudinally into three sections, for a total of 10 hadronic interaction lengths. Each section has a diameter of 114 cm and contains 28 steel plates spaced 6.3 mm apart interleaved with 29 scintillator sheets. Each steel plate is 1.9 cm thick and each scintillator plate is 4.6 mm thick. The light was collected through wave shifter rods that were inserted longitudinally into the calorimeter (Fig. 10 (bottom)).

2.3. Modes of operation

During the 1986 - 87 "shakedown" run of E-706 the beamline was used to transport secondaries with momentum of 530 GeV to the experimental target. All of the direct photon data were taken at this momentum. The momentum of 530 GeV was picked so that pions would have the same incident momentum per valence quark as for 800 GeV protons.

In order to study the response of the electromagnetic and hadron calorimeters it was also necessary to produce and transport hadrons and electrons of various momenta. For this purpose there were several calibration run modes.

2.3.1. Negative (pion) mode

This was one of the two standard modes of operation of the MW-beamline during the last run. It is often called the negative pion mode since -530 π^- are the predominant particles produced and transported (97.0%). There are also a few K^- (2.9%) which are tagged using the Cherenkov counter and a negligible amount of $\bar{p}$ (0.2%).

In this mode a primary target of 0.77 interaction lengths of Al was used initially. This target was replaced near the end of the run with an 1.0 interaction length Al target with the same lateral dimensions in order to improve the secondary particle yield. In this mode the production angle was 0 degrees and the initial momentum selection was done by the MW6W string of dipoles.

A characteristic of this mode was the limited secondary intensity. The maximum secondary flux obtained was 2×10^7 secondaries per spill for 1×10^{12} incident 800 GeV protons on the 1.0 interaction length Al target. A study has been made[44] of reconfinguring the MW-beamline in order to increase the acceptance and achieve a flux of 3.6×10^7 secondaries per spill for 1×10^{12} incident 800 GeV protons. Replacing some of the present 3Q120 (3 inch diameter) quadrupoles with 4Q120 (4 inch diameter) quadrupoles will further increase the secondary flux to a total of 5×10^7 secondaries per spill per 1×10^{12} incident protons.

2.3.2 Positive (proton) mode

In this mode 530 GeV a finite production angle of 1.4 mrad was used. Positive secondary fluxes were very large. Some collimators were closed to limit the

secondary intensity and prevent radiation trips along the beamline. The typical secondary intensity was 6.5×10^7 particles/spill, with the MW7CH2 collimator opened to 0.50 in. compared to 4.0 in. for the negative running.

The positive beam contains 7.2% π^+, 1.5% K^+, and 91.3% p. During the positive running mode the Cherenkov counter was used to tag π^+, and there was no dedicated K^+ run. Using the beamline to transport the 800 GeV primary proton beam during the next run will require the use of two pinhole collimators[45] upstream of the primary target in order to attenuate the primary beam intensity by a factor of 5×10^{-4}.

2.3.3. Calibration mode

In the calibration mode, negative beam energies of -25, -50, -100, -200 and -400 GeV, were used to study the response of the liquid argon calorimeter. There were two calibration runs; the first in December of 1987 and the second in February 1988. It was determined by Monte Carlo studies that up to the energy of 100 GeV there would be enough electrons in the beam to calibrate the electromagnetic calorimeter. The electrons were distinguished from the hadrons by using the differential Cherenkov counter, and/or by reconstructing the energy deposited in the electromagnetic calorimeter and checking that the shower was consistent with that of an electron.

In the first calibration run, the beam configuration remained intact, the SSD's target system was rolled out of the beam and the calorimeter was moved. The

beam was steered up and down the face of the calorimeter by the calibration dipole MW8D. In this case the maximum beam deflection angle 0.77 mrad was determined by the diameter of the vacuum pipe at the end of the hadron shield (1.5 inch inner diameter). The beam was limited to $Y = \pm 4.83$ cm at the EMLAC front face. However the dead region between two quadrants in EMLAC extended from $Y = \pm 2.9$ cm, to $Y = \pm 4.0$ cm. Thus, the window for testing the LAC consisted of two regions with widths varying from 0.83 cm to 1.83 cm. Only the 200 GeV and 400 GeV momenta were used in this run. The Cherenkov counter was not used since it was not possible to distinguish electrons from pions with the Cherenkov at these momenta.

The second calibration run was the main calibration run in which the position dependence of the calorimeter response was studied. In this calibration run all the beamline magnets downstream of the MW8D calibration magnet (they were hung from the ceiling instead of being anchored to the floor), were moved out of the beam. The hadron shield center insert, the veto wall, the SSD's, the analysis magnet and some of the chambers were also moved so as not to limit the acceptance.

The LAC was moved horizontally to several X positions and for each position the beam was steered up and down so as to hit the LAC at several positions. Fig. 11 shows all the calibration runs giving the positions where the calibration beam hit the front face of the LAC. The underlined numbers indicate runs with the 100 GeV beam. Run 3131 is the only 25 GeV calibration run, and the rest of the numbers are for 50 GeV beams. The Cherenkov was used to tag electrons or pions during the 50 GeV calibration runs.

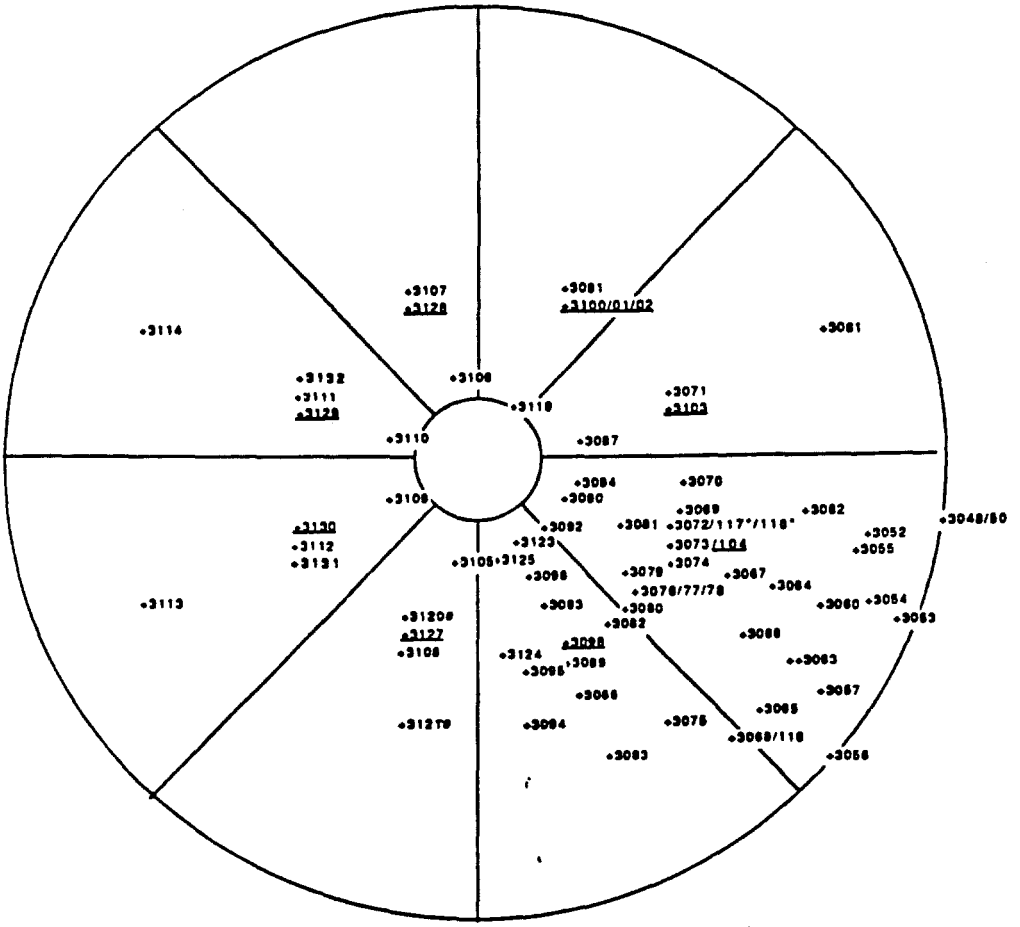

Figure 11: Run numbers during the second calibration run, superimposed in the front face of the LAC.

In both calibration runs the beam intensity was adjusted using the collimators (mainly the MW7CH2) to about 10^4 particles per second to avoid pileup of signals in the detectors. The momentum spread of the the calibration beam was typically $\pm 2.0\%$ (HWHM).

As mentioned before, the initial momentum selection of all the calibration momenta was done by the MW6W string of dipole magnets. At the end of the run a more precise determination of the momenta was done by using the current values and the excitation curves of all the bending dipoles in the MW-beamline as it will be explained in the next chapter. According to that determination the nominal values 50, 100, 200, 400 and 530 GeV should be understood as 56.4 ± 0.6, 102.8 ± 0.8, 189 ± 1, 379 ± 3 and 508 ± 5 GeV respectively.

3. MW-BEAMLINE STUDIES AND PARTICLE YIELDS

. In this chapter I describe the design characteristics of the MW-beamline and the way the beamline performed during the first E-706 run. Computations of particle yields for the beamline, using Monte Carlo programs, are compared with the actual yields.

3.1. BEAM OPTICS

A beam of charged particles can be transported in a way analogous to the focusing of light by an optical lens and the dispersion of light into colors by a prism. Particle beams can be deflected, focused to a small spot, and have their particles selected by momentum. All these functions can be accomplished by beamline magnets which have their fields oriented perpendicular to the beam direction.

A collection of charged particles is considered to be a beam when the particles are all moving essentially in the same average direction with nearly the same momentum and have a small spatial separation transverse to the general direction of motion. The spatial extent of the beam must be small enough to pass through the apertures of the magnets and other beamline devices. A charged particle in a magnetic field **B** experiences a force **F** given by the expression

$$\dot{\mathbf{p}} = \mathbf{F} = q(\mathbf{v} \times \mathbf{B}) \tag{3.1}$$

Here q is the charge of the particle, **v** its velocity, and **p** its momentum. Since

the velocity is the time derivative of position we could use Eq. 3.1 to formulate a differential equation of motion with time as the independent variable and find the particle's position as a function of time. However, in charged particle optics we are not so much interested in finding a particle's position as a function of time as in determining the path it follows. Thus the independent variable is then taken to be the distance along the beamline axis.

A beam of particles at any time can be represented by a collection of points in a six-dimensional phase space. The phase space location of a single particle has three coordinates specifying the position of the particle and three giving its momentum. From the region of phase space occupied by the particles a single point is chosen to be the reference particle. Its path through the magnetic system is known as the reference trajectory and its momentum is the reference momentum.

The position and momenta of all the other particles may be defined in terms of the reference particle. All spatial points on the reference trajectory define a longitudinal axis, s, in the direction of the reference momentum. The two traverse coordinates, x and y, are perpendicular to the s axis, with $x = y = 0$ on the s axis (Fig. 12).

The momentum of a beam particle is specified by three quantities. The two directional tangents and the fractional deviation from the reference momentum p_0. The direction tangents x' and y' are equal to the ratios of transverse to longitudinal components of momentum so that

$$x' = \frac{p_x}{p_s} \quad y' = \frac{p_y}{p_s} \tag{3.2}$$

Since p_x and p_y are small compared to p_s, x' and y' are approximately equal to

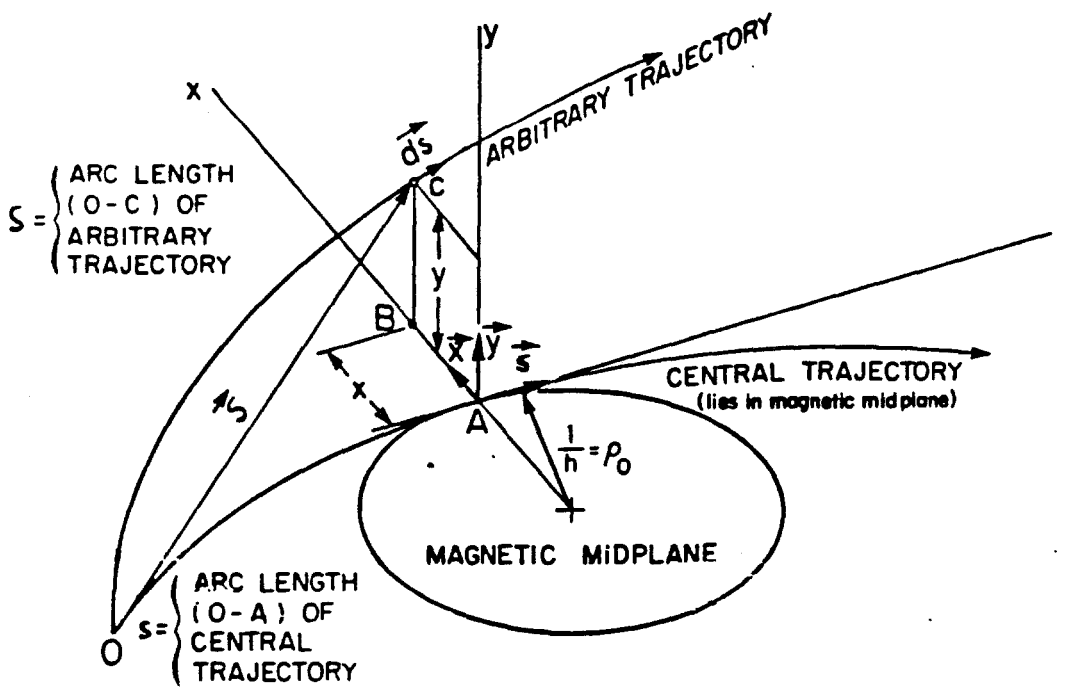

Figure 12: Curvilinear coordinate system used in derivation of the equation of motion[46].

the horizontal and vertical angles with respect to the reference momentum. The fractional momentum deviation is given by

$$p = p_0(1 + \delta) \tag{3.3}$$

The three spatial coordinates are the transverse distances x and y from the reference trajectory, and l, the difference in path length between a given trajectory and the reference trajectory. Using these coordinates system we can describe the action of a charged particle beamline on a collection of beam particles.

The beamlines contain magnets to bend the trajectories of the particles and focus the beam. In most of the beamlines the magnets are oriented so that the pole profiles are symmetric about a horizontal plane, known as the median plane. There is no horizontal component of the magnetic field in this plane and the system is said to posses midplane symmetry. The reference trajectory is bent entirely in the horizontal plane and to first order there is no dependence of the vertical coordinates on δ.

Using a moving coordinate system whose origin is always on the central trajectory and considering a system with midplane symmetry, we can derive the equations of motion with the distance s along the reference trajectory as the independent variable [46]. The resulting equations are

$$\begin{aligned} x'' + (1-n)h^2 x &= h\delta \\ y'' + nh^2 y &= 0 \end{aligned} \tag{3.4}$$

where n is a dimensionless parameter defined in terms of the vertical magnetic field component as

$$n = -\left[\frac{1}{hB_y}\left(\frac{\partial B_y}{\partial x}\right)\right]_{x=0,\ y=0} \tag{3.5}$$

The two Equations (3.4) are linear second-order differential equations. We can write the general solution of these two differential equations as

$$\begin{aligned} x(s) &= x_0 b_x(s) + x_0' c_x(s) + \delta d_x(s) \\ y(s) &= y_0 b_y(s) + y_0' c_y(s) \end{aligned} \tag{3.6}$$

where $b_{x,y}(s)$ and $c_{x,y}(s)$ are linearly independent solutions of the homogeneous equations for x and y, while the dispersion function, $d_x(s)$, is a particular solution to the inhomogeneous equation in x. The coefficients x_0 and y_0 are the initial transverse coordinates, and x_0' and y_0' their initial derivatives with respect to the longitudinal coordinate s. To first order, x_0' and y_0' are the initial angles the trajectory makes with the reference trajectory.

The general form for the homogeneous equation for both the horizontal and vertical planes has the form

$$\frac{d^2q}{ds^2} + k^2 q = 0 \tag{3.7}$$

Beam lines are comprised of magnets separated by drift spaces. Within any magnet, the value of k^2 is constant, and Eq. (3.7) can be easily solved.

If k^2 is positive, the trajectory executes harmonic motion and the two independent solutions are

$$\begin{aligned} q(s) = b(s) &= \cos ks \\ q(s) = c(s) &= \frac{1}{k}\sin ks \end{aligned} \tag{3.8}$$

If k^2 is negative, the trajectory is divergent and the general solution can be ex-

pressed as

$$\begin{aligned} q(s) = b(s) &= \cosh ks \\ q(s) = c(s) &= \frac{1}{k}\sinh ks \end{aligned} \tag{3.9}$$

The values for k are derived from Eq. (3.5) and satisfy the relation

$$k_x^2 + k_y^2 = h^2 \tag{3.10}$$

The solution of the inhomogeneous Eq. (3.6) for $d_x(s)$ can be expressed in terms of the characteristic functions $b(s)$ and $c(s)$. In a region where k_x and h are independent of s we can write[46],

$$d_x = \frac{h}{k_x^2}(1 - c_x(s)) \tag{3.11}$$

where this expression is independent of the sign of k_x^2.

3.2. First-Order Matrix Formalism

One can express the solutions for x,x',y, and y' in terms of matrix equations

$$\begin{aligned} \begin{pmatrix} x(s) \\ x'(s) \\ \delta \end{pmatrix} &= \begin{pmatrix} b_x(s) & c_x(s) & d_x(s) \\ b'_x(s) & c'_x(s) & d'_x(s) \\ 0 & 0 & 1 \end{pmatrix} \begin{pmatrix} x_0 \\ x'_0 \\ \delta \end{pmatrix} \\ \begin{pmatrix} y(s) \\ y'(s) \end{pmatrix} &= \begin{pmatrix} b_y(s) & c_y(s) \\ b'_y(s) & c'_y(s) \end{pmatrix} \begin{pmatrix} y_0 \\ y'_0 \end{pmatrix} \end{aligned} \tag{3.12}$$

Each magnetic element in a beamline has its own characteristic matrix (transfer matrix) describing the transformation of trajectory coordinates as a particle passes

through that element. The effect of N successive elements, each with a transfer matrix $\mathbf{R}_i$, is given by the total transfer matrix of the system $\mathbf{R}_S$ which is the product of the individual transfer matrices[48].

$$\mathbf{R} = \mathbf{R}_n \ldots \mathbf{R}_2 \mathbf{R}_1 \tag{3.13}$$

Using the transfer matrix notation we need not solve equations (3.5) for the general case. Instead we find solutions for sections of a beamline where the magnetic field and its transverse derivatives are independent of s. The general solution can be represented as the product of the transfer matrices representing the solutions for the individual sections.

The full six-by-six transfer matrix for a static magnetic system with horizontal midplane symmetry is[46]

$$\begin{pmatrix} x(s) \\ x'(s) \\ y(s) \\ y'(s) \\ l(s) \\ \delta(s) \end{pmatrix} = \begin{pmatrix} R_{11} & R_{12} & 0 & 0 & 0 & R_{16} \\ R_{12} & R_{22} & 0 & 0 & 0 & R_{26} \\ 0 & 0 & R_{33} & R_{34} & 0 & 0 \\ 0 & 0 & R_{43} & R_{44} & 0 & 0 \\ R_{51} & R_{52} & 0 & 0 & 1 & R_{56} \\ 0 & 0 & 0 & 0 & 0 & 1 \end{pmatrix} \begin{pmatrix} x_0 \\ x'_0 \\ y_0 \\ y'_0 \\ l_0 \\ \delta_0 \end{pmatrix} \tag{3.14}$$

where the coordinate l is the difference in path length between the arbitrary and the reference trajectory. The zero elements $R_{13}, R_{14}, R_{23}, R_{24}$ R_{31}, R_{32}, R_{41}, R_{42}, R_{36}, and R_{46} in the R matrix are a direct consequence of midplane symmetry. If midplane symmetry is destroyed, these elements will in general become non-zero. The zero elements in column five occur because x,x',y,y', and δ are independent of the path length difference l. The zero elements in the sixth row are a result of static magnetic fields, which make the scalar momentum a constant of the motion.

Thus, with central plane symmetry and with all bending taking place in the horizontal plane, we can write

$$x(s) = x_0 R_{11}(s) + x_0' R_{12}(s) + \delta_0 R_{16}(s) \tag{3.15}$$

and

$$y(s) = y_0 R_{33}(s) + y_0' R_{34}(s) \tag{3.16}$$

The matrix elements have special physical meaning. When plotted versus the longitudinal position along the beamline the transport characteristics of the beam become apparent. In particular, R_{11} and R_{33} are relating spatial magnification in the horizontal and vertical planes respectively; R_{12} and R_{34} are related to the angular magnification, or angular properties, of the beamline in the horizontal and vertical planes, respectively, and R_{16} is related to the fractional momentum spread.

So far we have examined the transmission characteristics of individual particle trajectories. However, a beamline transmits many trajectories with a variety of initial coordinates, so it is useful to have a method to treat many trajectories at one time. An extension of the matrix algebra discussed before allows one to represent the beam to first order as an ellipsoid in the six-dimensional space[48]. The extend of this ellipsoid is termed "the beam envelope", and the ellipsoid contains the region of space containing the particle trajectories. This ellipsoid is called the "beam ellipse".

The equation of the ellipse is

$$\mathbf{X}^t \sigma^{-1} \mathbf{X} = 1 \tag{3.17}$$

where $\mathbf{X}'$ is the transpose of the coordinate vector $\mathbf{X}$ and σ is a real, positive definite, symmetric matrix. Given an initial ellipsoidal representation $\sigma(0)$ of the beam, the ellipse's transformation through the beamline is given by

$$\sigma(s) = \mathbf{R}\sigma(0)\mathbf{R}^t \tag{3.18}$$

so that the beam ellipse matrix remains an ellipse under first-order transformations. As a result of Liouville's theorem the volume of the region enclosed by the ellipse remains unchanged under a transformation by the transfer matrix. All of the important physical parameters of the beam ellipsoid can be expressed as functions of the matrix elements of the sigma matrix at the location in question. In particular, the square roots of the diagonal elements ($\sqrt{\sigma_{ii}}$) are the projection of the ellipse upon the coordinate axes and thus represent the maximum extent of the beam in the various coordinate directions. The correlation between components (orientation of the ellipse) is determined by the off-diagonal terms (the σ_{ij}'s).

In order to illustrate these concepts we consider a two-dimensional ellipse. The ellipse matrix in a two-dimensional phase space x,x' would have the form

$$\sigma = \begin{pmatrix} \sigma_{11} & \sigma_{12} \\ \sigma_{12} & \sigma_{22} \end{pmatrix} \tag{3.19}$$

and the inverse

$$\sigma^{-1} = \frac{1}{\epsilon^2}\begin{pmatrix} \sigma_{22} & -\sigma_{12} \\ -\sigma_{12} & \sigma_{11} \end{pmatrix} \tag{3.20}$$

where ϵ^2 is the determinant of σ.

The expansion of the matrix equation $\mathbf{X}^t\sigma^{-1}\mathbf{X} = 1$ is the equation of the ellipse

$$\sigma_{22}x^2 - 2\sigma_{12}xx' + \sigma_{11}x'^2 = \epsilon^2 = |\sigma| \tag{3.21}$$

The (x, x') plane beam ellipse represented by Eq. 3.19 is shown in Fig. 13 (top) along with the physical meaning of the sigma matrix elements.

The area of the ellipse is given in terms of the determinant of the ellipse matrix

$$A = \pi(|\sigma|)^{1/2} = \pi x_{max}x'_{int} = \pi x_{int}x'_{max} \tag{3.22}$$

The correlation between x and x' depends on the off-diagonal term σ_{12} and is defined as

$$r_{12} = \frac{\sigma_{12}}{\sqrt{\sigma_{11}\sigma_{12}}} \tag{3.23}$$

The correlation r_{12}, measures the tilt of the ellipse and the intersection of the ellipse with the coordinate axes.

Figure 13 (bottom) shows an example of the transformation of the ellipse σ_0 by a two-dimensional $\mathbf{R}$ matrix representing a drift space of distance L:

$$\mathbf{R_{drift}} = \begin{pmatrix} 1 & L \\ 0 & 1 \end{pmatrix} \tag{3.24}$$

In working with beam ellipses, we can determine the region of the initial phase space which can be transmitted by a given beamline. This region is called the initial phase space "acceptance" of the beamline and can be specified in the variables $x, x'y, y'$,and δ. The phase space volume transmitted by a beamline is limited by the effective apertures of the components of the beamline, including the magnets and collimators.

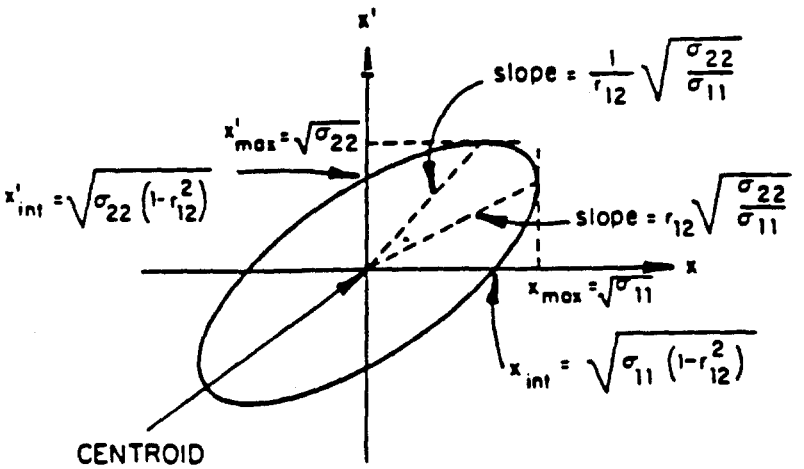

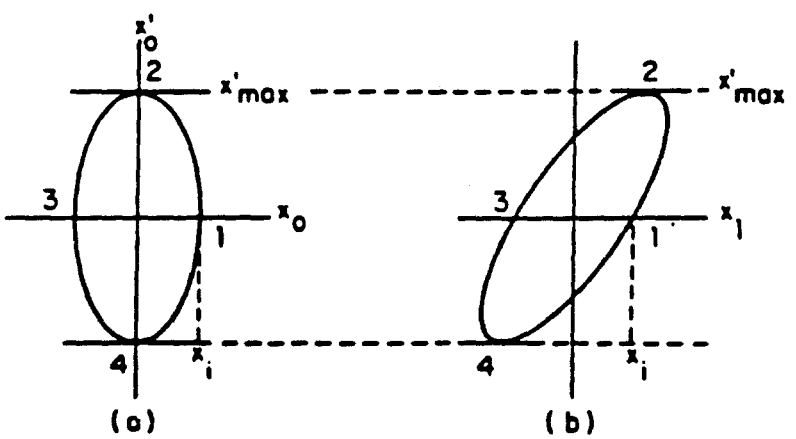

Figure 13: (top): Dimensions of a two-dimensional phase space ellipse in terms of ellipse matrix elements[48]. [(bottom): The two-dimensional ellipse (a) after traversing a drift space, becomes ellipse (b).]

3.3. Magnetic Elements

3.3.1 Dipole Magnets

Dipole magnets are so called because they have two poles of opposite polarity. The pole faces are flat and parallel and the magnetic field is uniform in the central region of the magnet. A cross section of a dipole magnet perpendicular to the reference trajectory is found in Fig. 14(top).

The dipole magnets serve two main functions in a beamline. The first is to change the direction of the beam by bending the particle's trajectories. The second is to provide dispersion, or a correlation of traverse position with momentum, since different momenta are deflected by different angles by a dipole magnet. This allows a restricted range of momenta to be transmitted by the beamline and permits precise momentum definition.

The physical quantities needed to describe a bending magnet are the effective magnetic length L, the reference trajectory magnetic field B_0, and the normalized field index n. If the field index n is between 0 and 1, the effect of the magnet is focusing in both planes. If the field index is less than zero, the magnet is horizontally focusing and vertically defocusing. If the field index is greater than one, the magnet is horizontally defocusing and vertically focusing. Thus, a secondary function of a bending magnet is it provides focusing in one or both transverse coordinates.

In most of the beamlines, it is desirable to focus and bend with separate magnets

so that different focal conditions can be achieved without relocation of beamline elements. At high energies, bend angles become very small and magnet lengths become long. In these beamlines the bending magnets are both zero-gradient and rectangular, instead of bent in an arc to follow the beam trajectory. Rectangular zero-gradient bending magnets are simple to manufacture and can have high fields on the central orbit.

The transfer matrix for a zero gradient rectangular bending magnet in the x bending plane is written as

$$R = \begin{pmatrix} 1 & \rho \sin\theta & \rho(1-\cos\theta) \\ 0 & 1 & 0 \\ 0 & 0 & 1 \end{pmatrix} \tag{3.25}$$

The focusing action of the dipoles in these beamlines is small compared to that of the quadrupoles. For high energy beamlines, the arc length traveled by the beam is nearly the effective length of the bending dipole (Fig. 14(bottom)), and the bending angle θ for a momentum p_0 is given by

$$\theta[mrad] = \frac{B[T]L[m]}{0.0033356p[GeV]} \tag{3.26}$$

In the MW-beamline all the strings of bending magnets are used to bend the beam west. The x and s position of each dipole in the MW beamline along with the nominal bending angle is shown in Fig. 15. The dipole MW7W1 is also used to introduce dispersion in the horizontal plane. As a result we have a momentum dispersed first focus and a momentum selection of the transmitted momenta can be done by using the horizontal collimator MW7CH2. In addition to the west bending dipoles there is a dipole magnet MW8D used to bend the beam vertically for calibration purposes.

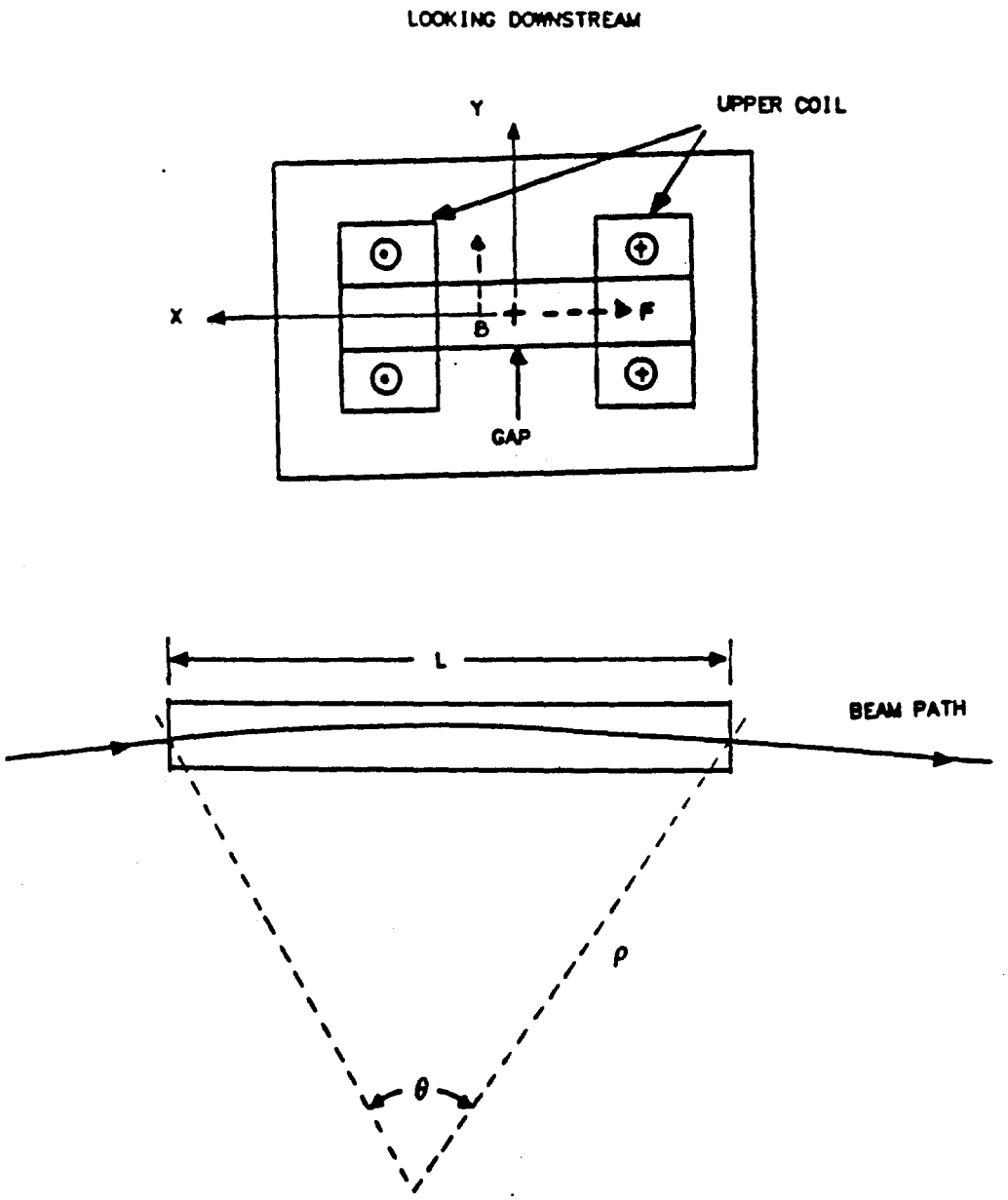

Figure 14: (top): Dipole magnet cross section showing B and Force components and the central trajectory coordinates. (bottom): Charged particle path in the bending plane of a dipole magnet.

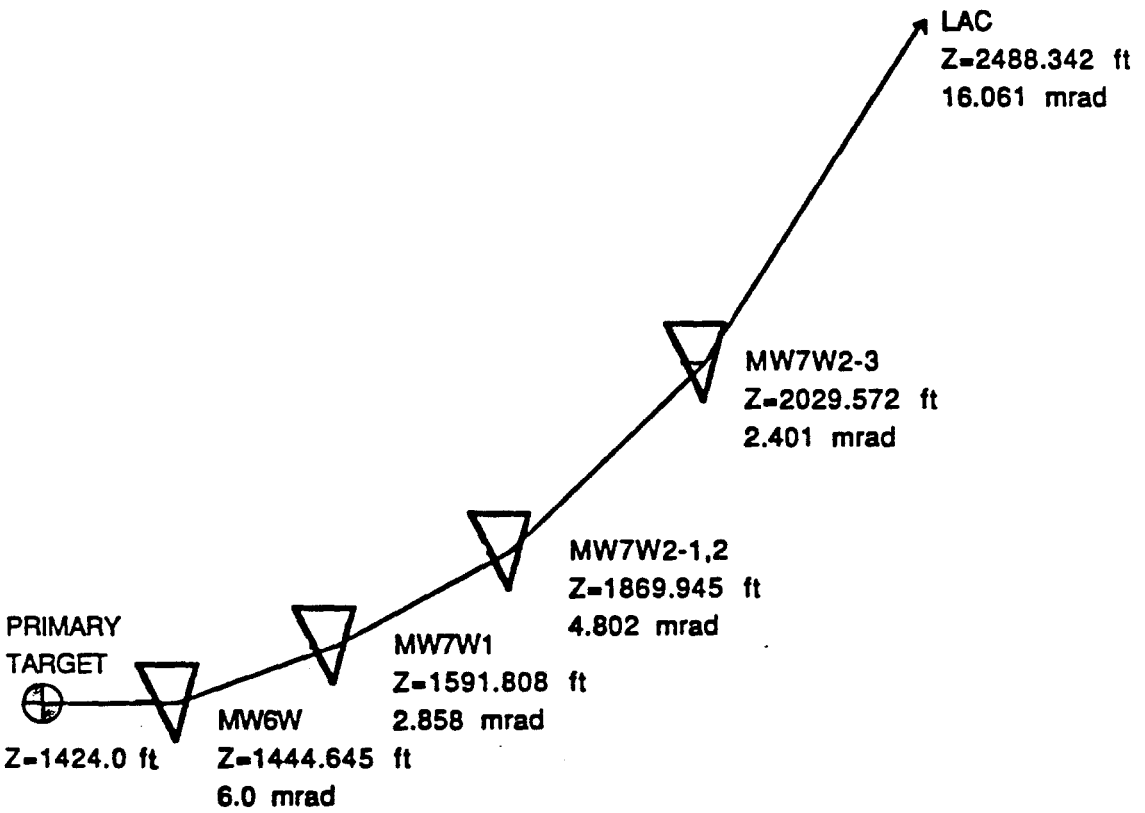

Figure 15: MW secondary beam bend points.

3.3.2 Quadrupole Magnets

A quadrupole is so named because it has four magnetic poles with a cross-sectional configuration shown in Fig. 16. The two physical parameters used to describe the magnetic field in a quadrupole are B_0, the magnitude of the field at the pole-tip radius, and a, the pole-tip radius.

The magnetic field components can be expressed as

$$\begin{aligned} B_x &= \frac{B_0 y}{a} = gy \\ B_y &= \frac{B_0 x}{a} = gx \end{aligned} \tag{3.27}$$

where the quantity g is the constant of proportionality between the magnitude of the field and the radius.

Since there is no net field along the axis of the quadrupole magnet the curvature h of the reference trajectory is zero, and the field index n is zero. We define

$$k_q^2 = \frac{q}{p_0}\frac{\partial B_y}{\partial x} = \frac{qg}{p_0} \tag{3.28}$$

Since there is no dispersive term, the transfer matrix for a quadrupole is two by two in both planes. If the pole-tip field strength is positive, then the magnetic field tends to restore the trajectory toward the optic axis in the horizontal plane and to deflect it away from the optical axis in the vertical plane. The quadrupole is then horizontally focusing and vertically defocusing. The equations of motion in the two planes become

$$\begin{aligned} x'' + k_q^2 x &= 0 \\ y'' - k_q^2 y &= 0 \end{aligned} \tag{3.29}$$

If the pole-tip field is negative, the focusing and defocusing characteristics of the

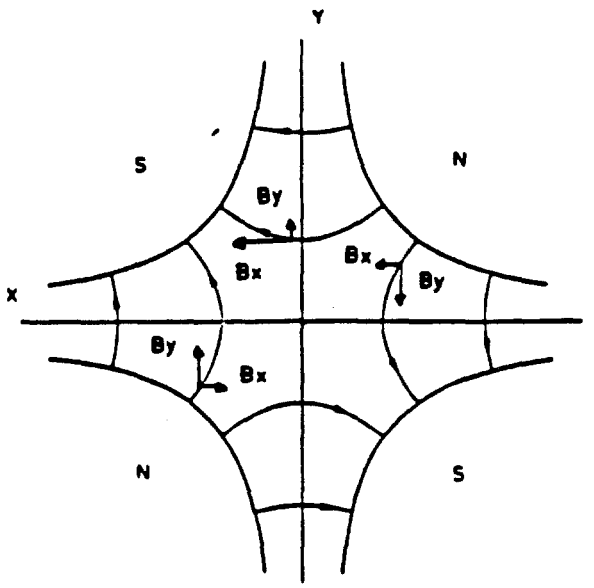

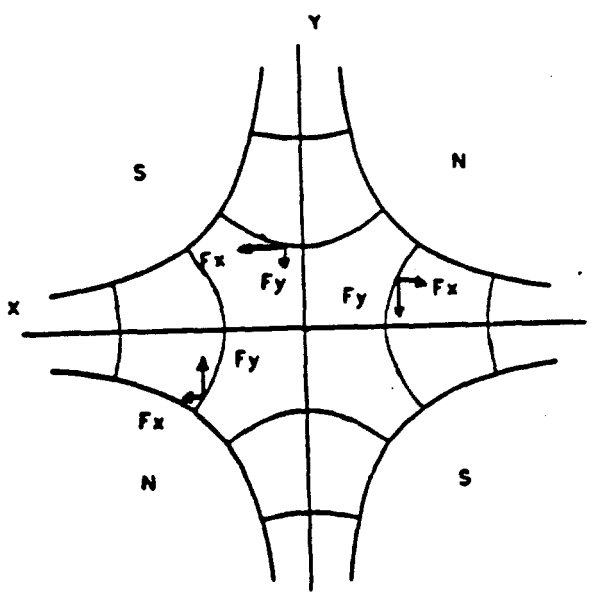

Figure 16: (top): Cross sectional configuration of a quadrupole magnet showing the B components (top), and the Force components (bottom).

two planes are reversed and the signs in Eqs. (3.29) are interchanged.

The transfer matrix for a quadrupole in terms of k_q and the effective magnetic length L in the focusing plane is

$$R_f = \begin{pmatrix} \cos k_q L & \frac{1}{k_q} \sin k_q L \\ -k_q \sin k_q L & \cos k_q L \end{pmatrix} \tag{3.30}$$

In the defocusing plane the transfer matrix is:

$$R_d = \begin{pmatrix} \cosh k_q L & \frac{1}{k_q L} \\ k_q \sinh k_q L & \cosh k_q L \end{pmatrix} \tag{3.31}$$

If $L \rightarrow 0$, but $k_q^2 L$ is finite, then the transfer matrix for a quadrupole in the focusing plane is

$$R_f = \begin{pmatrix} 1 & 0 \\ \frac{-1}{f} & 1 \end{pmatrix}, \tag{3.32}$$

where $\frac{1}{f} = k_q^2 L$ is the focal length of the quadrupole in the focusing plane. Thus a single quadrupole can be approximated by a thin lense with a focal length f that is focusing in one plane and defocusing in the other. This is the reason that a quadrupole magnet is represented by a convex (convergent) lens or by a concave (divergent) lens symbol, depending on which of the quadrupole planes is being shown.

Quadrupoles are usually employed in combinations in beamlines to form lens systems which focus in both planes. The two most common systems are quadrupole doublets and triplets.

There are four types of imaging which lens systems may be used to achieve: point to point (position independent of the initial angle), point to parallel (angle independent of the initial angle), parallel to point (position independent of the initial position), and parallel to parallel (angle independent of position).

For monoenergetic point-to-point imaging in the x-plane, the magnification of a lens system is given by

$$M_x = \frac{x(s)}{x_0} = R_{11} = b_x(s) \tag{3.33}$$

and in the y plane by

$$M_y = R_{33} = b_y(s) \tag{3.34}$$

A doublet lens consists of two magnets (or magnet strings) with opposite polarity, often of the same length. A doublet is not necessarily symmetric in its focus in the vertical and horizontal planes, resulting in different magnifications in the two planes and causing a first-order image distortion. Figure 17 (top) illustrates the doublet's property of ansymmetric focusing and Fig. 17 (middle) and 17 (bottom) show how doublets can be used to achieve point-to-point and point-to-parallel focusing, respectively.

The most common triplet lens system is a symmetric triplet, consisting of two quadrupoles of identical polarities and lengths, separated by a quadrupole of opposite polarity and twice the length, all with the same field gradients. That configuration can result in equal foci in both planes with no first order image distortion.

In the MW beamline both quadrupoles doublets and triplets are used to achieve the different necessary functions. The initial point is the image at the primary target MW6TGT. An asymmetric triplet (MW7Q1, MW7Q2,3 and MW7Q4,5) is used to produce the first focus at MW7CH2 (momentum dispersed focus). The quadrupole singlet MW7Q6 acts as a field lens and bends the dispersed momenta

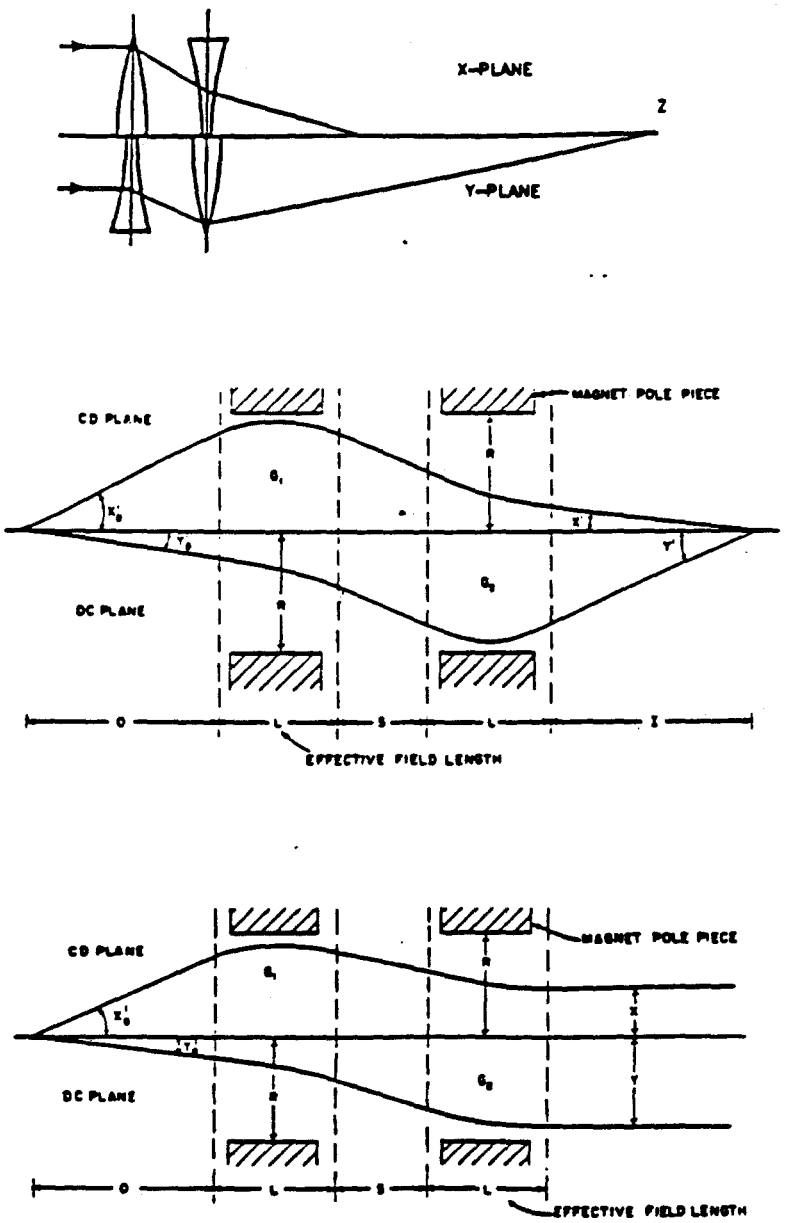

Figure 17: (top): Unsymmetric focusing by a quadrupole doublet. (middle): Point-to-point focusing with a quadrupole doublet. (bottom): Point-to-parallel focusing with a quadrupole doublet (All from Sedman[56]).

into the center of the aperture of the remainder of the beamline. The field lens is followed by a doublet (MW8Q1,2 and MW8Q3,4) which produces a parallel section (point to parallel focusing). Finally an asymmetric triplet (MW8Q5, MW8Q6,7 and MW8Q8,9) is used to focus the beam on the experimental target (parallel to point focusing).

3.4. Computer analysis and Design Considerations

Beamlines are designed and analyzed using charged particle transport computer simulation programs. At Fermilab, the TRANSPORT[48],[50],[51] and TURTLE[52] programs are used.

TRANSPORT is a computer program used to design charged-particle beam transport systems by finding the first-order (or the first and second order if needed) matrix multiplication solution for a set of sequential magnetic elements with static fields. In first order, this is done by fitting the transfer matrix **R** representing the transformation of an arbitrary ray with respect to a reference trajectory and/or fitting the phase space ellipse matrix σ representing a bundle of rays transformed by the system. The program can vary the physical parameters of the elements comprising the system. These parameters include the magnetic fields and their gradients, magnetic lengths and shapes, drift spaces, and the initial beam accepted into the system.

After the beamline configuration is finalized, the TRANSPORT program is used in determining the magnet current settings necessary to transport a given initial

phase space ellipse with a given central momentum (nominal tune). For each tune the program can give the **R** and σ matrix elements at specified locations along the beamline.

TRANSPORT is not a ray tracing program. It only transforms an initial six-dimensional phase space ellipse from the beginning to the end of a beamline. It does not account for the apertures of magnets, collimators, and other beamline devices. This is done by the TURTLE program which is used after the application of TRANSPORT. TURTLE is a ray tracing program with no fitting capability and is applicable to beamlines with small phase space acceptance. Through a Monte Carlo process, it generates (from the production target rays) of particles over the full transportable ranges of momenta and production angles. It then tracks each ray through the beamline and calculates the fraction of rays (and thus the initial phase space acceptance) which are transported through the entire beamline. This is done by solving the equations of motion directly, accounting for apertures and for chromatic and geometric aberrations due to second order effects caused by the beamline's magnetic devices.

TURTLE can calculate, at any point along the beamline, histograms giving the distribution of rays in any of the phase space coordinates. An additional feature is that TURTLE does these calculations for a given particle type (normally protons, pions, and kaons) produced at the target, taking into account the decay of unstable particles.

A special version of TURTLE, called RAYGEL, has been developed to determine electron-positron production and transport based on the ($\pi^\circ \rightarrow \gamma\gamma, \gamma \rightarrow e^+e^-$) cascade process. This program was used to determine $e^\pm$ rates for the

calibration mode of operation.

The MW-beamline was designed to be a two stage high resolution secondary beamline, with mass definition, able to transport a high intensity secondary beam for a wide range of secondary momenta. In the first stage a momentum dispersed focus was produced and a range of momentum was selected by the horizontal collimator MW7CH2. A field lens MW7Q6, located at the first focus 380 ft away from the primary target is used to bend the dispersed momenta into the center of the aperture of the remainder of the beamline. A quadrupole doublet (MW8Q1,2 MW8Q3,4) was used to produce a 200 ft. long parallel section for the differential Cerenkov counter used to tag the beam particles. Finally a triplet was used to focus the beam at the experimental target 1030 ft. away from the primary target.

TRANSPORT was used to calculate transfer matrix elements R_{ij} at designated points along the MW beamline. As was discussed earlier, certain matrix elements have a direct physical meaning in regard to beamline transport characteristics. Figures 18 and 19 plot R_{12}, R_{34}, and R_{16} versus longitudinal distance s along the beamline. The location of magnets is also indicated in these figures. Each symbol represent a group of magnets with the same polarity and field. The σ matrix elements were also calculated. Figure 20 shows $\sqrt{\sigma_{11}} = x_{max}$, and $\sqrt{\sigma_{33}} = y_{max}$ versus s.

The transfer matrix elements R_{ij} are only a function of the beam optics. However, in order to calculate the σ matrix elements the initial phase space that can be transported by the MW beamline must be determined. This was done by using the TURTLE program which takes into account the apertures of the beamline elements.

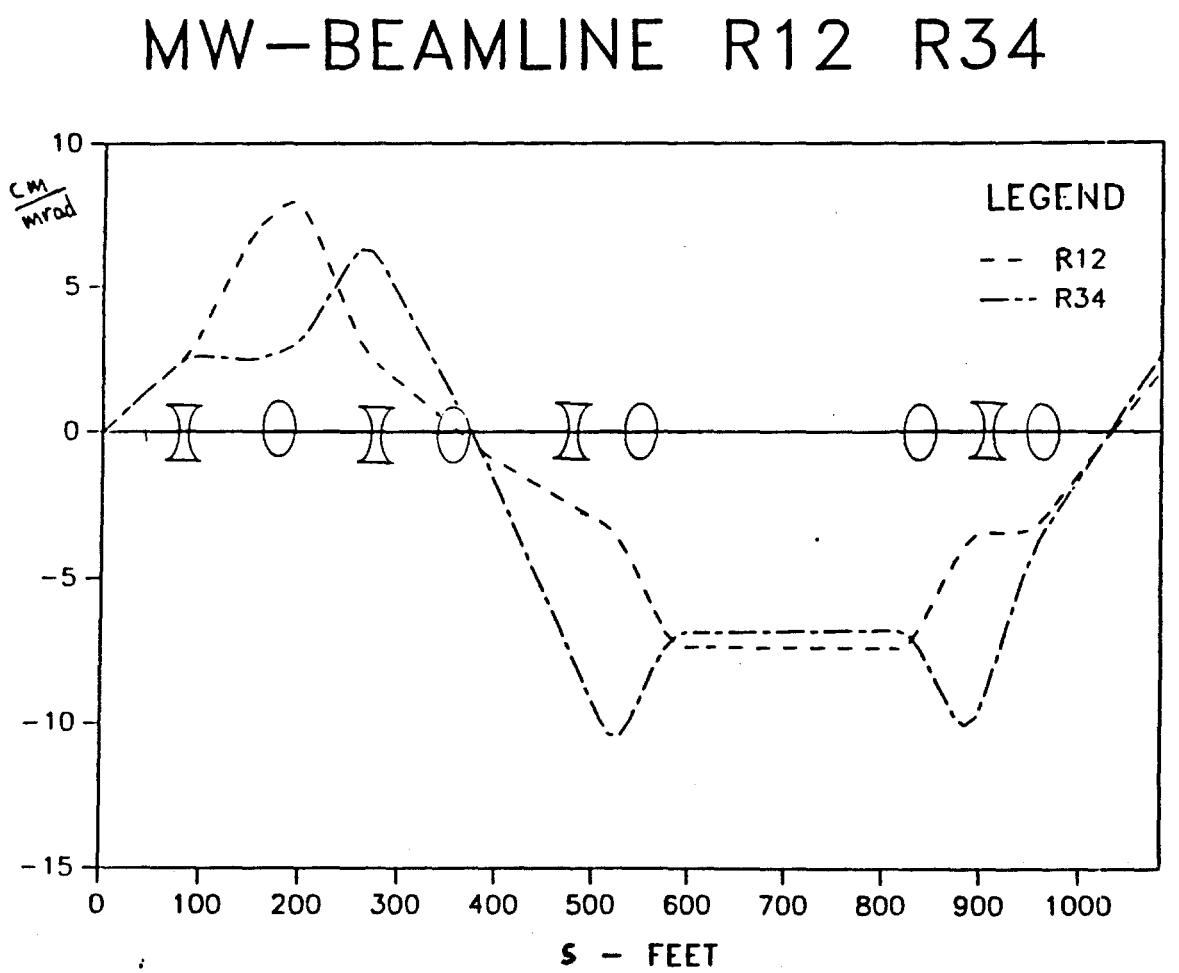

Figure 18: R_{12}, R_{34} matrix for the MW-beamline plotted versus the longitudinal distance s along the beamline.

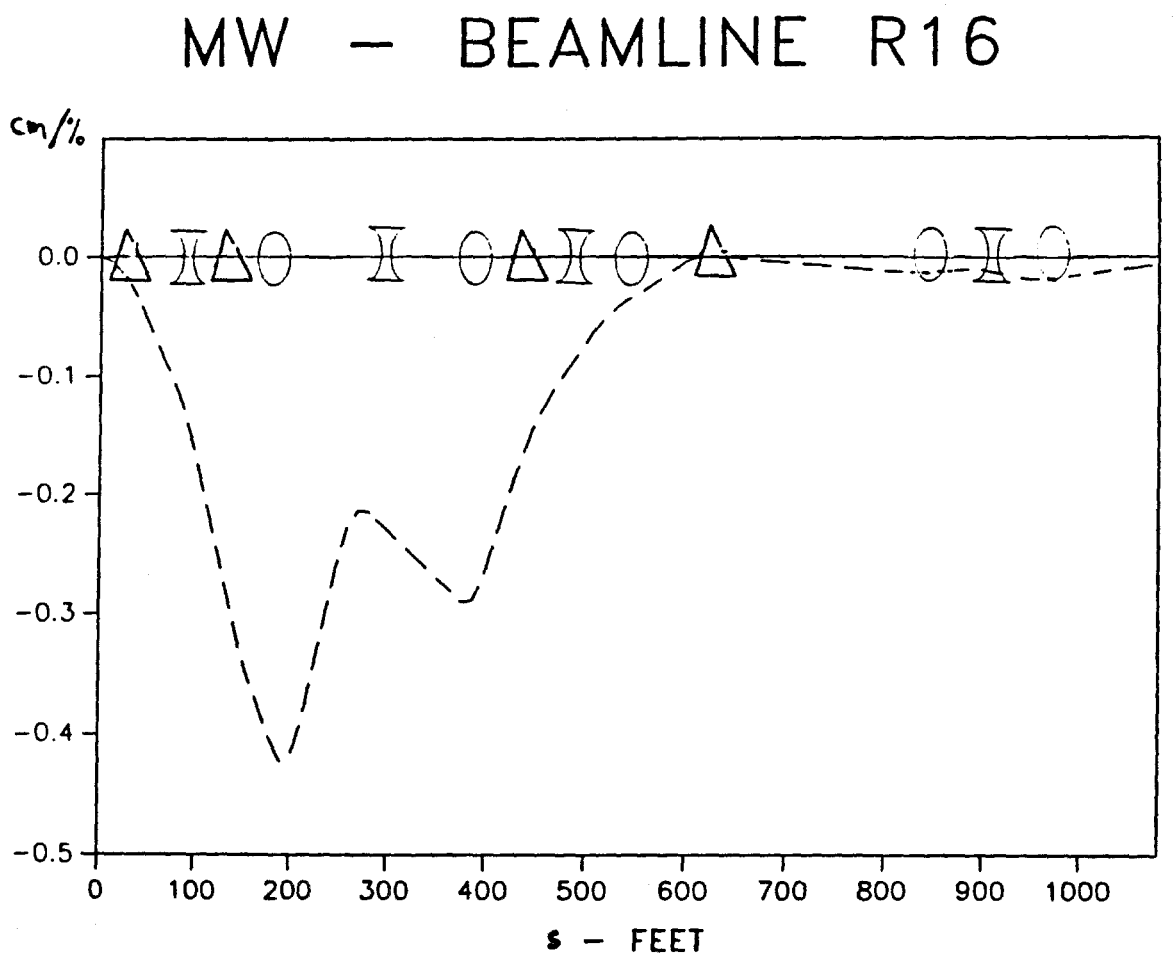

Figure 19: R_{16} matrix element for the MW-beamline plotted versus the longitudinal distance s along the beamline.

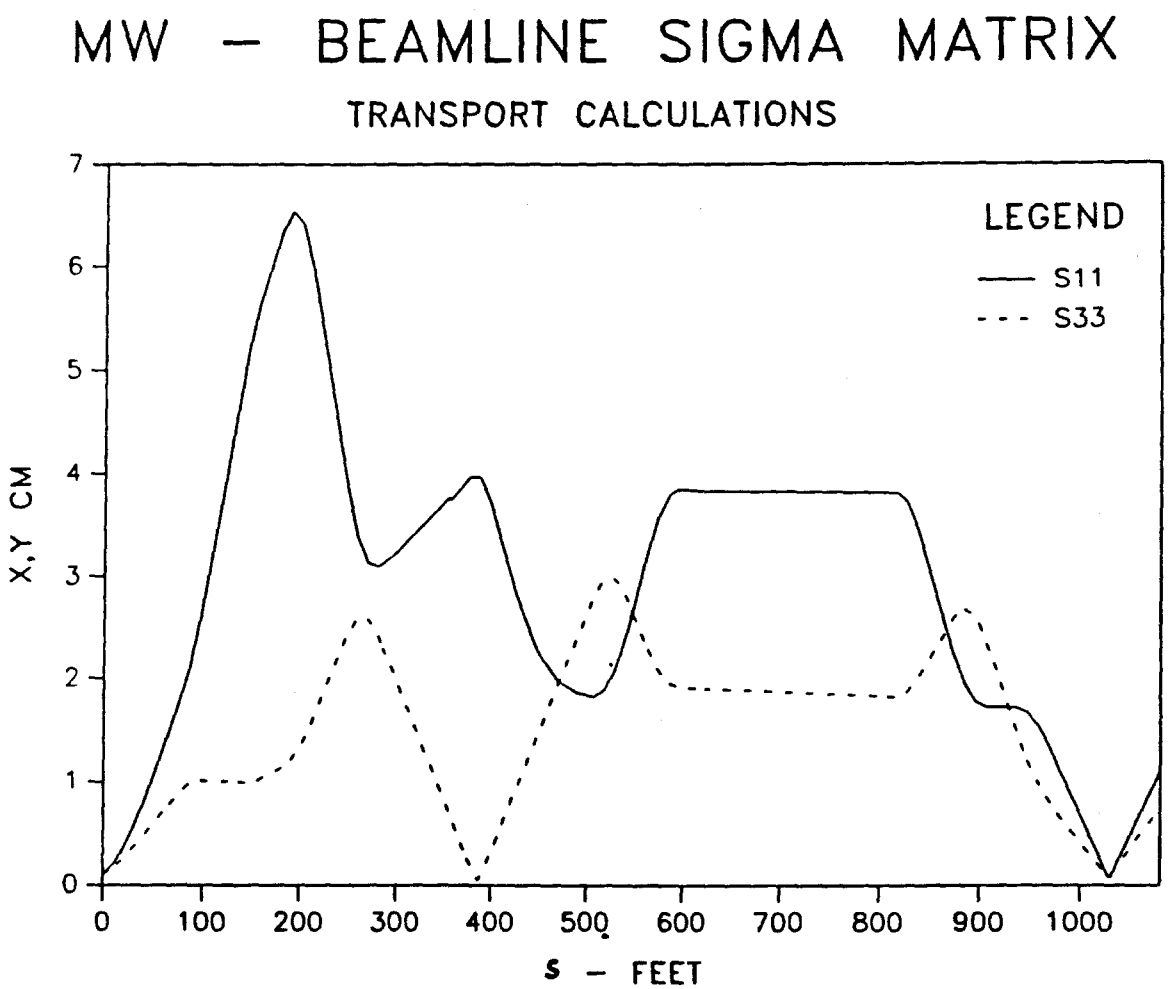

Figure 20: $\sqrt{\sigma_{11}}$ and $\sqrt{\sigma_{33}}$ matrix elements for the MW-beamline plotted versus the longitudinal distance s along the beamline.

The primary 800 GeV proton beam at the MW primary production target has the following parameters

$$(\Delta x) = 1 \text{ mm}, \quad (\Delta y) = 1 \text{ mm}, \quad \text{and} \quad (\Delta p/p) = 0.1\% \tag{3.35}$$

where the numbers refer to the total extent. The profile of the primary beam in the horizontal and vertical planes as recorded just upstream the MW production target is shown in Fig. 21.

The phase space acceptance of the MW beamline was calculated to be

$$(x_0, x_0', y_0, y_0', \delta, \Delta p/p) = (0.1 \text{ cm}, 0.51 \text{ mrad}, 0.1 \text{ cm}, 0.38 \text{ mrad}, 0.0, 12.5\%) \tag{3.36}$$

The beamline angular acceptance with all collimators wide open was 0.61μsr and the total acceptance was 8μsr%. For the positive running mode the collimator MW7CH2 was closed to 0.5in. (FWHM) and the acceptance was 0.5μsr%.

TURTLE was also used to determine the beam profile in the horizontal and vertical planes, the momentum distribution in the horizontal plane, and the beam divergence for the different secondary momenta and running modes. The beam profiles in x and y at the experimental target as calculated by TURTLE and the beam profiles obtained by the SSDs' are plotted in Fig. 22, 23. The calculated momentum distributions for the two beam running modes (positive, negative) at 530 GeV are plotted in Figs. 24, 25. Also shown on these figures are Gaussian fits to the distributions. According to those plots, the momentum bite of the beam was $\Delta p/p = \pm 7.0\%$ HWHM for the negative mode and $\Delta p/p = \pm 1.6\%$ HWHM for the positive mode.

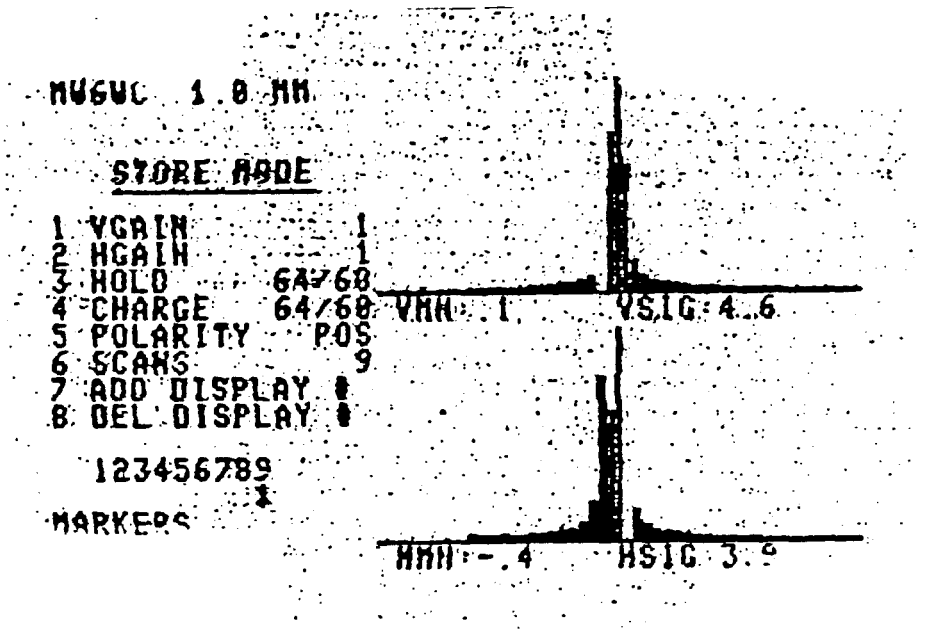

Figure 21: Profile of the Primary 800 GeV proton beam before the MW-Primary target. (top): Horizontal plane. (bottom): Vertical plane.

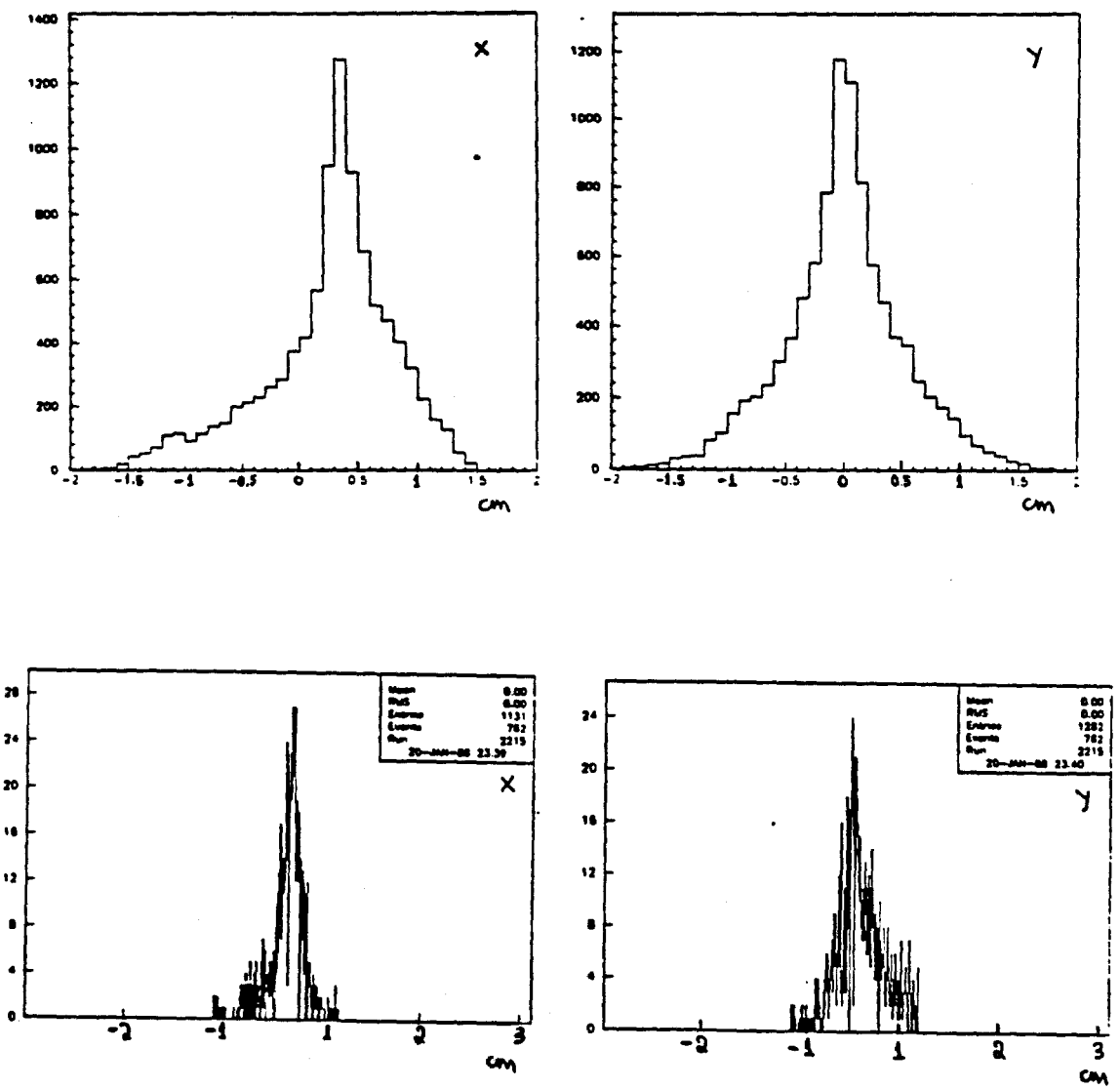

Figure 22: Beam profiles at the experimental target for the negative running mode. (top): TURTLE calculations. (bottom): SSD profiles.

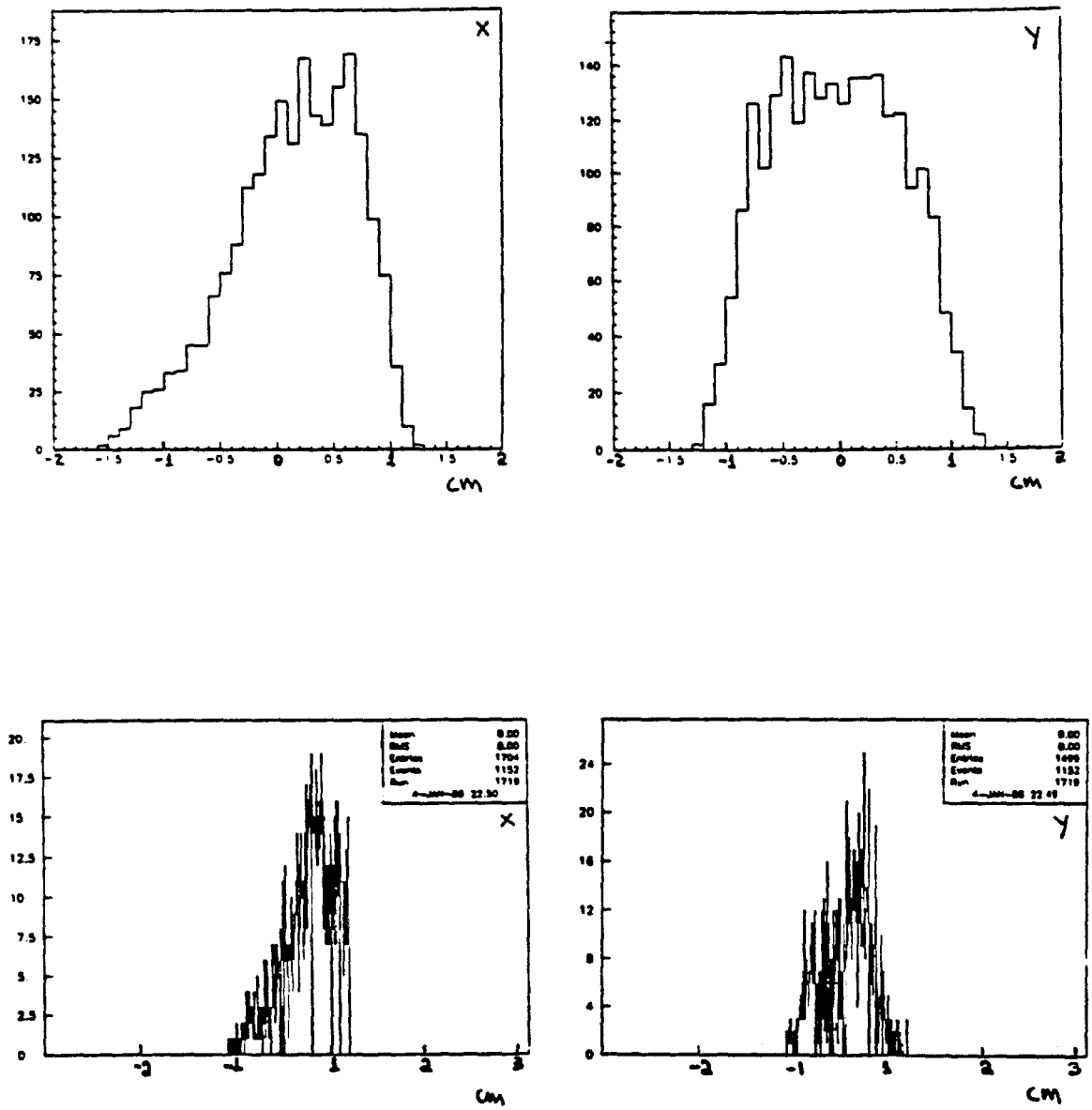

Figure 23: Beam profiles at the experimental target for the positive running mode. (top): TURTLE calculations. (bottom): SSD profiles.

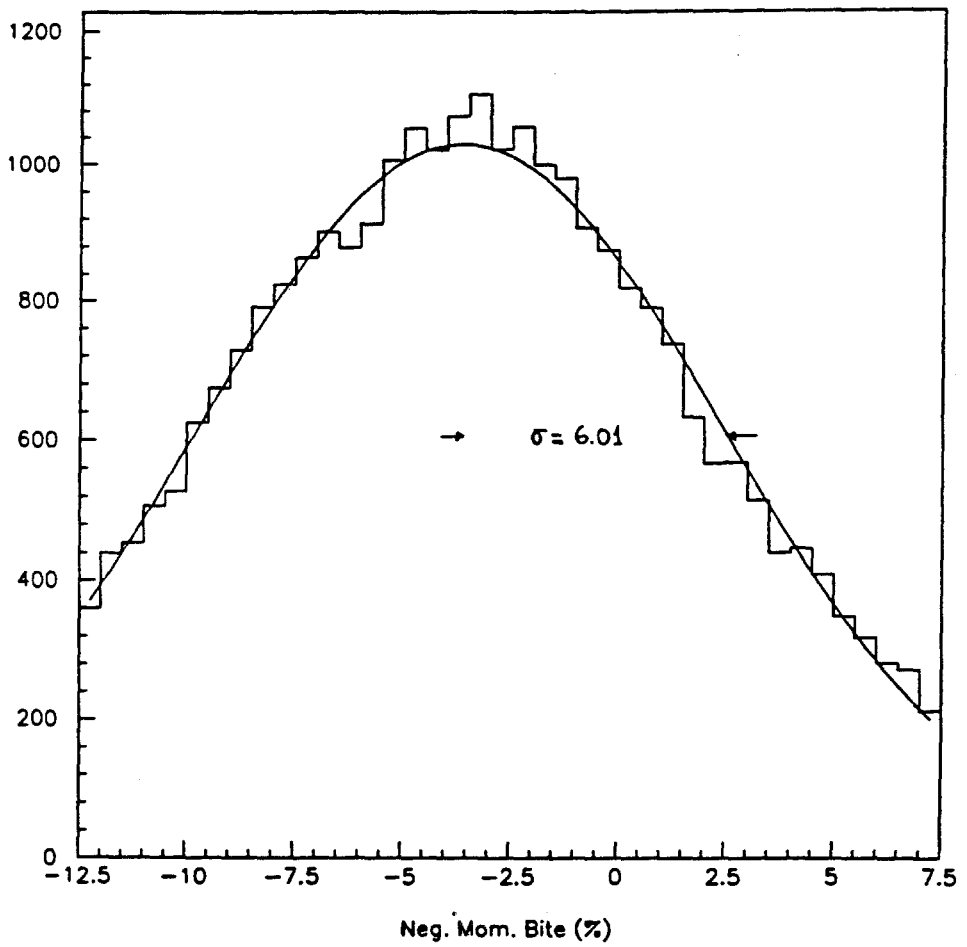

Figure 24: Beam momentum distribution for the negative running mode calculated by TURTLE.

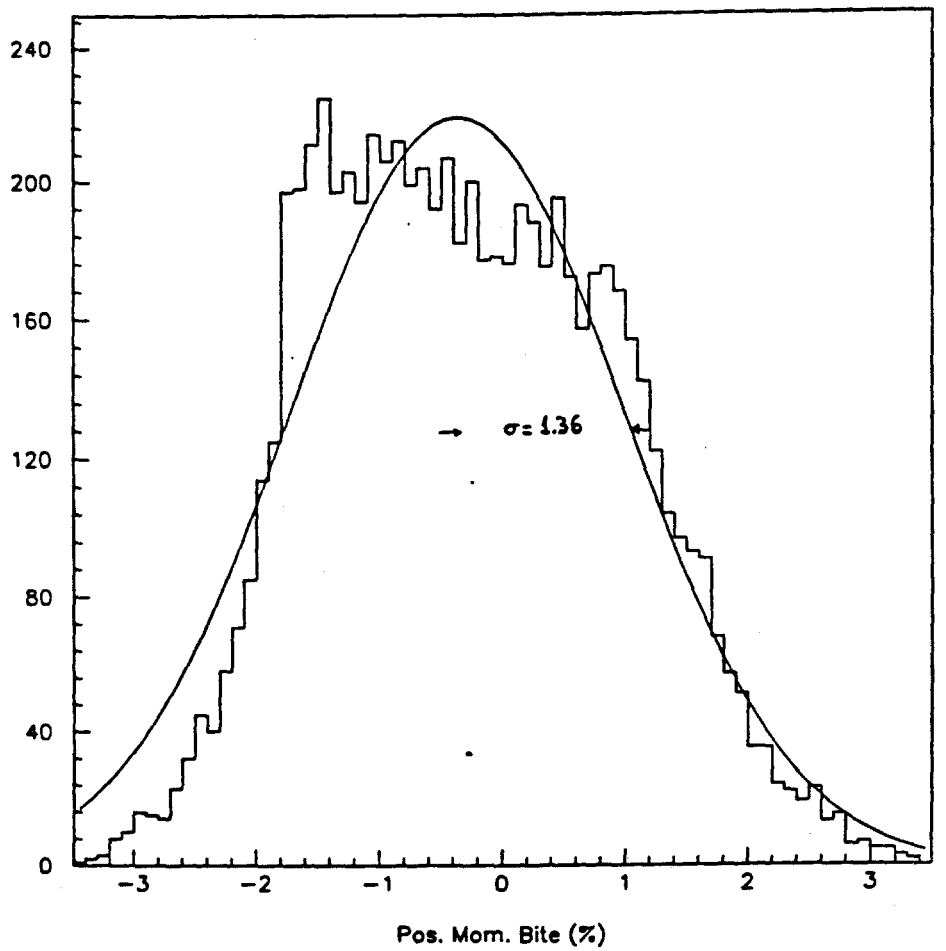

Figure 25: Beam momentum distribution for the positive running mode calculated by TURTLE.

The TRANSPORT and TURTLE calculations (tunes), produce optimum magnet current settings and collimator positions which transport secondary particle beams with the maximum possible yields, optimum beam profiles at the final target area and a high degree of parallelism in the region of the Cherenkov counter.

These tunes are the starting point for the actual tuning of the beamline which is an extremely time consuming process requiring a certain amount of hands-on experience. A beamline's actual tunes are continually improved upon and are redone when the beamline configuration is changed or the primary beam is altered by the Switchyard.

For the MW beamline, nominal tunes were first determined using TRANSPORT for the 530 GeV secondary momentum. The tunes for the other secondary momenta were determined, to the first order, by simply scaling down the optimum experimental 530 GeV tune using the magnets excitation curves.

3.5. Particle Yields

An empirical particle production formula has been used in the TURTLE program to calculate particle yields for secondary high energy beamlines. The particle production formula is for proton beams interacting with thick targets (up to one interaction length) and was developed by A. Malensek[53],[54] by fitting the experimental data taken by Atherton et al.[23], who made precise measurements of particle production from 400 GeV protons incident on Be targets.

According to Malensek's formula the number of particles produced per (sr-GeV-

incident proton) on a 500 mm Be target is given by

$$\frac{\partial^2 N}{\partial P \partial \Omega} = Kp\frac{(1-X)^A(1+5e^{-DX})}{(1+p_t/M^2)^4} \tag{3.37}$$

where

K=B/400

X=p/p_{inc}

p=laboratory momentum of the produced particle

p_{inc}=incident primary proton momentum

p_t=transverse momentum of the produced particle

and A, B, D, and M^2 are constants dependent on the particle produced and are given in reference [53]. This formula fits the data within 20%[53].

The original formula can be modified for other target lengths and materials. To correct for different target lengths (still assuming a Be target) of thickness L (in cm), the empirical formula is multiplied by the factor $f^s(L)/f^s(50)$, where f^s is the target production efficiency given by

$$f^s(L) = \frac{e^{-L/\lambda_S} - e^{-L/\lambda_p}}{1-\frac{\lambda_p}{\lambda_S}} \tag{3.38}$$

where λ_S is the absorption length (in cm) for the produced secondary particles (which may be protons) and λ_p is the absorption length for protons. This formula is based on the simple model where the produced secondary either escapes the material or is absorbed with no daughter particles created. This is a reasonable model as long as the target is about one interaction length or less. For secondary

proton production, $\lambda_S = \lambda_p$ and Eq. 3.14 simplifies to

$$f^p(L) = \frac{1}{\lambda_p} e^{-L/\lambda_p} \tag{3.39}$$

All the λ_S are taken from Carrol et al.[57]. Figure 26 shows a plot of Be target production efficiency f^s versus L/λ_S for production of π^-, where L is the target thickness and λ_S is the absorption length for π^- in Be. This plot can be used to determine necessary target thickness for other materials besides Be.

To correct for different target materials, plots of conversion factors versus A and X that are given by Ref. [53] are used to multiply the empirical formula, Eq. (3.13), for the final result.

Application of the empirical formula gives the initial beam flux at the end of the target. To determine the beam flux at another point downstream of the target, the initial flux is integrated over the accepted phase space region for the point of the beamline being considered. Special packages of TURTLE including Malensek's empirical formula are used to calculate the rate of secondary hadron production from the target per interacting proton, plus the fraction of these particles which reach the final target area. Decay is also taken into account. The result need only be corrected for the target production efficiency and for target materials other than Be.

Using the package of TURTLE with the above procedure, we calculated the yields at the experimental target for different particles (π^-, K^-, $\bar{p}$) and different beam momenta for the MW-beamline and the negative running mode. The results are summarized in the Table 2, below.

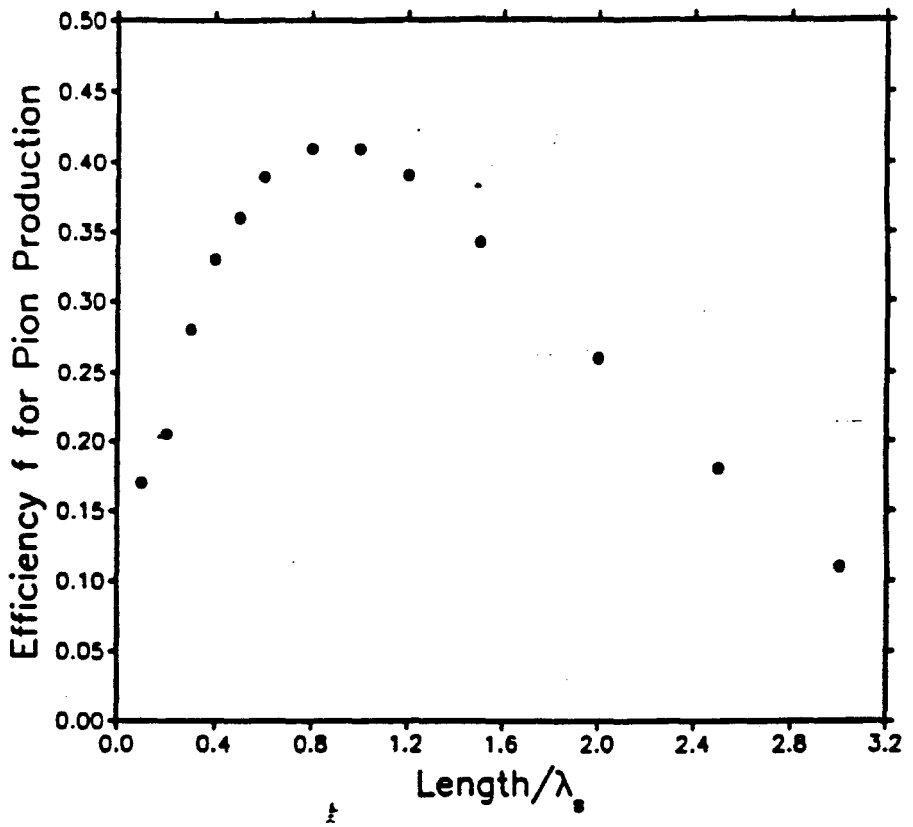

Figure 26: Berylium target production efficiency f versus L/λ_s.

TABLE 2				
P (GeV)	π^-	K^-	$\bar{p}$	Total
25	3.7×10^7	5.7×10^6	2.1×10^6	4.5×10^7
50	1.2×10^8	1.6×10^7	6.2×10^6	1.4×10^8
100	2.4×10^8	2.3×10^7	7.2×10^6	2.7×10^8
200	2.6×10^8	2.3×10^7	5.9×10^6	2.8×10^8
300	2.1×10^8	1.6×10^7	2.8×10^6	2.3×10^8
400	1.3×10^8	6.3×10^6	9.0×10^5	1.4×10^8
530	4.1×10^7	1.0×10^6	8.0×10^4	4.2×10^7

TABLE 2: Negative particle yields for 10^{12} incident 800 GeV primary protons on the 3/4 interaction length Al target.

The total negative particle yield at the experimental target at 530 GeV from the 3/4 interaction length Al target was measured and found 2.4×10^7 particles per 10^{12} inc. protons which is a factor of 1.75 less than the calculated total particle yield from TURTLE and is considered acceptable for this kind of calculation.

In the positive running mode, the production angle was 1.4 mrad. A modified version of TURTLE was used in order to calculate the positive particle yields. The results are summarized in Table 3. The total positive particle yield from the long (3/4 interaction length) Al target at 530 GeV, was not measured directly, because of radiation problems. Instead, we used a smaller W target (1/10 interaction length) to measure the total yield as a function of the momentum slit collimator MW7CH2, and compared the yields from the two targets at a fixed MW7CH2 position (0.58″). We estimated the total positive yield from the 3/4 interaction Al target at 530 GeV to be 1.5×10^8 particles per 10^{12} incident protons which is

a factor of 3.6 times less than the calculated one. The hadron yields for the MW beamline for 10^{12} incident protons on the 3/4 interaction Al target versus beam momentum are plotted in Fig. 27. The yields were normalized to the measured E706 values at 530 GeV.

TABLE 3				
P (GeV)	π^+	K^+	p	Total
100	2.7×10^8	3.5×10^7	6.0×10^7	2.7×10^8
200	3.8×10^8	5.1×10^7	2.3×10^8	6.6×10^8
300	2.4×10^8	4.7×10^7	4.1×10^8	7.0×10^8
400	1.3×10^8	2.9×10^7	5.2×10^8	6.8×10^8
530	3.1×10^7	9.7×10^6	5.0×10^8	5.4×10^8

TABLE 3: Positive particle yields for 10^{12} incident 800 GeV protons on the 3/4 interaction length Al target.

We used RAYGEL to calculate electron production rates from the normal cascade processes in the long (3/4 interaction Al) production target. The number of π°s is chosen to be $\frac{1}{2}(\pi^+ + \pi^-)$ and the Malensek empirical formula is used to calculate the π^+ and π^- rates. The results are summarized in Table 4, which follows.

TABLE 4		
P (GeV)	e^-	e^-/Total %
25	1.3×10^8	74
50	1.2×10^8	46
100	7.2×10^7	21
200	1.6×10^8	5.0

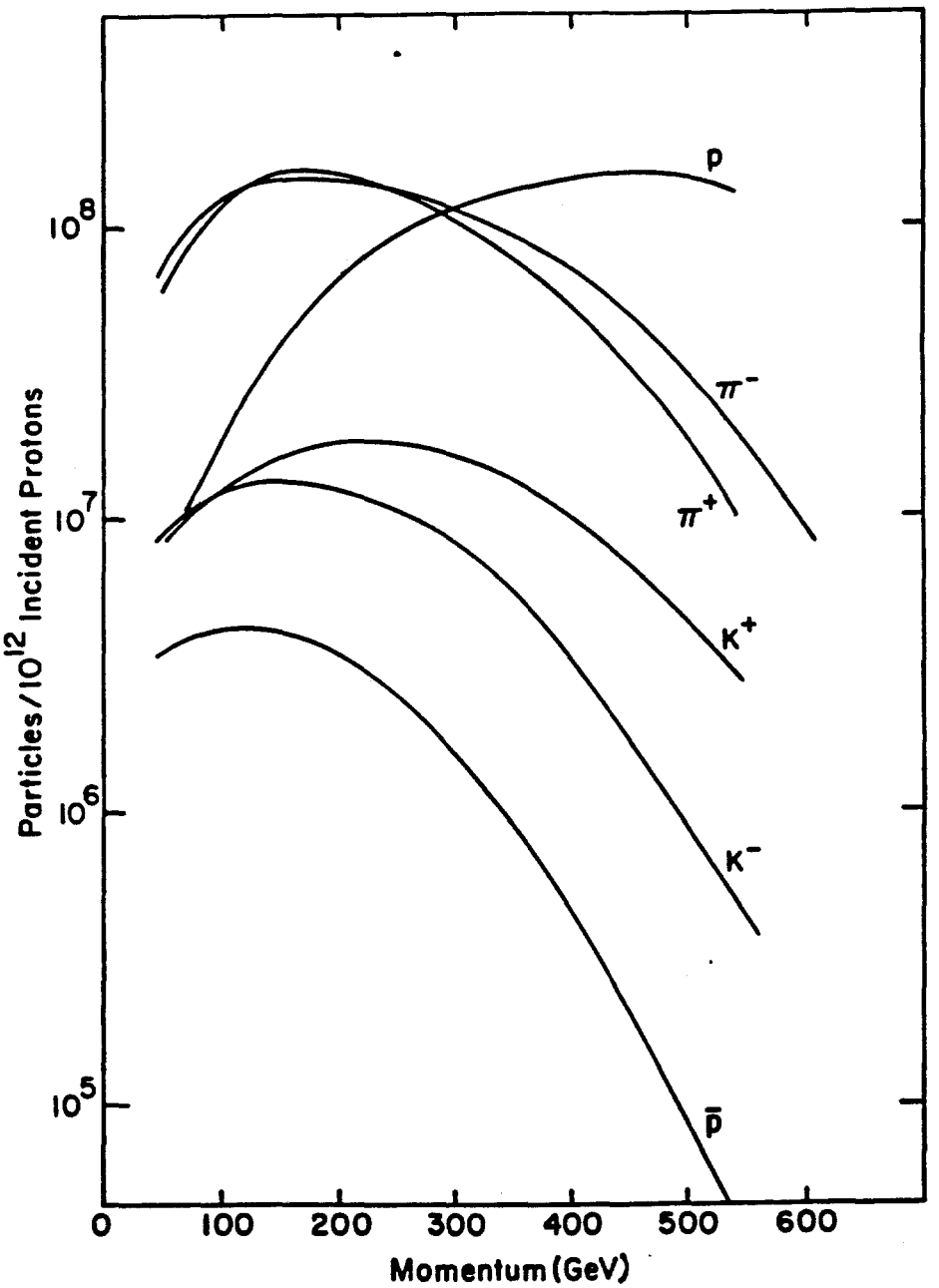

Figure 27: Calculated particle yields for the MW-beamline (3/4 interaction Al target), normalized to the E706 measurements at 530 GeV.

TABLE 4: Electron yields for 10^{12} incident 800 GeV primary protons on the 3/4 interaction length Al target.*

The electron yields were not measured directly. An estimation of the percentage of electrons in the beam for various momenta was done by looking at the energies deposited in the electromagnetic and hadron calorimeter. Charged particles that deposited all their energy in the electromagnetic calorimeter, were called electrons. The energy deposited in both calorimeters (EMLAC/HALAC) and the energy deposited only in the electromagnetic calorimeter for 50, 100 and 200 GeV, are plotted in Figures 28, 29, and 30 respectively.

According to that method the percentage of electrons in the beam is measured to be 38%, 22%, and 5.7% for 50, 100 and 200 GeV secondary momenta respectively. The measured values are within 20% of the calculated ones.

---

* RAYGEL does not take into account the effect of synchrotron radiation which becomes important for very high energy electrons going through large magnetic fields. The energy δE lost by an electron of energy E bent through a circular arc by a dipole magnet of length L and with a uniform magnetic field of strength B is given by

$$\delta E[MeV] = 0.0013(E[GeV])^2(B[T])^2(L[m]) \tag{3.40}$$

The MW beamline has only a few bends and the bend angles are small so the effect of the synchrotron radiation is very small. For example, the total energy δE lost by synchrotron radiation from a 100 GeV electron in the MW beamline is $\delta E^s_{100} = 10.75 MeV$, while the energy loss by a 200 GeV electron is $\delta E^s_{200} = 171 MeV$.

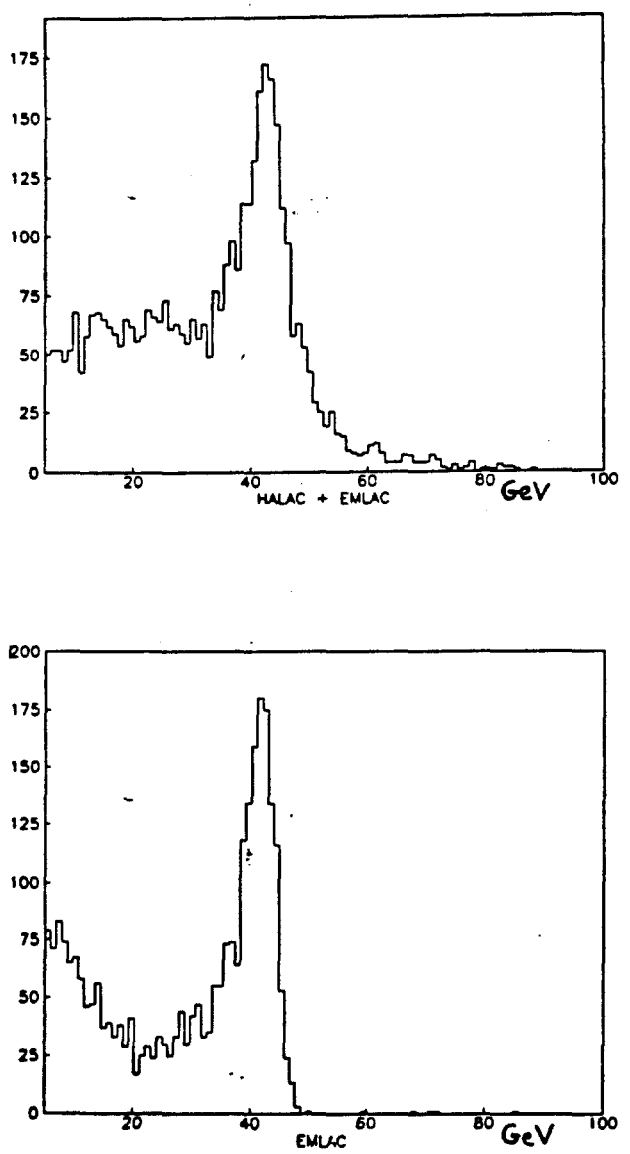

Figure 28: (top): Energy deposited in the whole calorimeter for the 50 GeV calibration run. (bottom): Energy deposited in the electromagnetic calorimeter for the 50 GeV calibration run.

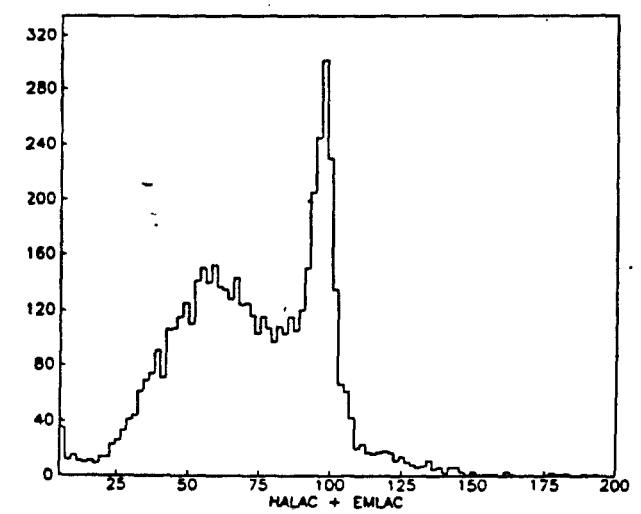

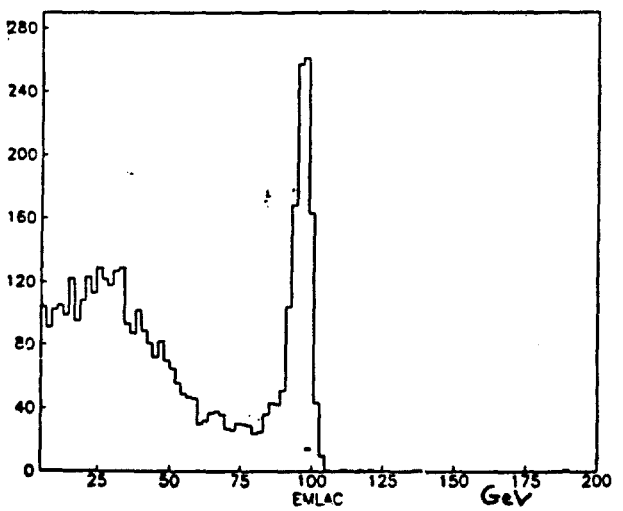

Figure 29: (top): Energy deposited in the whole calorimeter for the 100 GeV calibration run. (bottom): Energy deposited in the electromagnetic calorimeter for the 100 GeV calibration run.

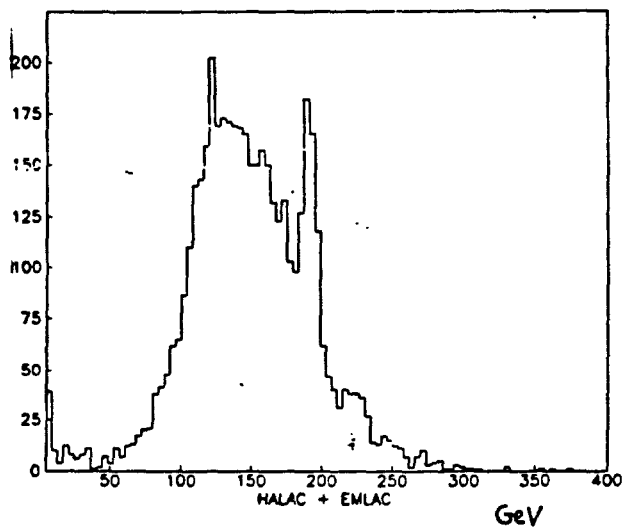

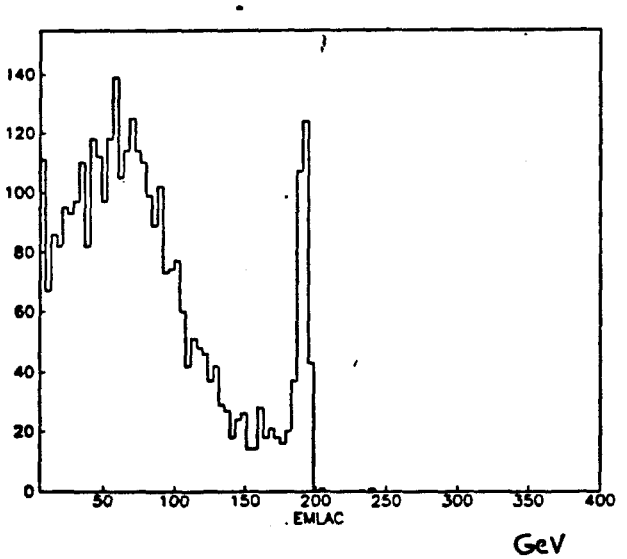

Figure 30: (top): Energy deposited in the whole calorimeter for the 200 GeV calibration run. (bottom): Energy deposited in the electromagnetic calorimeter for the 200 GeV calibration run.

3.6. Absolute Beam Momentum

The absolute beam momenta were determined from the currents in the bending magnets in the beamline (MW7W1, MW7W2-1,2). The currents values were converted to magnetic field values using the excitation curves of the magnets[55]. The absolute momentum of the beam was calculated from the magnetic field values and the nominal bending angle of each magnet. Table 5 lists the calculated absolute momentum values next to the nominal ones. Through out this thesis I will be using the nominal values.

TABLE 5	
BEAM MOMENTUM (GeV)	
Nominal Value	Calculated Value
50	56.4±0.6
100	102.8±0.8
200	189.±1.
400	379.±3.
530	508.±5.

TABLE 5: Quoted and calculated values of the beam momentum.

4. MW-CHERENKOV COUNTER

In this chapter, I will first describe the main characteristics of a Cherenkov counter that determine its performance and then the MW-Cherenkov counter itself. Finally, I will describe how the MW-Cherenkov was used to tag the minority particles during the E706 run.

4.1. INTRODUCTION

Cherenkov radiation was discovered in 1943 by Vavilov and Cherenkov[58] and was explained theoretically by Tamm and Frank[59] in 1937 who developed a classical theory to account for the radiation. A quantum-mechanical theory of the effect was given by Ginsburg[60] in 1940.

The relation between the angle of Cherenkov radiation, θ, the velocity of the particle, β, and the refractive index of the miedium, $\eta(\lambda)$, is:

$$\cos\theta = \frac{1}{\beta\eta(\lambda)} \tag{4.1}$$

Relation (4.1) can be rewritten as:

$$\cos\theta(\lambda) = \frac{v_{\text{light}}}{v_{\text{particle}}} \tag{4.2}$$

which shows that the angle of emission of light is directly related to the ratio of the

velocity of light in the radiator to the particle velocity. The optical measurement of the emission angle of the light, along with the knowledge of the velocity of light in the same medium, determines the velocity of a particle. For high-energy charged particles, measuring their relative velocity β via Cherenkov radiation together with an independent determination of their momenta p is practically the primary way to identify the particles.

By using the Cherenkov effect, the velocity can be measured to a percentage accuracy in the range of 10^{-3} to 10^{-7}, with the corresponding accuracy in mass, m, of a single particle given by:

$$dm/m = \gamma^2(d\beta/\beta) + (dp/p) \tag{4.3}$$

where dp/p is the momentum spread of the beamline. Due to the large γ^2 factor at high energies, the ability to identify particles by this mass definition is limited by the velocity resolution of the particular Cherenkov detector.

There are three basic types of Cherenkov detectors that are used for particle identification at high energies[61]:

a) *The threshold counter*, which is used to detect particles that have velocity β above a given threshold velocity β_0.

b) *The differential counter*, which distinguishes among different particles by the angle of their Cherenkov light. In a differential counter the reflected ring of Cherenkov light is focused into an annular diaphragm. The light that passes through the aperture of the diaphragm is detected by a number of photomultipliers equally spaced around the annulus.

c) *The differential isochronous self-collimating counter (DISC)*, which is a differential counter equipped with an optical system which corrects for geometric and chromatic aberrations.

All three types of counters are illustrated schematically in Fig. 31.

In a high energy beam of momentum p the velocity resolution $\Delta\beta$ of a Cherenkov counter is defined in terms of the range of the Cherenkov angle accepted by the counter:

$$\Delta\beta = \tan\theta \; \Delta\theta \tag{4.4}$$

The approximate velocity difference $\Delta\beta_{m_0 m_1}$ between two particles with masses m_0, and m_1 and the same momentum is given by

$$\Delta\beta_{m_0 m_1} = \frac{(m_1^2 - m_0^2)}{2p^2}, \tag{4.5}$$

with $m_1 > m_0$.

The limiting mass separation of a Cherenkov counter corresponds to the finest velocity resolution $\Delta\beta_{limit}$ that the counter can achieve. For the limiting separation of two particles one must have:

$$\Delta\beta_{limit} = \Delta\beta_{m_0 m_1} \tag{4.5}$$

In practice, $\Delta\beta_{limit}$ is chosen so that

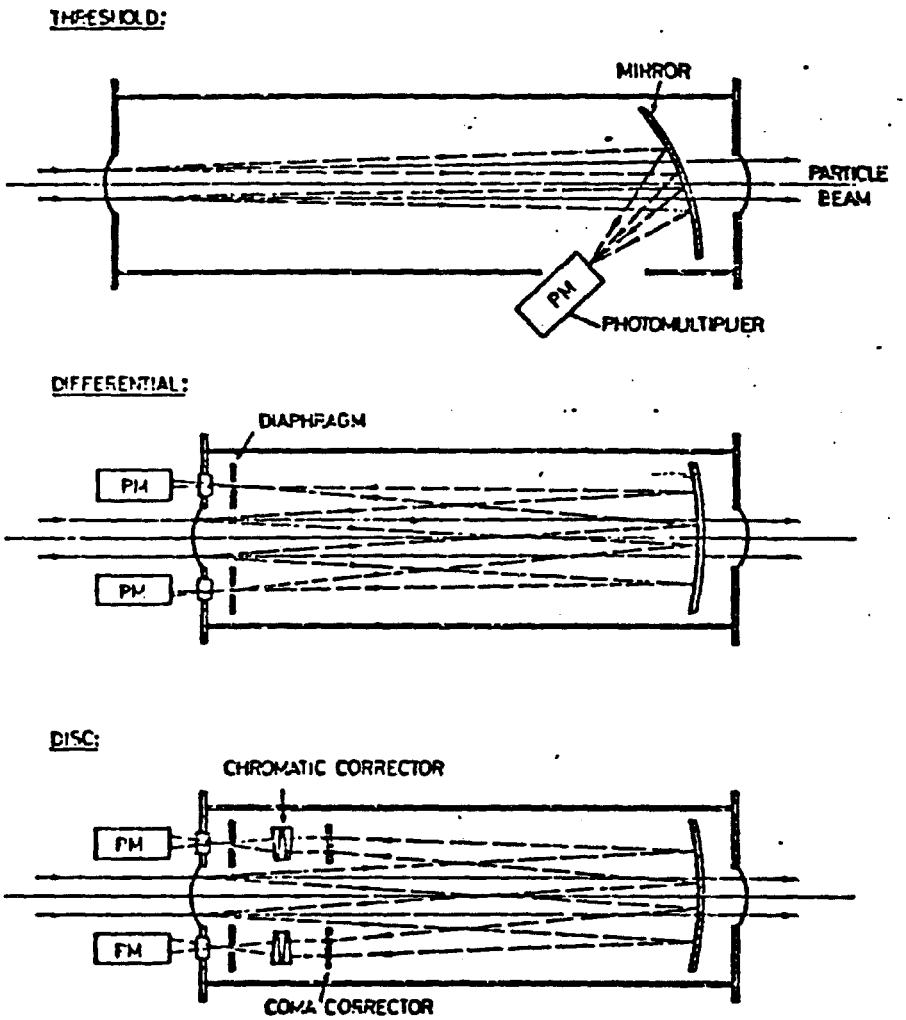

Figure 31: Basic Types of Cherenkov Detectors.

$$\Delta\beta_{limit} = \frac{1}{4}\Delta\beta_{m_0 m_1} \tag{4.6}$$

As a numerical example, the mass separation between pions and kaons at 300 GeV is $\Delta\beta_{m_0 m_1} \sim 10^{-6}$. To resolve between pions and kaons at this energy using a Cherenkov counter demands a small value for the Cherenkov angle from Eq. (4.4), and consequently a small value of the refraction index $(\eta - 1)$. Therefore at high energies one considers only gas-filled Cherenkov counters.

Before I go on to describe the MW Cherenkov counter I will discuss the main characteristics that determine the performance of a Cherenkov counter.

4.2. Performance Characteristics of a Cherenkov Counter

4.2.1 The light yield

The number of photons N per unit wavelength λ in a counter of finite length L is given by:

$$\frac{d^2N}{d\lambda d\cos\theta} = \frac{z^2 2\pi\alpha}{\lambda}\left(\frac{L}{\lambda}\right)^2\left(\frac{\sin\chi}{\chi}\right)^2\sin^2\theta, \tag{4.8}$$

where

$$\chi(\theta) = \pi\frac{L}{\lambda}\left(\frac{1}{\eta(\lambda)\beta} - \cos\theta\right), \tag{4.9}$$

ze is the charge of the particle, α is the fine structure constant and $\eta(\lambda)$ is the refraction index of the radiator.

In the limit $(L/\lambda \rightarrow \infty)$, $\sin\chi/\chi$ becomes a δ-function and

$$\frac{d^2N}{d\lambda\, d\cos\theta} = \frac{z^2 2\pi\alpha}{\lambda}\delta(\chi)\left(\frac{L}{\lambda}\right)^2\sin^2\theta \tag{4.10}$$

which, when the δ-function is integrated over all angles, reduces to:

$$\frac{dN}{d\lambda} = \frac{z^2 2\pi\alpha}{\lambda^2}L\sin^2\theta \tag{4.11}$$

Due to the z^2 dependence, a particle with a large charge can generate sufficient Cherenkov light intensity to be recorded on photographic emulsion. However, for

singly charged particles, the light yield is quite small. For example, the energy loss by Cherenkov radiation in the wavelength bandwidth from 200 to 600 nm is about $1keV$, which is about 100 times less than the energy loss by ionization.

As we see from Eq. (4.11), the light yield is proportional to the length of the radiator and increases with decreasing wavelengths. Thus, many efforts have been made to improve the light transmission and extend the sensitivity of the photodetector into the ultraviolet region where the number of photons is greater. At long wavelengths the detection by the counter is limited not only by the reduced Cherenkov light emission but also by the cut off threshold of the photomultiplier photocathodes.

4.2.2 Quantum Efficiency and Noise

The detection efficiency of a given Cherenkov counter is obtained by folding the quantum efficiency of the photodetector used with the optical transmission properties of the counter, both of which are a function the Cherenkov light spectrum. By using ultraviolet-transmitting materials such as fused silica, the Cherenkov light can be detected to wavelengths of about 150 nm.

The effective detector efficiency of a photodetector and its the associated electronic equipment can be measured if one knows the bandwidth to be transmitted by the standard Cherenkov optics. The standard Cherenkov optics are those that are used in conventional threshold counters and consist of: (a) one front-aluminized mirror, especially coated for reflection at ultraviolet wavelengths and containing a

protective interference layer of $\lambda/2$ thickness of MgF_2 at 350 nm, and (b) one exit window of ultraviolet-transmitting fused silica which has an antireflection coating of a layer of $\lambda/4$ thickness of MgF_2 at 350 nm. With this standard set of Cherenkov optics it is possible to experimentally measure and compare the performances of different types of photomultipliers.

For a Cherenkov counter of length L and Cherenkov angle θ, the number of photoelectrons N produced by the passage of a single charged high-energy particle is given by:

$$N = AL\theta^2 \tag{4.12}$$

where A characterizes the photodetector, taking into account the Cherenkov light spectrum and the transmission properties of the optics. Values of the parameter A have been measured in several laboratories[62], and are in good agreement. The most sensitive photomultipliers available today, consisting of fused silica entrance window and a bialcali (K-Cs-Sb) photocathode, have a value of the parameter A from about 100-150 cm^{-1}. Photomultipliers having a photocathode of lower quantum efficiency and a UV-glass entrance window have a value of A from 50-60 cm^{-1}. For example, if L=42.1 m, θ=5.0 mrad and A = 150 cm^{-1} then Eq. (4.12) gives:

N = 16 Photoelectrons/particle

The noise pulses in a photomultiplier, mainly arising from single photoelectrons, are indistinguishable from true signals since the threshold of the detection electronics is generally set below that level. To avoid counting noise, in the differential type of Cherenkov counter, the light output is divided among several photomulti-

pliers, and their output signals required to satisfy a coincidence requirement. In this way the accidental count rate can be reduced to an extremely low level at the expense of reducing the overall counting efficiency of the detector.

For a differential Cherenkov counter with q photomultipliers, the efficiency for the q-fold coincidence is:

$$\epsilon_q = (1 - \epsilon^{-N/q})^q \tag{4.13}$$

where N is the number of photoelectrons.

For example, when q=6, $\epsilon_6 = 0.64$ for N=16 photoelectrons.

4.2.3 Optical Dispersion in the Radiator

In Eq. (4.1), the Cherenkov angle θ is a function of the wavelength λ of the light due to variation of the refractive index of the radiator as a function of λ. As a consequence, there is a spread or dispersion in the angle of the emitted photons due to variation of the refractive index of the radiator as a function of λ. The range of the chromatic dispersion is given by:

$$\Delta\theta_{DISP} = \frac{\Delta\eta}{\eta(\lambda)\tan\theta(\lambda)} \tag{4.14}$$

where $\Delta\eta$ is the change in refractive index over the range of the detectable wavelengths. If one defines an average wavelength λ_2 (which is the mean of the dis-

tribution of detected photoelectrons versus wavelength), and wavelengths λ_1, λ_3 corresponding to the limits of the spectral range, then

$$\Delta\theta_{DISP} = \frac{\eta(\lambda_2) - 1}{\eta(\lambda_2)\nu \tan\theta(\lambda_2)} \tag{4.15}$$

where

$$\nu = \frac{\eta(\lambda_2) - 1}{\eta(\lambda_1) - \eta(\lambda_3)} \tag{4.16}$$

The parameter ν characterizes the optical dispersion in the radiator. Table 6 contains values of the refractive index (at 1 atm and 20°C) and of the parameter ν for some commonly used gas radiators for wavelengths consistent with fused silica optics and the spectral response of a bialcali photocathode ($\lambda_1 = 280$ nm, $\lambda_2 = 350$ nm, $\lambda_3 = 440$ nm). As it is clear from the table, the inert gases have the largest values of ν and consequently the smallest chromatic dispersion.

TABLE 6

Gas	$(n_0 - 1) * 10^6$ [280 nm]	$(n_0 - 1) * 10^6$ [350 nm]	$(n_0 - 1) * 10^6$ [440 nm]	ν
He	33.27	32.90	32.67	54.5
Ne	64.07	63.37	62.85	52.2
H_2	140.6	135.3	132.0	15.7
N_2	294.8	287.0	282.0	22.5
CH_4	447.8	430.3	419.7	15.3

TABLE 6: Values of the parameter ν for some commonly used gas radiators.

A precise expression for the refractive index of inert gases as a function of

wavelength at $0°C$ and 760 mm Hg was obtained by Dalgano and Kingston[66]. This useful expression for He is:

$$\eta^2 - 1 = 6.927 * 10^{-5}\left(1 + \frac{2.24 * 10^5}{\lambda^2} + \frac{5.94 * 10^{10}}{\lambda^4} + \frac{1.72 * 10^{16}}{\lambda^6} + ...\right) \quad (4.17)$$

4.2.4 Optical Aberrations

Most differential Cherenkov counters use a spherical mirrors to reflect and focus the Cherenkov light onto an annular diaphragm.

In a differential counter, a spherical mirror of radius of curvature R and focal length $f(= R/2)$ focuses the cone of Cherenkov light in the differential counter into a ring image of radius r, given by:

$$r = f \tan\theta \quad (4.18)$$

The total radial spread Δr of the ring image is determined by the spherical and coma aberrations which to the third order, are given by:

$$\Delta r = \frac{-1}{8}\left(\frac{d}{f}\right)^3 + \frac{1}{8}\left(\frac{d}{f}\right)^2\theta \quad (4.19)$$

In this expression the first term is the spherical error, the second is the coma, d is the useful diameter of the mirror, f is the focal length and θ is the Cherenkov angle.

Thus, the angular broadening $\Delta\theta_{OPT}$ of the ring image due to the optical aberrations is given by:

$$\Delta\theta_{OPT} = \frac{\Delta r}{f} \tag{4.20}$$

4.2.5 Energy Loss, Scattering, and Diffraction Effects

As the particle traverses the radiator it loses energy, primarily by the process of ionization, which changes the value of its velocity β and hence the Cherenkov angle of the radiated light. However, the ionization loss, which is about 2MeV*g^{-1}*cm^{-2} for most materials, is negligible at relativistic energies. Multiple Coulomb scattering of the particle also causes a broadening of the Cherenkov angle. The angular spread $\Delta\theta_{MSC}$ (root mean squared projected angle) due to multiple scattering of a particle with momentum p can be expressed as[68]:

$$\Delta\theta_{MSC} = \left(\frac{14.1 \text{ Mev}}{p\beta}\right)\sqrt{\frac{L}{L_R}}\left[1 + \frac{1}{2}\log\left(\frac{L}{L_R}\right)\right] \tag{4.21}$$

where L is the radiator length and L_R its radiation length. For a gas radiator of length L, Eq.(4.21) can be rewritten as

$$\Delta\theta_{MSC} = \left(\frac{14.1 \text{ Mev}/c}{p\beta}\right)\left[\frac{\rho L(\eta - 1)}{(\eta_0 - 1)L_R}\right]^{\frac{1}{2}}, \tag{4.22}$$

where ρ is the gas density, L_R is the radiation length, η_0 is the refractive index

of the gas for a given wavelength of light at the temperature of the counter and pressure of 1 atm, and η is the refractive index at the same wavelength at the temperature and pressure of the counter.

The broadening of the Cherenkov angle $\Delta\theta_{DIFF}$ by diffraction is approximately given by:

$$\Delta\theta_{DIFF} = \frac{\lambda}{(L \sin\theta)} \tag{4.23}$$

where λ is the wavelength of light, L is the length of the radiator and θ is the Cherenkov angle. Since the gas-filled counters used to identify individual particles at ultra high energies operate at Cherenkov angles from 5 to 10 milliradians and are made tens of meters long (in order to obtain sufficient light) diffraction effects are negligible. For example the diffraction broadening for a 42.1 m long counter with θ=5 mrad and λ=350 nm is:

$$\Delta\theta_{DIFF} = 1.66 * 10^{-6} rads = 1.66 \mu rads$$

4.2.6 Finite Momentum Bite

Usually the beamlines where the Cherenkov counters are located are not monochromatic. The angular broadening of the Cherenkov light due to a finite momentum bite is given by:

$$\Delta\theta = \frac{(\Delta p/p)}{\theta}\left(\frac{m^2}{p^2}\right) \tag{4.24}$$

where $\Delta p/p$ is the momentum bite and m is the mass of the particle. From this relation we see that the larger the mass of the particle the larger the broadening. If θ=5 mrad and p=530 GeV, the broadening caused by a 10% momentum bite is

$\Delta\theta_{rms}$ = 1.4 μrad for π's, 17.3 μrad for K's, and 62.6 μrad for p's.

2.7 Beam Divergence

Any divergence in the beam will broaden the angular width of the Cherenkov cone by an equal amount. This is the reason that most Cherenkov counters are located in the parallel sections of the beamlines where the divergence of the beam is deliberately minimized. Typical values for beam divergence in the parallel sections of a beamline are about 0.02–0.10 mrad. The beam divergence in the MW-Beamline varied between 0.025–0.065 mrad depending on the running mode.

4.2.8 Thermal Stability

For Cherenkov counters which employ a gas radiator, one changes the refractive index merely by changing the operating pressure of the counter. The resulting change in the index is given by the Lorentz-Lorenz law:

$$\frac{(\eta^2 - 1)}{(\eta^2 + 2)} = \left(\frac{R}{M}\right)\rho \tag{4.25}$$

where R is the molecular refractivity, M is the molecular weight, and ρ is the gas density. For pressures that are not too high (less than 3 atm) Eq. (4.25) can be approximated by:

$$(\eta - 1) = (\eta_0 - 1)P \tag{4.26}$$

where η_0 is the refractive index of the gas for a given wavelength of light, at the temperature of the counter, and at a pressure of 1 atm. The pressure P is in atmospheres. From the last equation we see that the refractive index depends upon the gas density, which depends upon the temperature and pressure according to the equation of state of the gas. Any temperature gradient along the counter can cause variations in the index of refraction and degrade the velocity resolution achievable by the counter. It turns out that:

$$\frac{\Delta\rho}{\rho} = \frac{\Delta P}{P} = -\frac{\Delta T}{T} = \frac{\Delta\beta}{\frac{1}{2}\theta^2} \tag{4.27}$$

where ρ is the gas density, P the pressure and T the temperature. So in order to achieve a resolution of $\Delta\beta = 10^{-7}$ with a Cherenkov angle of 5 mrad we must have a $\Delta T = 2°\mathrm{C}$ or smaller along the length of the counter.

4.3. The MW Cherenkov Detector

4.3.1 General description

The MW-Cherenkov detector is a gas filled differential counter without an achromatizer. It has however a second larger radius annulus of photodetectors which can be used as an additional particle detection channel or for a veto channel. It is sits in the 67 m long parallel section of the MW-beamline, 708.44 ft (215.93 m) downstream of the MW primary target, and 320.8 ft (97.8m) upstream of the experimental target.

The counter has a total radiator length of 130 ft (42.1 m) and the Cherenkov angle is 4.998 mrad. The counter's pressure vessel consists of two 36 ft. and two 18 ft. stainless steel pipe sections bolted together, plus two 15 ft long aluminum extension pipes at the upstream end to give it a longer radiator length. The inner diameter of the steel pieces is 19.250 in. (48.89cm) and the thickness is 0.375 in. (0.95cm) (Fig. 32).

The counter uses a long (1275.5 in.) focal length mirror to focus the light and two rings at different radii, each with 6 photomultipliers to collect the light. The inner ring of photomultipliers (designated as the coincidence channel) has a radius of 6 3/8 in. (10.19 cm) and the outer ring (anticoincidence or veto channel) has a radius of 7 5/8 in. (19.3 cm).

The counter used He as radiator and the index of refraction was changed by changing the gas pressure. The vessel was checked for leaks and could maintain a

vacuum of 1 mTorr with a rate of rise of 1 mTorr per day. The operating pressure was 4-7 psia and was read remotely by two pressure transducers with an accuracy of ± 0.01 psia. However it was possible to attain 1.2 atm (17 psia) before the pressure relief valve blew. We used two 0.01 in. thick Ti foils for the entrance and exit windows of the counter. Two 4×4 in.^{2} scintillation counters, one upstream and one downstream of the Cherenkov counter, were used in coincidence to define beam particles which passed through the entire counter.

Finally, the vessel of the counter was covered by a 1 in. thick layer of Flex-Sulation X (a foam plastic material) for thermal insulation. The temperature inside the counter was monitored by 6 platinum RTD (resistant transition detectors) that were placed every 18 ft along the counter and measured the temperature with an accuracy of $\pm 0.2°$C.

The MW Cherenkov counter was designed to separate pions from protons at a 530 Gev beam momentum, but the final performance of the counter was such that we were also able to separate pions from kaons. In Table 7 I tabulate the effects the various performance characteristics discussed previously had on the resolution of the MW Cherenkov counter at a 530 GeV mean momentum. We also list the π-K and π-p separation at 530 GeV for comparison.

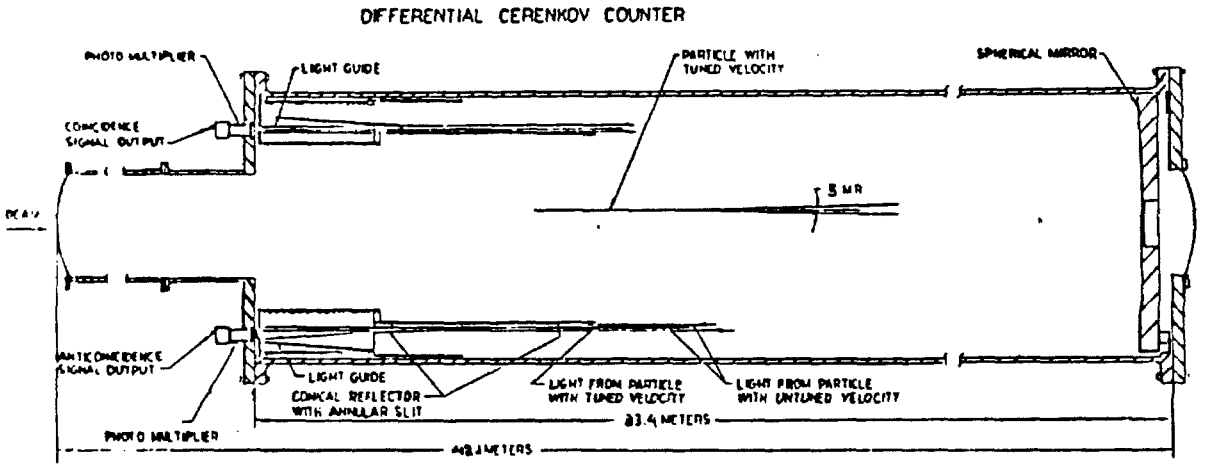

Figure 32: MW Cherenkov counter.

TABLE 7			
Parameter	$\Delta\beta$	$\Delta\theta(mr)$	$\Delta r(mm)$
π p Separation	1.53×10^{-6}	0.306	9.9
π K Separation	4.04×10^{-7}	0.081	2.6
Beam Divergence	1.0×10^{-7}	0.020	0.65
7.0% Momentum Spread	6.10×10^{-8}	0.012	0.40
Temperature to 2°C	7.8×10^{-8}	0.015	0.48
Multiple Scattering	1.5×10^{-8}	0.003	0.09
Chromatic Spread	2.25×10^{-7}	0.045	1.46

TABLE 7: Performance characteristics of the MW-Cherenkov counter at 530 GeV.

4.3.2 The gas system

The gas system for the Cherenkov counter starts at the MW-Gas house in the MW9 enclosure. We used bottles of welding (99.995% pure) He gas. The He bottles were connected at a four station manifold with a Matheson gas regulator and a Scott Speciality moisture trap.

On the upstream end of the counter, and somewhat further downstream, the He gas goes through two more filters before entering the Cherenkov vessel. The first filter was a "shop made" filter consisting of copper brillo pads that were cleaned with freon; this filter is used to prevent oxygen and debris from entering the counter. The second filter is a Scott Specialty gas moisture trap. Before and

after the filters there were pressure gauges to measure any pressure drops.

After the filters, the gas went through a regulator and valve set-up. The valve was used to keep a positive pressure on the regulator. The gas was allowed into the counter by an electric valve. This valve could be operated locally, if the controls were in the "local" mode, or remotely from the experimental counting house, either from a remote control panel or from a personal computer. To prevent overfilling we used a 1.2 atm pressure relief valve located in the middle of the counter.

The Cherenkov counter could be evacuated locally or remotely. The evacuation system used two Guardian "PET 1418" programmable electronic timers that broke the system into three sections. The first opened a solenoid valve, referred to as a "differential pressure module", which allowed the pump and the counter to equalize in pressure, preventing any concussion that could damage the counter's optics when the gate valve was opened.

The second timer opened the gate valve just before the starting of the pump. The gate valve was a VAT VACUUM VALVE, series 10, bought from VAT Inc. in Woburn Mass. It was found that the best setting was for the valve to be fully open about two seconds before the pump started.

The third timer started the pump and the blower at the same time. The pump was an EDWARDS E2M40 with a mechanical booster model EH500A with hydrokinetic drive. The pump had a pumping speed of 400 ft^3 per min at 1 atm.

The pressure of the counter was read from a mechanical pressure gauge and from two pressure transducers. The mechanical pressure gauge was located at the counter and could be read out at the counting house via TV camera and monitor. The pressure transducers were made by OMEGA and were located at the upstream

and downstream end of the counter. Both the transducers were read by a Zenith personal computer using an OMEGA interface card and a terminal box. The gas system is pictured schematically in Fig. 33.

There was also a separate gas system for purging the Cherenkov phototubes with nitrogen, to prevent the phototubes from being contaminated with He (fused silica and natural quartz are permeable to helium). In front of the photomultipliers there were ultrasil (a type of fused silica) windows 3 in. in diameter. The photomultipliers fit in a housing around the windows and sat about 1/2 in. away from them. A gas tight seal was made around the phototubes and the housing to permit a constant nitrogen purge around the phototubes.

The nitrogen gas for the purging comes from a nitrogen dewar outside the experimental building. A line was tapped into the dewar for gas only and the nitrogen was brought to the gas house where there was a check valve and a regulator. After the regulator, the nitrogen was piped to the counter, where it went through a manifold. This manifold distributed the gas to each of the phototubes for purge. A set of 12 oil bubblers on the manifold gave visual evidence that there was a gas purge across the front face of each phototube.

4.3.3 The Optics

The counter optics consisted of a spherical mirror, the conical reflector, the light guides, the phototube windows, and the phototubes.

a) *The spherical mirror.* The mirror that is used to focus the Cherenkov light

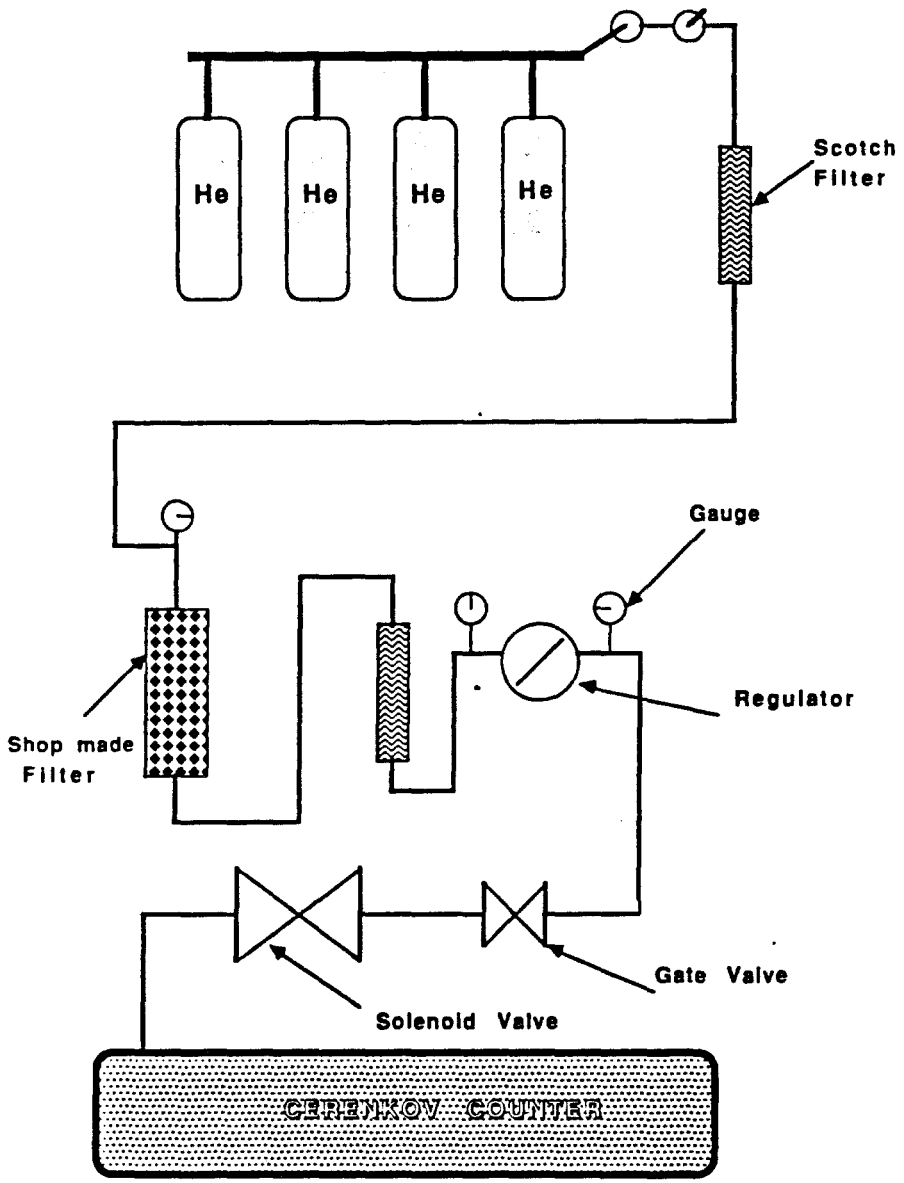

Figure 33: The MW Cherenkov counter gas system

is a front aluminized spherical mirror with a focal length of 1275.5 in. (32.4 m). The mirror (made by Unertl Co. of Philadelphia PA.) has a useful diameter of 18.5 in., and is mounted on a aluminum base that is capable of tilting in the x and y plane for fine adjustments. The mirror was coated with Al plus a $\lambda/2$ thick layer of MgF_2 to protect the Al from oxidizing and enhance the ultraviolet reflectance.

b) *The conical reflector.* The conical reflector consists of a cylinder (45.72 cm long), the front part of which, 16.5 cm, is inclined with a slope of 34.6 mrad. The inner diameter of the cylinder is 29.72 cm (Fig. 34). On top of the cylinder fits a cylindrical cap that has a length of 15.3 cm and a slope of 38.31 mrad, so that there is a gap of 5mm between the cap and the front surface of the cylinder (Fig. 35). Both inclined surfaces are aluminized to reflect the light while the rest surface of the cylinder and the inner surface of the cylindrical cap are painted black to absorb light. In the back of the cylinder fits a ring with openings for the light guides. The counter is tuned by varying the He pressure so that the Cherenkov light of selected or (tagged) particles goes through the 5mm aperture and lands on the inside ring of phototubes (coincidence channel).

The Cherenkov light from particles with masses different from those of the detected particle will hit one of the inclined reflecting surfaces and will end up in the anticoincidence channel of phototubes, or will directly land in the anti-ring of tubes. Of course, if the mass of a particle is much smaller than the mass of the tagged particle, the Cherenkov light of that particle will end up inside the cylinder of the conical reflector and will be lost.

The optical design of the Cherenkov counter was done with the objective of separating πs from ps at the highest possible secondary momentum which was

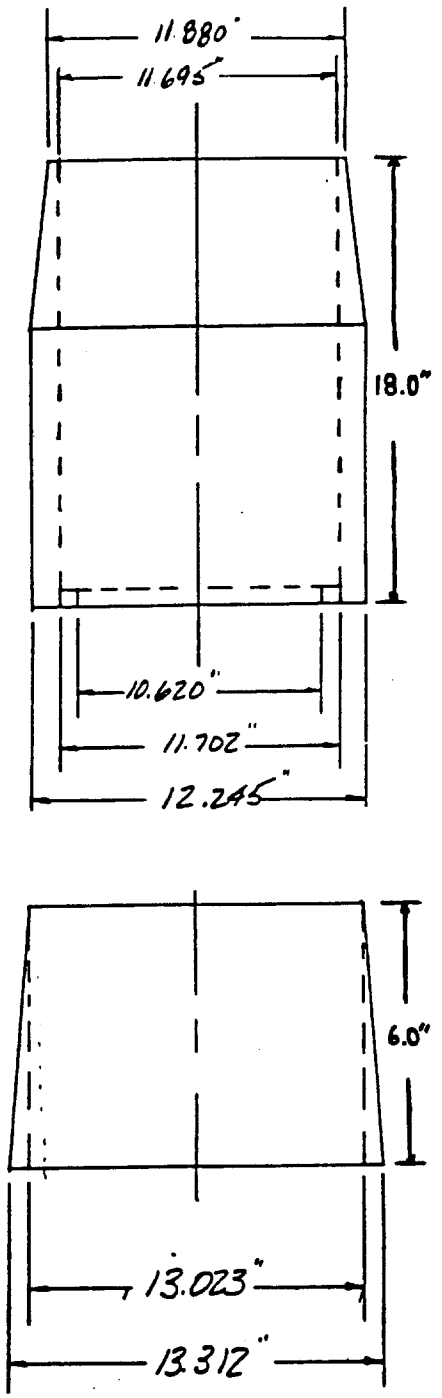

Figure 34: Parts of the Conical Reflector. (top): Main cylinder. (bottom): Cylindrical Cap.

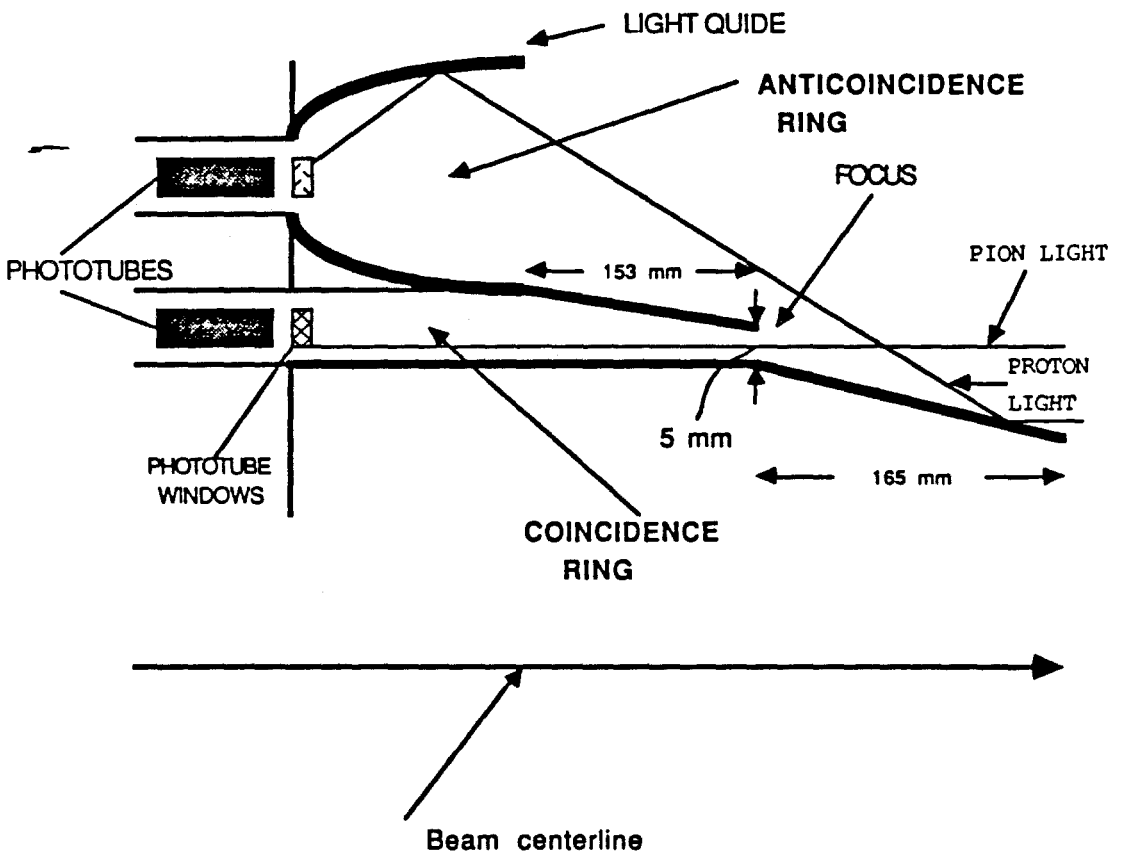

Figure 35: A partial cross section of the conical reflector assembly.

considered to be 700 GeV. For a 700 GeV beam $\Delta\beta_{\pi,p} = 8.778 \times 10^{-7}$ and $\Delta\beta_{\pi,K} = 2.283 \times 10^{-7}$. Thus, for this counter $\Delta\theta_{\pi,p} = \frac{\Delta\beta_{\pi,p}}{tan\theta} = 0.176$ mrad, $\Delta\theta_{\pi,K} = 0.0457$ mrad. Assuming that the tagged particles are pions, the distances, ΔR, between the focal rings are:

$$\Delta R_{\pi,p} = 6.375'' - (1275.5'')\tan(4.822 \text{ mrad}) = 0.224'' = 5.703 \text{ mm} \tag{4.28}$$

and

$$\Delta R_{\pi,K} = 6.375'' - (1275.5'')\tan(4.953 \text{ mrad}) = 0.057'' = 1.459 \text{ mm} \tag{4.29}$$

These separations of two particles have to be modified by the effects of divergence of the beam. The beam divergence is, $\Delta\theta_{bd} = \pm 0.025$ mrad. Thus the spread due to the beam divergence is given by:

$$\Delta R_{bd} = \pm f \tan(\theta_{bd}) = \pm 0.0318'' = \pm 0.81 \text{ mm} \tag{4.30}$$

Now we have to take into account the light spread due to the change in the index of refraction with the wavelength (chromatic spread). The chromatic spread was designed to be confined to the region 0.8 mm from the inner and outer radii of the coincidence ring aperture, to compensate for the smearing due to the beam divergence. In other words the particle's light was restricted to a ring with a width of $(5.0 - 1.6)$ mm=3.4 mm=0.1338 in. centered in the center of the coincidence channel. To restrict the pion or proton light to the desired ring (3.4 mm width), special windows were introduced to block light with wavelengths which corresponded to

undesirable angles. To determine the transmission properties needed for the windows, one wants to position the longest wavelength to which the photocathode is sensitive to (~600 nm), at the smallest Cherenkov angle θ_{min}. Assuming that the tagged particles are pions:

$$\theta^{\pi}_{min} = \frac{\left(6.375'' - \frac{0.1338''}{2}\right)}{1275.5''} = 4.9455 \text{ mrad} \tag{4.31}$$

so:

$$\eta^{\pi}_{min} = \frac{1}{\beta_{\pi} \cos \theta^{\pi}_{min}} = 1.000012250 \tag{4.32}$$

In order to avoid overlapping between pion and proton light, we must have the proton light with the smallest acceptable wavelength lying 0.8 mm away from the 5 mm aperture, i.e:

$$\theta^{p}_{max} = \frac{\left(6.375'' - \frac{0.1968''}{2} - 0.0315''\right)}{1275.5''} = 4.896 \text{ mrad} \tag{4.33}$$

so:

$$\eta^{p}_{max} = \frac{1}{\beta_{p} \cos \theta^{p}_{max}} = 1.000012884 \tag{4.34}$$

We must also confine the pion light with the smallest acceptable wavelength inside the 0.1338″ diameter aperture, i.e:

$$\theta^{\pi}_{max} = \frac{\left(6.375'' + \frac{0.1338''}{2}\right)}{1275.5''} = 5.0505 \text{ mrad} \tag{4.35}$$

so:

$$\eta^{\pi}_{max} = \frac{1}{\beta_{\pi} \cos \theta^{\pi}_{max}} = 1.000012775 \tag{4.36}$$

Now taking into account the variation of the index of refraction with the wavelength at 700 GeV (Table 8), we conclude that we must limit the Cherenkov light to be between 220-600 nm. A window can be used to prevent the light below 220 nm from hitting the phototubes. Nothing needs to be done about the light above 600 nm because there are very few photons. For comparison we also list the similar table for 530 GeV (table 9).

From this table we can see that π and p are completely separated at all the wavelengths that the photocathode is sensitive to. In this case the windows reduce the chromatic dispersion of the Cherenkov light and help separate the kaon and pion light. The Cherenkov was used at -530 GeV to tag K^-. In this case we adjusted the Cherenkov pressure so that to position the kaon light with the smallest acceptable wavelength (300 nm as will be explained later) just inside the 0.1338″ diameter aperture in the coincidence ring i.e at 6.442″ (Table 10). The pion light will end up in the coincidence ring and will overlap with the kaon light for wavelengths larger than 390 nm.

c) *The light guides.* The light guides are used to guide the light through internal reflections to the phototubes. They are made of plastic cold coated internally with

CERENKOV ANGLES WERE CALCULATED AT A MOMENTUM OF 700. GEV/C

WAVELENGTH ANGSTROMS	INDEX AT 5.54 PSI (N-1)*E-5	THETA PIONS IN MR	HEIGHT* AT DETECTORS IN IN.	THETA KAONS IN MR	HEIGHT AT DETECTORS IN IN.	THETA PROTONS IN MR	HEIGHT AT DETECTORS IN IN.
1500.	0.1354570	5.2	6.634	5.2	6.577	5.0	6.415
1600.	0.1336056	5.2	6.588	5.1	6.531	5.0	6.368
1700.	0.1321137	5.1	6.552	5.1	6.494	5.0	6.330
1800.	0.1308925	5.1	6.521	5.1	6.463	4.9	6.298
1900.	0.1298789	5.1	6.496	5.0	6.438	4.9	6.272
2000.	0.1290278	5.1	6.474	5.0	6.416	4.9	6.250
2100.	0.1283057	5.1	6.456	5.0	6.398	4.9	6.231
2200.	0.1276873	5.0	6.441	5.0	6.382	4.9	6.215
2300.	0.1271535	5.0	6.427	5.0	6.369	4.9	6.201
2400.	0.1266893	5.0	6.415	5.0	6.357	4.9	6.189
2500.	0.1262829	5.0	6.405	5.0	6.346	4.8	6.178
2600.	0.1259251	5.0	6.396	5.0	6.337	4.8	6.169
2700.	0.1256083	5.0	6.388	5.0	6.329	4.8	6.160
2800.	0.1253265	5.0	6.381	5.0	6.322	4.8	6.153
2900.	0.1250745	5.0	6.374	5.0	6.315	4.8	6.146
3000.	0.1248484	5.0	6.369	4.9	6.310	4.8	6.140
3100.	0.1246446	5.0	6.363	4.9	6.304	4.8	6.135
3200.	0.1244603	5.0	6.359	4.9	6.299	4.8	6.130
3300.	0.1242930	5.0	6.354	4.9	6.295	4.8	6.125
3400.	0.1241408	5.0	6.350	4.9	6.291	4.8	6.121
3500.	0.1240018	5.0	6.347	4.9	6.288	4.8	6.118
3600.	0.1238745	5.0	6.344	4.9	6.284	4.8	6.114
3700.	0.1237577	5.0	6.341	4.9	6.281	4.8	6.111
3800.	0.1236503	5.0	6.338	4.9	6.279	4.8	6.108
3900.	0.1235512	5.0	6.335	4.9	6.276	4.8	6.106
4000.	0.1234596	5.0	6.333	4.9	6.274	4.8	6.103
4100.	0.1233747	5.0	6.331	4.9	6.271	4.8	6.101
4200.	0.1232960	5.0	6.329	4.9	6.269	4.8	6.099
4300.	0.1232228	5.0	6.327	4.9	6.267	4.8	6.097
4400.	0.1231546	5.0	6.325	4.9	6.266	4.8	6.095
4500.	0.1230910	5.0	6.323	4.9	6.264	4.8	6.093
4600.	0.1230316	5.0	6.322	4.9	6.262	4.8	6.092
4700.	0.1229760	5.0	6.321	4.9	6.261	4.8	6.090
4800.	0.1229239	5.0	6.319	4.9	6.260	4.8	6.089
4900.	0.1228750	5.0	6.318	4.9	6.258	4.8	6.088
5000.	0.1228290	5.0	6.317	4.9	6.257	4.8	6.086
5100.	0.1227858	5.0	6.316	4.9	6.256	4.8	6.085
5200.	0.1227450	5.0	6.315	4.9	6.255	4.8	6.084
5300.	0.1227066	4.9	6.314	4.9	6.254	4.8	6.083
5400.	0.1226703	4.9	6.313	4.9	6.253	4.8	6.082
5500.	0.1226360	4.9	6.312	4.9	6.252	4.8	6.081
5600.	0.1226035	4.9	6.311	4.9	6.251	4.8	6.080
5700.	0.1225728	4.9	6.310	4.9	6.251	4.8	6.080
5800.	0.1225436	4.9	6.309	4.9	6.250	4.8	6.079
5900.	0.1225160	4.9	6.309	4.9	6.249	4.8	6.078
6000.	0.1224897	4.9	6.308	4.9	6.248	4.8	6.077

Table 8: Variation of the index of refraction of He and the Cherenkov angle of different 700 GeV particles with the wavelength. The index of refraction of He was calculated at a pressure of 5.54 psi and at 20°. *(Height at the detectors means radius at the phototubes).

CERENKOV ANGLES WERE CALCULATED AT A MOMENTUM OF 530. GEV/C

WAVELENGTH ANGSTROMS	INDEX AT 5.55 PSI (N-1)*E-5	THETA PIONS IN MR	HEIGHT AT DETECTORS IN IN.	THETA KAONS IN MR	HEIGHT AT DETECTORS IN IN.	THETA PROTONS IN MR	HEIGHT AT DETECTORS IN IN.
1500.	0.1356216	5.2	6.634	5.1	6.535	4.9	6.248
1600.	0.1337679	5.2	6.589	5.1	6.489	4.9	6.199
1700.	0.1322743	5.1	6.552	5.1	6.451	4.8	6.160
1800.	0.1310516	5.1	6.521	5.0	6.420	4.8	6.127
1900.	0.1300368	5.1	6.496	5.0	6.395	4.8	6.100
2000.	0.1291846	5.1	6.475	5.0	6.373	4.8	6.078
2100.	0.1284616	5.1	6.456	5.0	6.355	4.7	6.058
2200.	0.1278425	5.0	6.441	5.0	6.339	4.7	6.042
2300.	0.1273080	5.0	6.427	5.0	6.325	4.7	6.027
2400.	0.1268432	5.0	6.416	4.9	6.313	4.7	6.015
2500.	0.1264364	5.0	6.405	4.9	6.302	4.7	6.004
2600.	0.1260782	5.0	6.396	4.9	6.293	4.7	5.994
2700.	0.1257610	5.0	6.388	4.9	6.285	4.7	5.985
2800.	0.1254788	5.0	6.381	4.9	6.278	4.7	5.978
2900.	0.1252265	5.0	6.374	4.9	6.271	4.7	5.971
3000.	0.1250001	5.0	6.369	4.9	6.265	4.7	5.965
3100.	0.1247961	5.0	6.363	4.9	6.260	4.7	5.959
3200.	0.1246116	5.0	6.359	4.9	6.255	4.7	5.954
3300.	0.1244441	5.0	6.354	4.9	6.251	4.7	5.949
3400.	0.1242917	5.0	6.350	4.9	6.247	4.7	5.945
3500.	0.1241525	5.0	6.347	4.9	6.243	4.7	5.941
3600.	0.1240251	5.0	6.344	4.9	6.240	4.7	5.938
3700.	0.1239082	5.0	6.341	4.9	6.237	4.7	5.935
3800.	0.1238006	5.0	6.338	4.9	6.234	4.7	5.932
3900.	0.1237013	5.0	6.335	4.9	6.231	4.6	5.929
4000.	0.1236096	5.0	6.333	4.9	6.229	4.6	5.927
4100.	0.1235247	5.0	6.331	4.9	6.227	4.6	5.924
4200.	0.1234458	5.0	6.329	4.9	6.225	4.6	5.922
4300.	0.1233726	5.0	6.327	4.9	6.223	4.6	5.920
4400.	0.1233043	5.0	6.325	4.9	6.221	4.6	5.918
4500.	0.1232406	5.0	6.324	4.9	6.219	4.6	5.916
4600.	0.1231811	5.0	6.322	4.9	6.218	4.6	5.915
4700.	0.1231255	5.0	6.321	4.9	6.216	4.6	5.913
4800.	0.1230733	5.0	6.319	4.9	6.215	4.6	5.912
4900.	0.1230243	5.0	6.318	4.9	6.214	4.6	5.910
5000.	0.1229783	5.0	6.317	4.9	6.213	4.6	5.909
5100.	0.1229350	5.0	6.316	4.9	6.211	4.6	5.908
5200.	0.1228942	5.0	6.315	4.9	6.210	4.6	5.907
5300.	0.1228557	4.9	6.314	4.9	6.209	4.6	5.906
5400.	0.1228194	4.9	6.313	4.9	6.208	4.6	5.905
5500.	0.1227851	4.9	6.312	4.9	6.207	4.6	5.904
5600.	0.1227526	4.9	6.311	4.9	6.207	4.6	5.903
5700.	0.1227218	4.9	6.310	4.9	6.206	4.6	5.902
5800.	0.1226926	4.9	6.309	4.9	6.205	4.6	5.901
5900.	0.1226649	4.9	6.309	4.9	6.204	4.6	5.901
6000.	0.1226386	4.9	6.308	4.9	6.204	4.6	5.900

Table 9: Variation of the index of refraction of He and the Cherenkov angle of different 530 GeV particles with the wavelength. The index of refraction of He was calculated at a pressure of 5.55 psi and at 20°.

CERENKOV ANGLES WERE CALCULATED AT A MOMENTUM OF 530. GEV/C

WAVELENGTH ANGSTROMS	INDEX AT 5.86 PSI (N-1)*E-5	THETA PIONS IN MR	HEIGHT AT DETECTORS IN IN.	THETA KAONS IN MR	HEIGHT AT DETECTORS IN IN.	THETA PROTONS IN MR	HEIGHT AT DETECTORS IN IN.
1500.	0.1431098	5.3	6.816	5.3	6.719	5.0	6.440
1600.	0.1411538	5.3	6.769	5.2	6.672	5.0	6.390
1700.	0.1395777	5.3	6.731	5.2	6.633	5.0	6.350
1800.	0.1382874	5.3	6.699	5.2	6.601	5.0	6.317
1900.	0.1372166	5.2	6.673	5.2	6.575	4.9	6.289
2000.	0.1363174	5.2	6.651	5.1	6.553	4.9	6.266
2100.	0.1355545	5.2	6.633	5.1	6.534	4.9	6.246
2200.	0.1349012	5.2	6.617	5.1	6.517	4.9	6.229
2300.	0.1343372	5.2	6.603	5.1	6.503	4.9	6.214
2400.	0.1338468	5.2	6.591	5.1	6.491	4.9	6.201
2500.	0.1334175	5.2	6.580	5.1	6.480	4.9	6.190
2600.	0.1330395	5.2	6.571	5.1	6.471	4.8	6.180
2700.	0.1327048	5.1	6.562	5.1	6.462	4.8	6.171
2800.	0.1324070	5.1	6.555	5.1	6.455	4.8	6.163
2900.	0.1321408	5.1	6.548	5.1	6.448	4.8	6.156
3000.	0.1319019	5.1	6.543	5.1	6.442	4.8	6.150
3100.	0.1316866	5.1	6.537	5.0	6.437	4.8	6.144
3200.	0.1314919	5.1	6.532	5.0	6.432	4.8	6.139
3300.	0.1313152	5.1	6.528	5.0	6.427	4.8	6.134
3400.	0.1311543	5.1	6.524	5.0	6.423	4.8	6.130
3500.	0.1310075	5.1	6.520	5.0	6.419	4.8	6.126
3600.	0.1308730	5.1	6.517	5.0	6.416	4.8	6.123
3700.	0.1307496	5.1	6.514	5.0	6.413	4.8	6.119
3800.	0.1306361	5.1	6.511	5.0	6.410	4.8	6.116
3900.	0.1305314	5.1	6.508	5.0	6.407	4.8	6.114
4000.	0.1304346	5.1	6.506	5.0	6.405	4.8	6.111
4100.	0.1303450	5.1	6.504	5.0	6.403	4.8	6.109
4200.	0.1302618	5.1	6.502	5.0	6.400	4.8	6.106
4300.	0.1301844	5.1	6.500	5.0	6.398	4.8	6.104
4400.	0.1301124	5.1	6.498	5.0	6.397	4.8	6.102
4500.	0.1300452	5.1	6.496	5.0	6.395	4.8	6.101
4600.	0.1299825	5.1	6.495	5.0	6.393	4.8	6.099
4700.	0.1299237	5.1	6.493	5.0	6.392	4.8	6.097
4800.	0.1298687	5.1	6.492	5.0	6.390	4.8	6.096
4900.	0.1298170	5.1	6.491	5.0	6.389	4.8	6.095
5000.	0.1297684	5.1	6.489	5.0	6.388	4.8	6.093
5100.	0.1297227	5.1	6.488	5.0	6.387	4.8	6.092
5200.	0.1296797	5.1	6.487	5.0	6.386	4.8	6.091
5300.	0.1296391	5.1	6.486	5.0	6.385	4.8	6.090
5400.	0.1296008	5.1	6.485	5.0	6.384	4.8	6.089
5500.	0.1295645	5.1	6.484	5.0	6.383	4.8	6.088
5600.	0.1295302	5.1	6.483	5.0	6.382	4.8	6.087
5700.	0.1294977	5.1	6.482	5.0	6.381	4.8	6.086
5800.	0.1294669	5.1	6.482	5.0	6.380	4.8	6.085
5900.	0.1294377	5.1	6.481	5.0	6.379	4.8	6.084
6000.	0.1294099	5.1	6.480	5.0	6.379	4.8	6.084

Table 10: Variation of the index of refraction of He and the Cherenkov angle of different 530 GeV particles with the wavelength. The index of refraction of He was calculated at a pressure of 5.86 psi and at 20°.

Al and they have a conical shape with a round top.

d) *The phototube windows.* The windows in front of the phototubes have a diameter of 3 in. (7.62 cm) and the ones in front of the inner (coincidence) ring of phototubes have a thickness of 1/2 in. (1.27 cm) while the ones in front of the outer (anti-coincidence) ring of phototubes have a thickness of 3/4 in. (1.91 cm). All the windows in the coincidence channel are made of Ultrasil and they effectively transmit light down to 225 nm (Fig. 36). In the anticoincidence or outer ring, the windows were made of an unknown type of UV glass whose transmission dropped severely below 300 nm.

e) *The phototubes.* HAMAMATSU R1332X phototubes with quartz windows were used, which are capable of detecting light down to 160 nm. The phototubes have a 2 in. (51 mm) diameter and use a bialkali photocathode for high quantum efficiency (25% at 385 nm). The quantum efficiency of the phototubes is plotted versus wavelength in Fig. 37.

4.3.4 Logic and Electronics

The signals from all the phototubes and the two scintillation counters upstream and downstream the Cherenkov counter are transported using coaxial cables to the upstream latch house where they go through the electronics.

The Cherenkov trigger logic is depicted schematically in Fig. 38. The phototube signals are first amplified by a programmable amplifier, set to a gain of ten, and then go through a discriminator (along with the signals of the two scintillators).

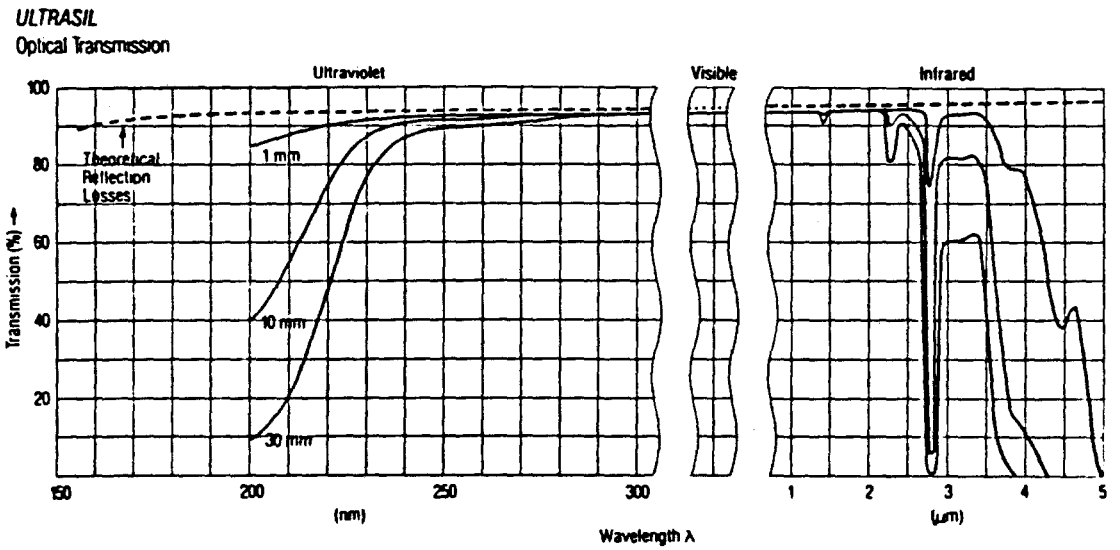

Figure 36: Optical transmission of the Ultrasil windows.

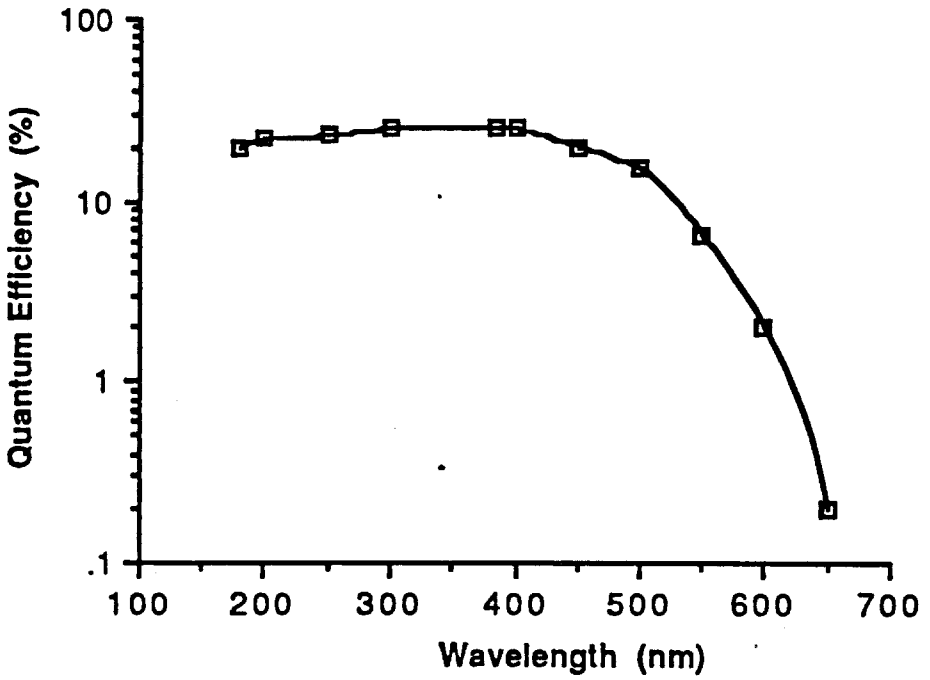

Figure 37: Quantum efficiency versus wavelength, for the HAMAMATSU R1332X phototubes.

After the discriminator, the signals go to a programmable logic delay/fan-out unit for timing. This unit has three output streams.

The first stream of output signals goes to a series of 4508 LeCroy programmable logic units used to do the final Cherenkov coincidence logic. The 6 Cherenkov coincidence logic combinations outputs along with the two signals from the scintillation counters, go through an ECL/NIM converter, then to a prescaler and finally to a scaler from where they are recorded. These signals were used to obtain the Cherenkov pressure curves. The Cherenkov coincidence logic combinations used were:

$DN_1\overline{VN_2}$: N_1 or more phototubes in the coincidence channel firing with less than N_2 phototubes firing in the anti-coincidence channel ($1 \leq N_{1,2} \leq 6$). In this notation D stands for the coincidence channel and V for the anti-coincidence (veto channel).

$D23\overline{V2}$: $[(1.AND.3.AND.5).OR.(2.AND.4.AND.6)]$ .AND.$\overline{V2}$ where the numbers correspond to photomultipliers in the coincidence channel if one starts counting them from the top and goes clockwise looking downstream along the direction of the beam.

A second and the third streams of signals go to latches designed by our University of Minnesota collaborators. For each event the content of the Cherenkov latches were written to a tape along with the other event information. Out of the 16 data bits avaliable in the Cherenkov latches, 6 were used to store the information from the phototubes in the coincidence channel, 6 to store the information from the phototubes in the anti-channel and 2 to store the information from the two Cherenkov scintillators counters.

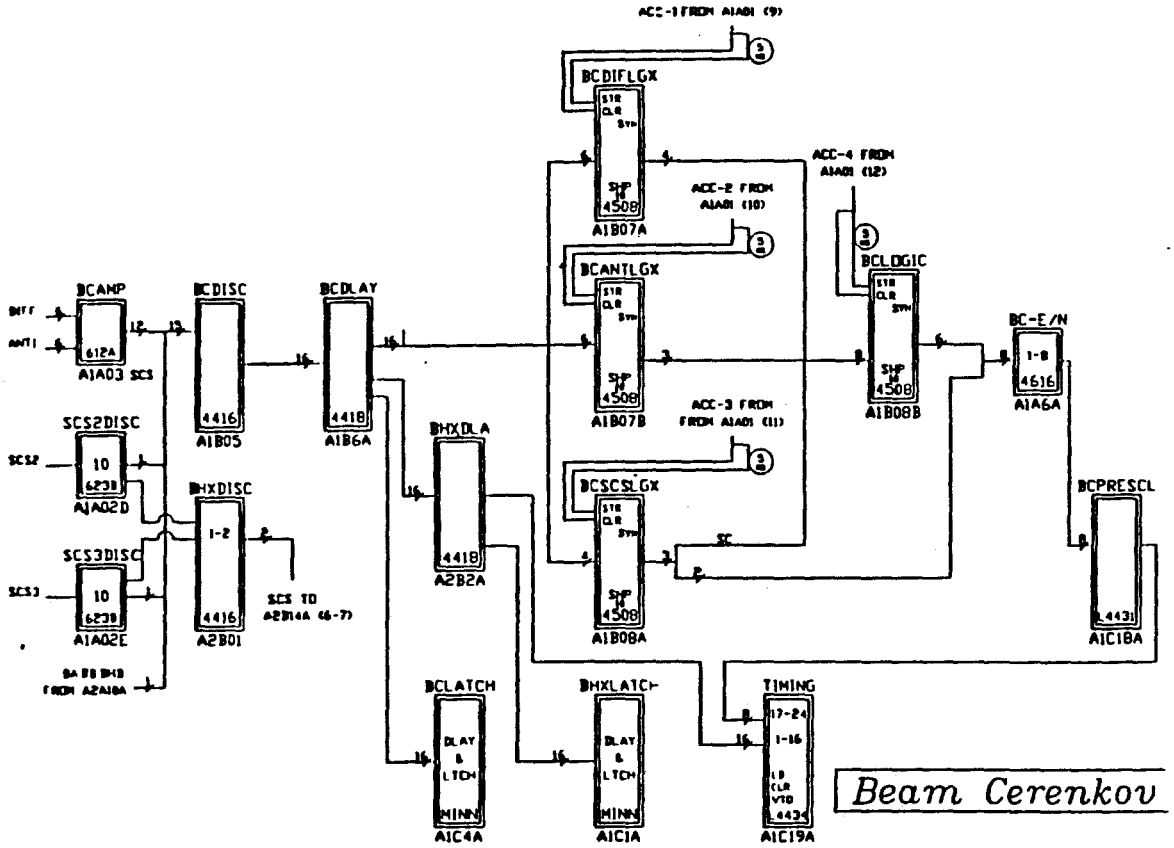

Figure 38: MW Cherenkov trigger logic.

All the high voltage signals were controlled by a Le Croy 1440 programmable multichannel high voltage supply.

4.4. Monte Carlo Simulation and Counter Performance

4.4.1 Monte Carlo Simulation and Pressure Curves

The MW-Cherenkov counter was used extensively during the E-706 shakedown run to tag particles at different momenta in the range 50-530 GeV and at + and − polarities. In Fig. 39, 40, 41 and 42 a set of pressure curves taken at several different momenta and polarities are shown. As we can see from the pressure curves, there is a separation (although not complete) between π and K even at 530 GeV.

A Monte Carlo program was developed to simulate the counter's performance in order to help us estimate the exact kaon and pion fraction at 530 GeV, and the various contaminations. The Monte Carlo program generates particles of specified masses taking into account the momentum dispersion of the beam. Each particle emits Cherenkov radiation at random points along its path through the counter. The photons are generated uniformly within a wavelength range accepted by the counter's optics. For each wavelength the refractive index of He was calculated using the Dalgano and Kingston expression (Eq. 4.17), and then was converted to

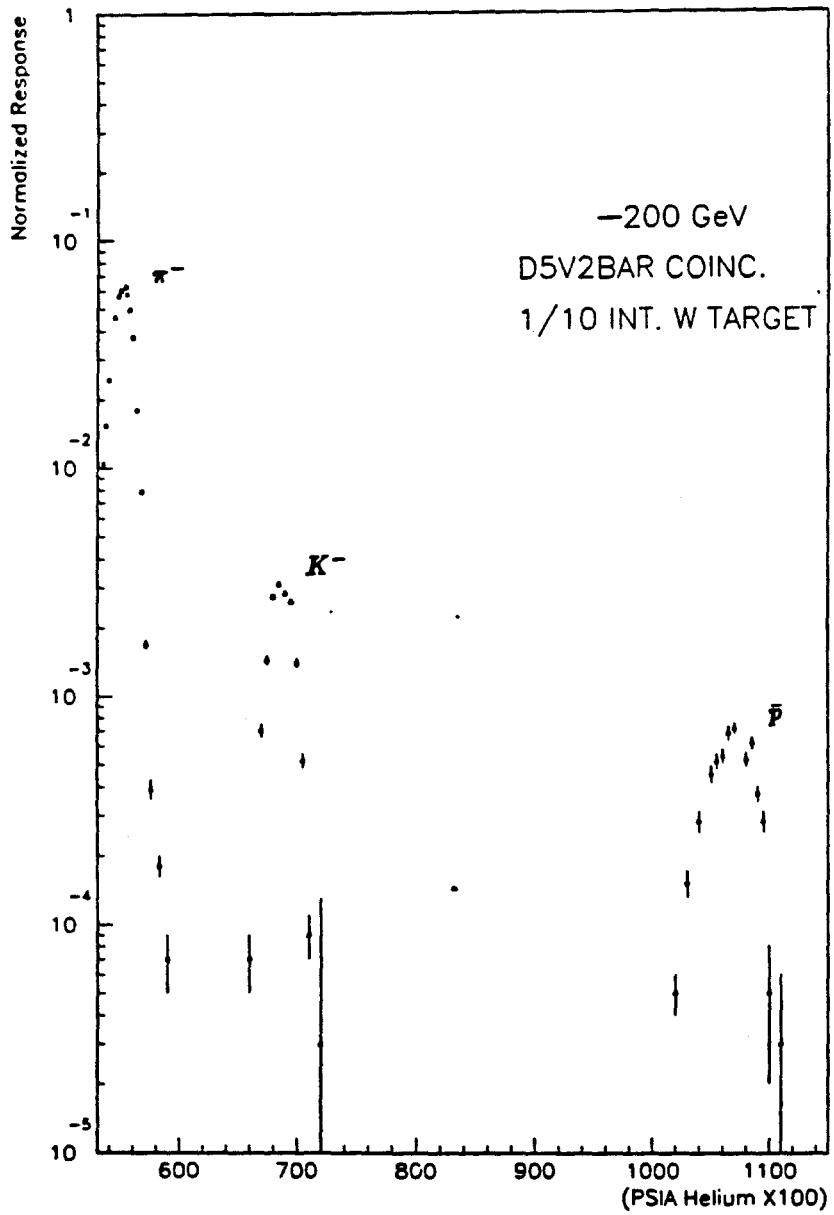

Figure 39: Pressure Curve at -200 GeV.

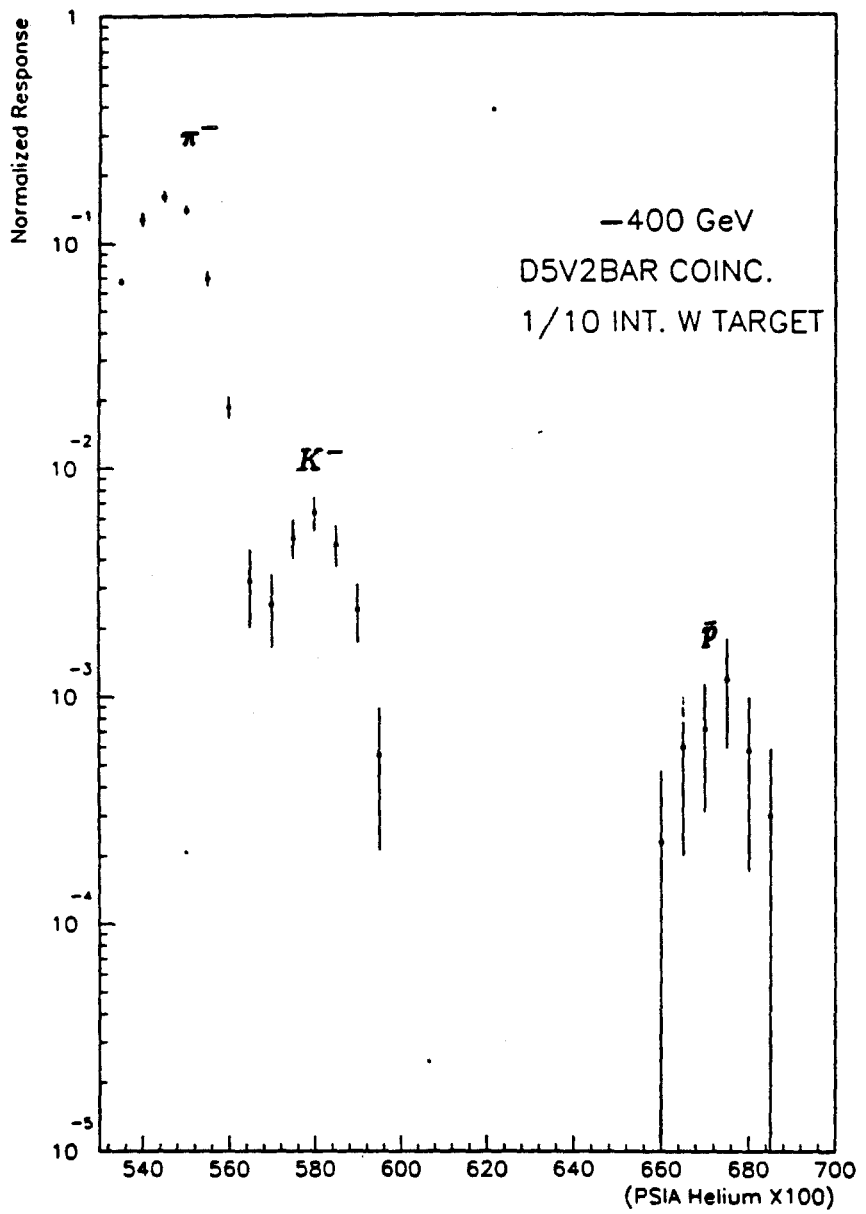

Figure 40: Pressure Curve at -400 GeV.

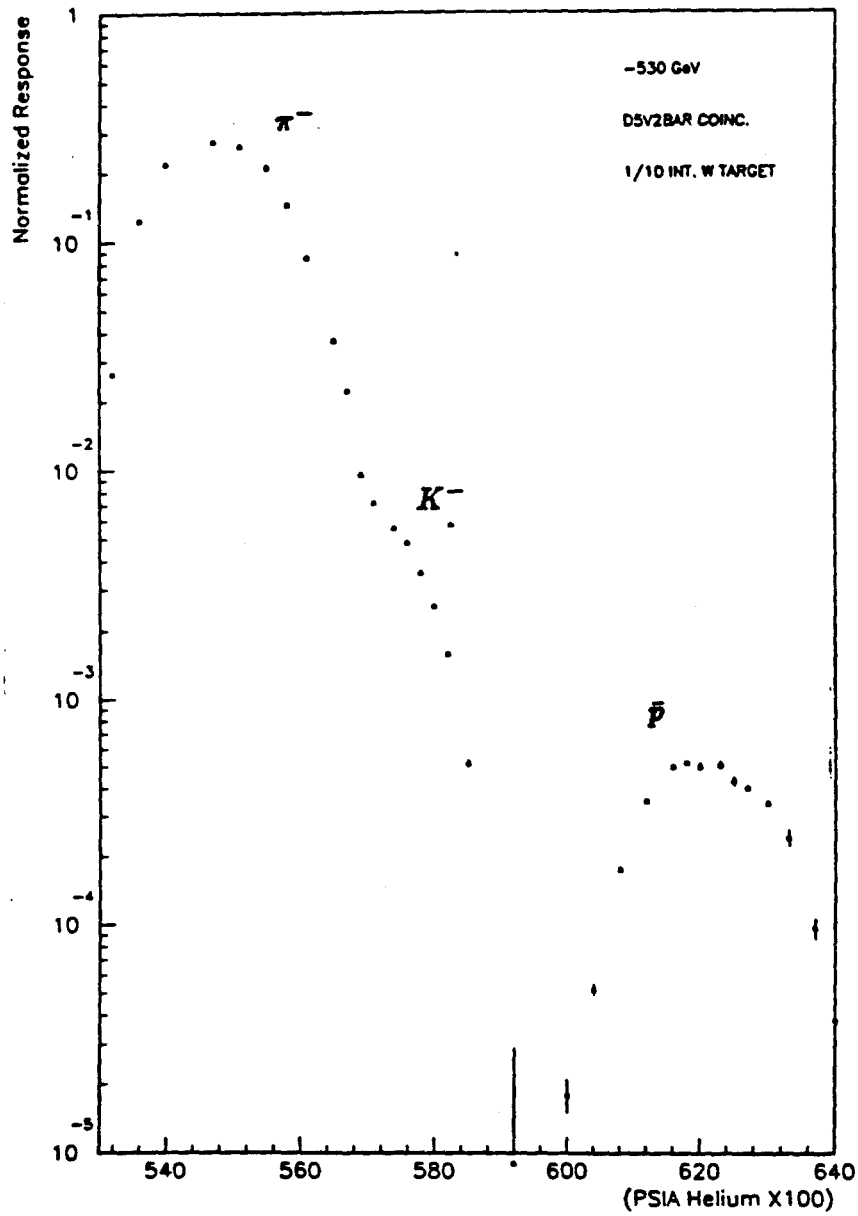

Figure 41: Pressure Curve at -530 GeV.

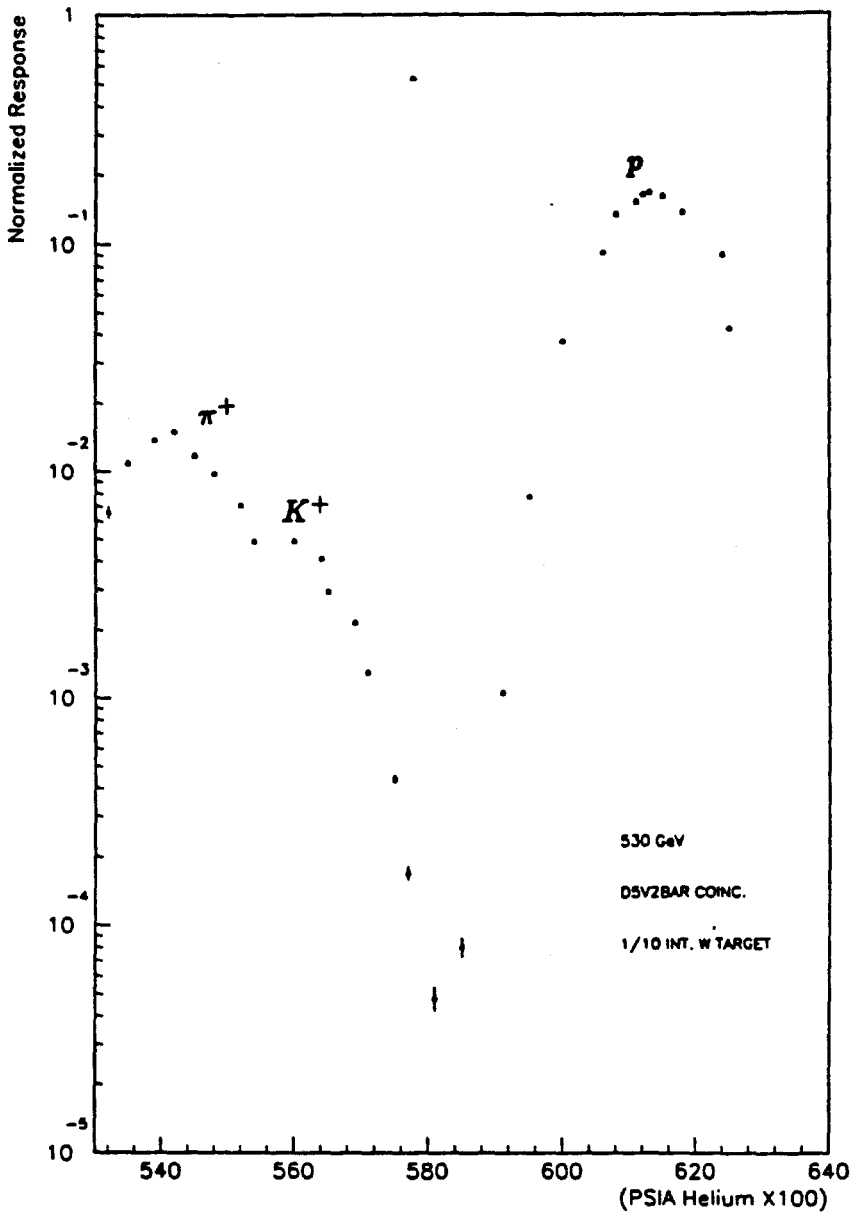

Figure 42: Pressure Curve at 530 GeV.

the pressure and temperature of the counter using the Lorentz-Lorenz law and the law of gases. The emission of photons was considered to take place at a cone polar angle $\theta = \cos^{-1}(1/\eta\beta)$ and to be uniform in ϕ. Finally each photon was weighted with the probability $dN/d\lambda = (2\pi\alpha/\lambda^2)L\sin^2\theta$, where $dN/d\lambda$ is the number of photons per wavelength, L is the counter's length, and α is the fine structure constant. The beam divergence of the beam was added as Gaussian distribution in the angle θ.

The emitted photons are reflected from the mirror and are followed through the counter. The ones that make it to the phototubes are transformed into photoelectrons using the quantum efficiency curves. Using the number of photoelectrons the various electronic efficiencies are calculated and plotted as a function of pressure.

The Monte Carlo pressure curves were also used to qualitatively show the effect of the chromatic dispersion, the beam divergence and the beam momentum bite on the counter's resolution. Figures 43, 44 and 45 show the effect that each of the quantities mentioned above had on the Cherenkov pressure curve at -530 GeV. The particles fractions used in these examples were determined from the data. Figures 46, 47 show the Monte Carlo pressure curves superimposed on the actual pressure curves for the ± 530 GeV and the $D5\overline{V2}$ coincidence level (for the 3/4 interaction length Al target). The agreement between the calculations and the data is good.

Although the optical properties of the mirror, the phototube windows and the phototubes are well known, there was some uncertainty concerning the optical properties of the various light guides. After studying the efficiencies for the six-fold coincidence ($D6$) achieved by the counter ($\sim$ 8.0%), we concluded that we

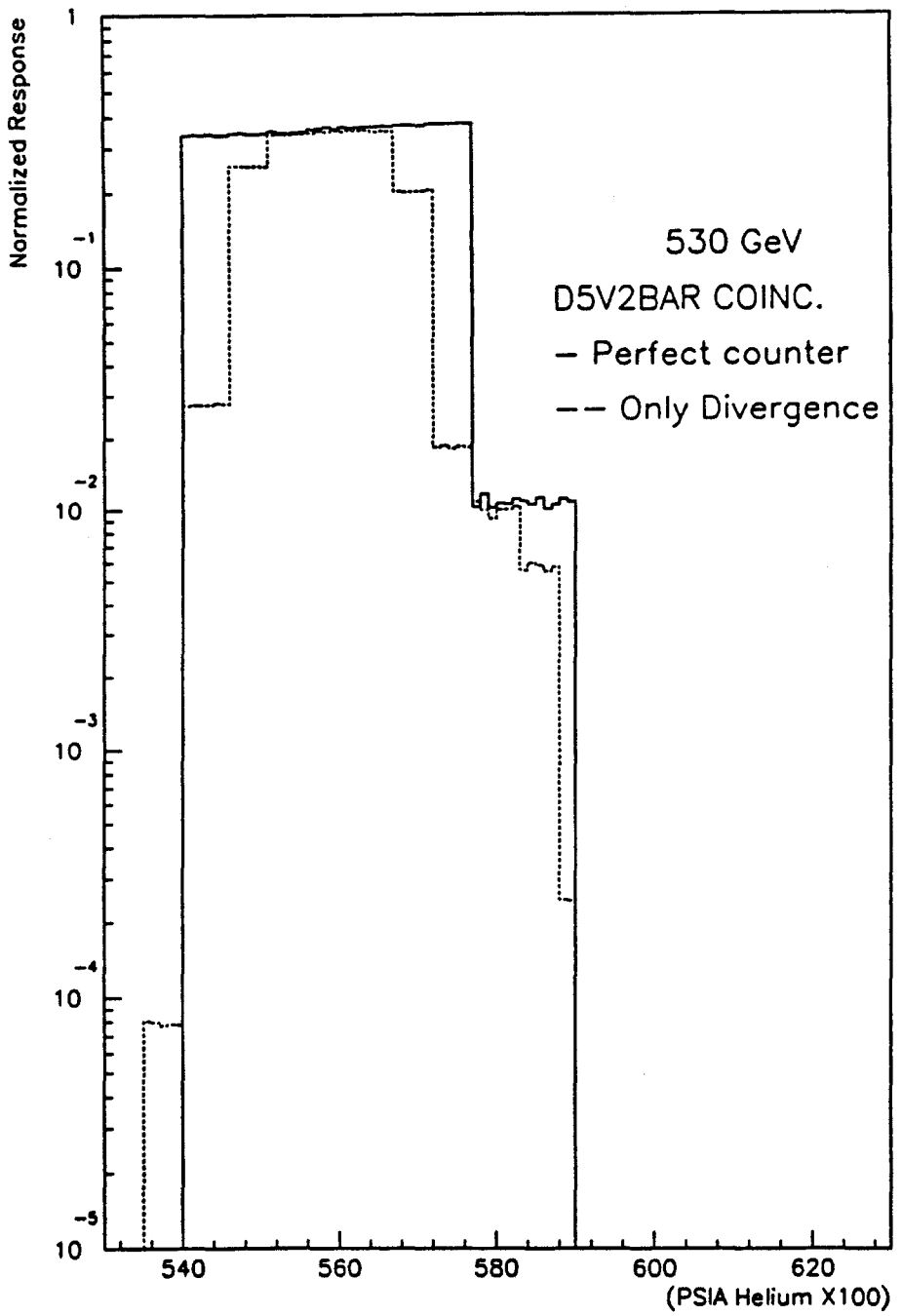

Figure 43: Effect of the beam divergence on the resolution of the Cherenkov counter at -530 GeV. Solid line: Perfect counter. Dashed line: Counter with only beam divergence (0.025 mrad).

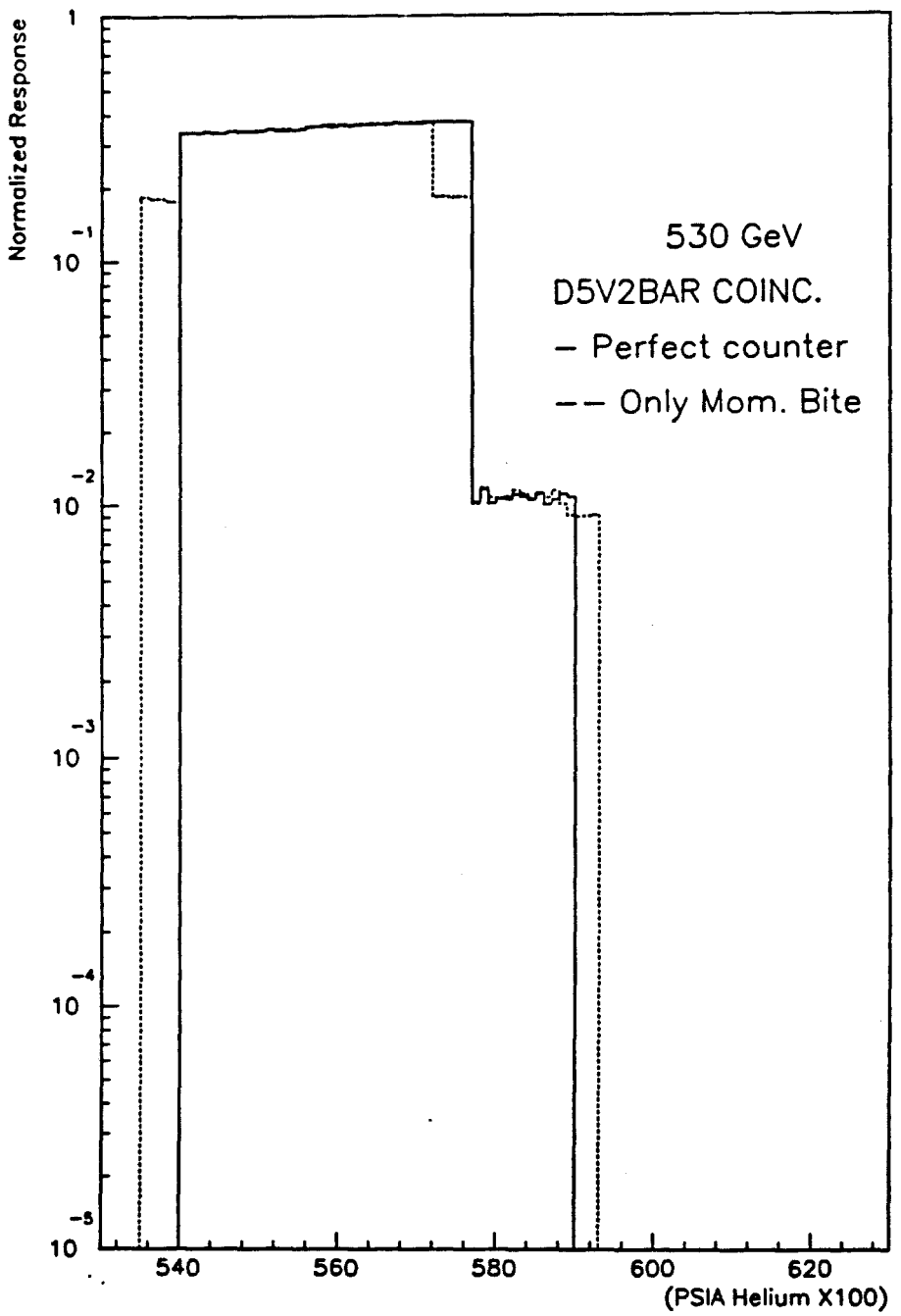

Figure 44: Effect of the beam momentum bite on the resolution of the Cherenkov counter. Solid line: Perfect counter Dashed line: Counter with 10% (FWHM) momentum bite.

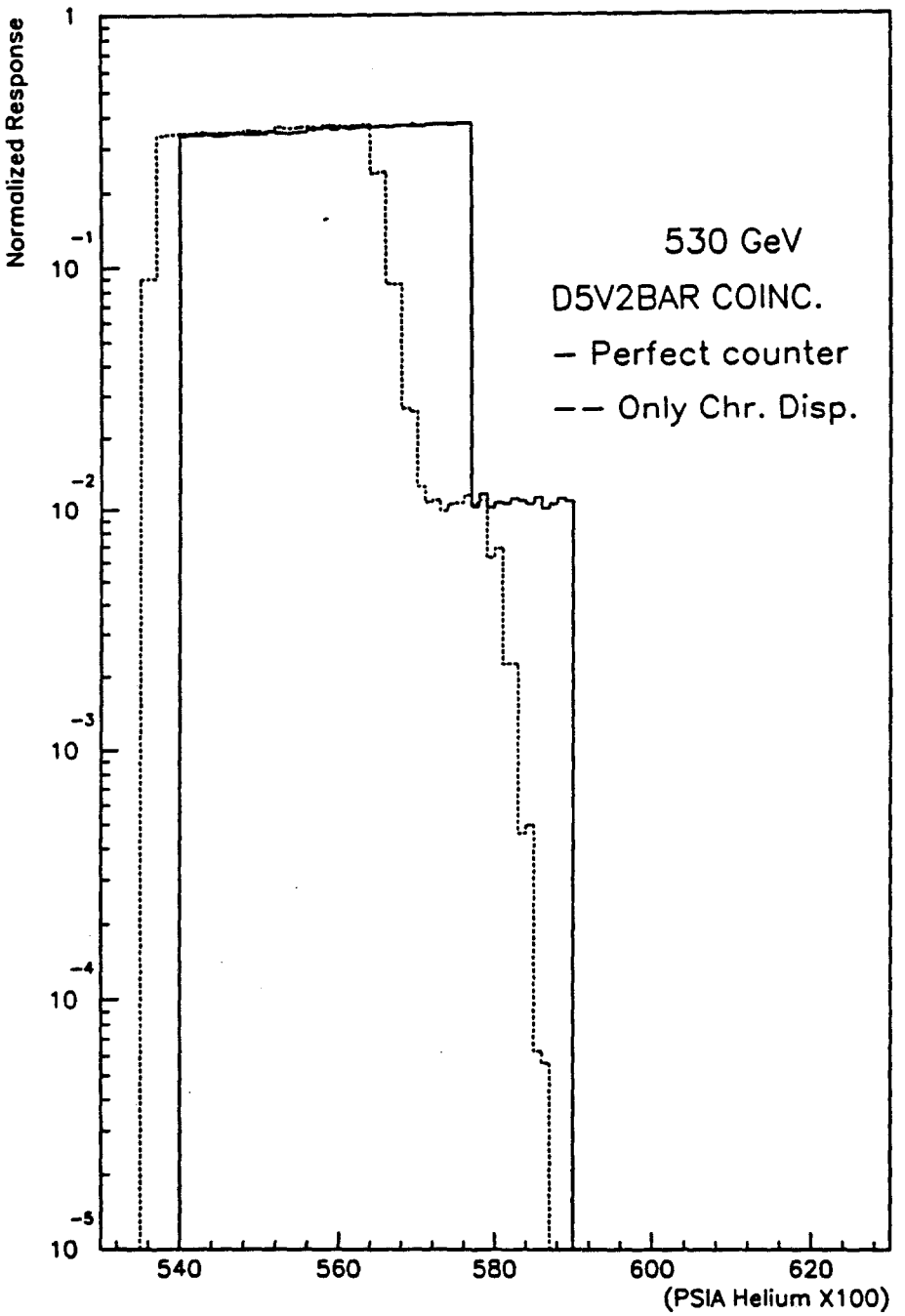

Figure 45: Effect of the chromatic dispersion to the resolution of the Cherenkov counter. Solid line: Perfect counter. Dashed line: Counter with only chromatic dispersion.

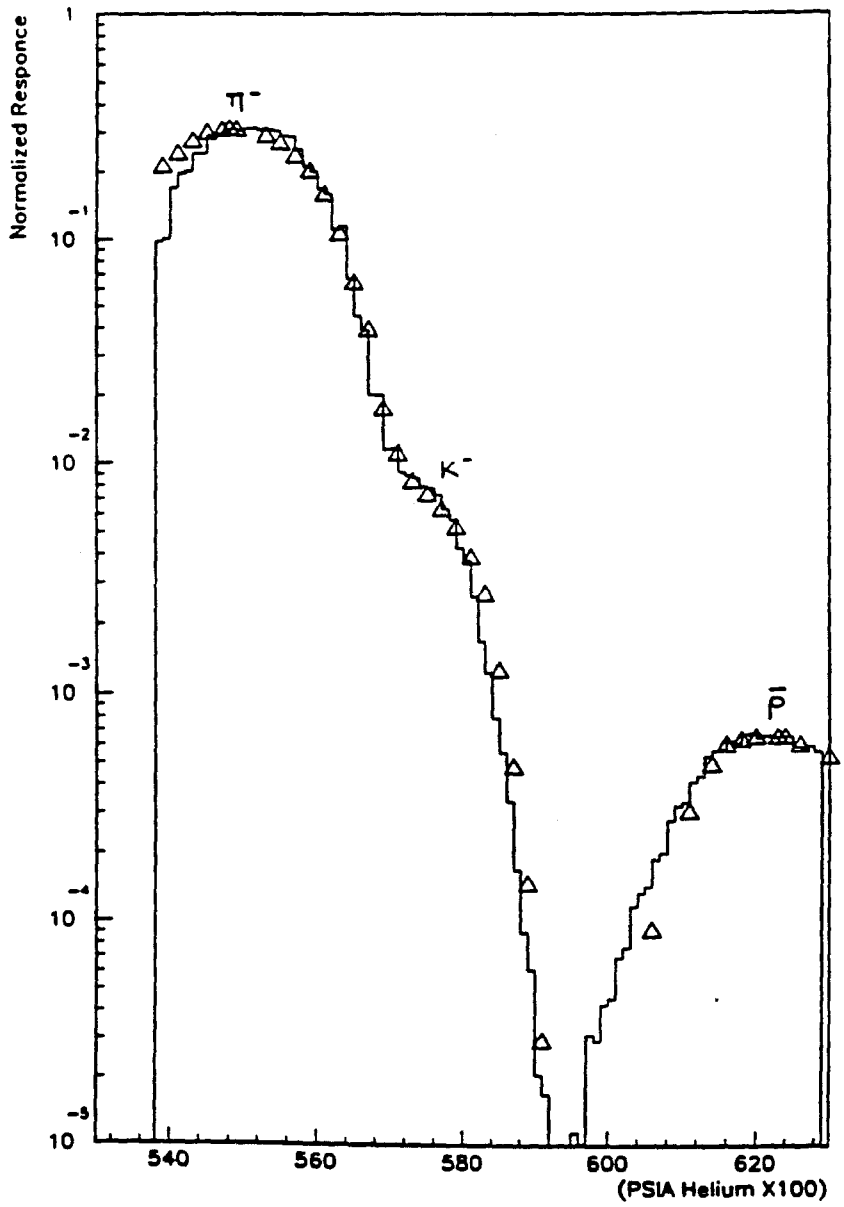

Figure 46: Comparison of the Monte Carlo pressure curve to the experimental data one at -530 GeV for the 3/4 interaction length Al target and the $D5\overline{V2}$ coincidence level.

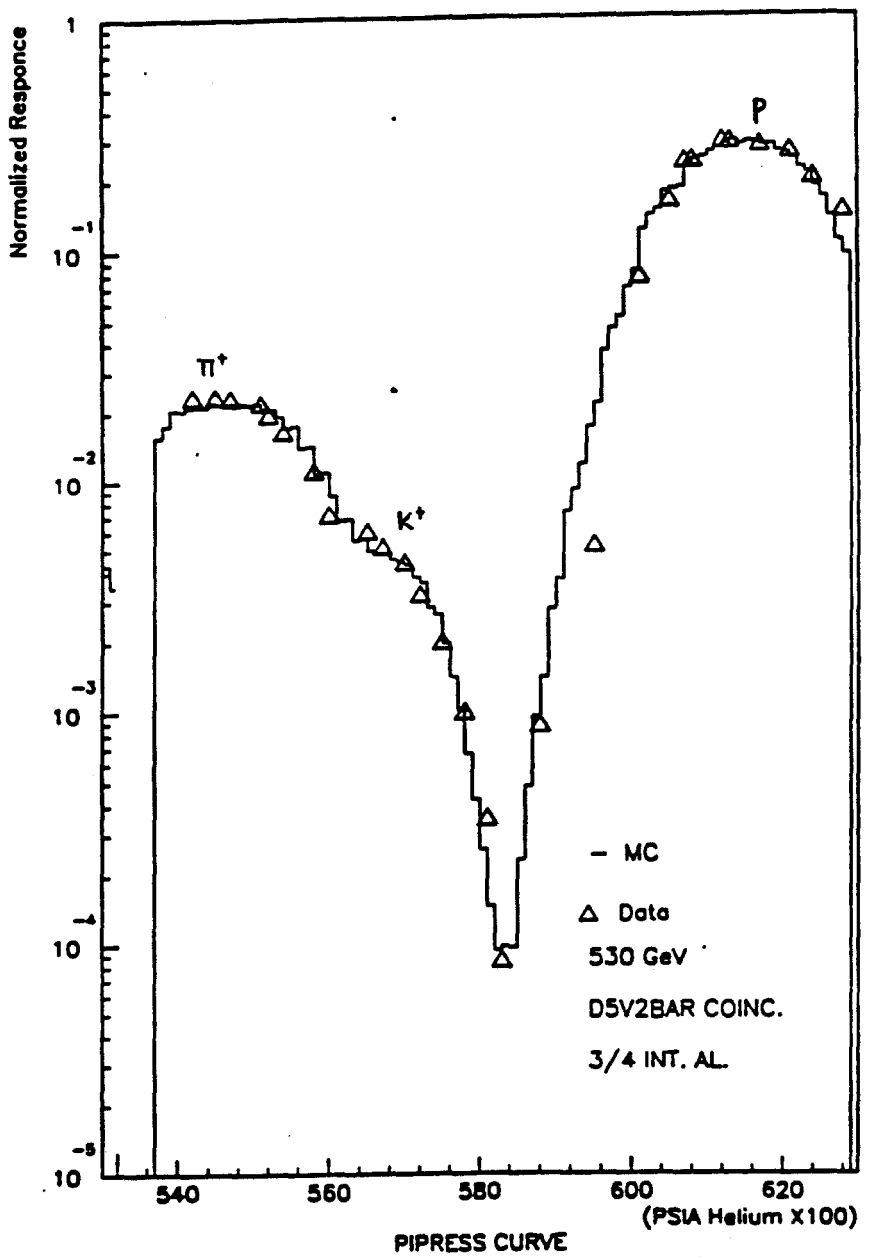

Figure 47: Comparison of the Monte Carlo pressure curve to the experimental data one at 530 GeV for the 3/4 interaction length Al target and the $D5\overline{V}2$ coincidence level.

were getting 1.1 photoelectrons per phototube per particle which is about half of what was expected, if the counter's optics were reflecting down to 220 nm as expected. This suggests the fact that most of the short wavelength photons were absorbed by the plastic light guides. This loss of light was responsible for the low observed efficiencies but also had a beneficial effect which was an improvement in the counter's resolution because the chromatic dispersion decreased. As a result the π-K resolution improved. This observation was also confirmed by the Monte Carlo program (Fig. 48). The best estimate of the actual accepted wavelength range is 300-600 nm.

4.4.2 Negative Beam Tagging

The negative 530 GeV beam that was used during the last E-706 run was composed mostly of π^- ($\sim$ 97%) and K^- ($\sim$ 3%). The fraction of antiprotons was small$\sim$ 0.2%. The Cherenkov counter was used to tag the minority particles (K^-), and everything that was not tagged as a K^- was called a π^- (the antiprotons were ignored).

The coincidence requirement that was chosen for tagging was $D4\overline{V2}$ which was the most efficient with sufficient separation between πs and Ks. The pressure point at which the counter was set was chosen so as to tag as many K^-s as possible, with the smallest possible contamination.

The exact composition of the negative beam at 530 GeV was determined by fitting the M.C pressure curve to the experimental one for the $D5\overline{V2}$ coincidence

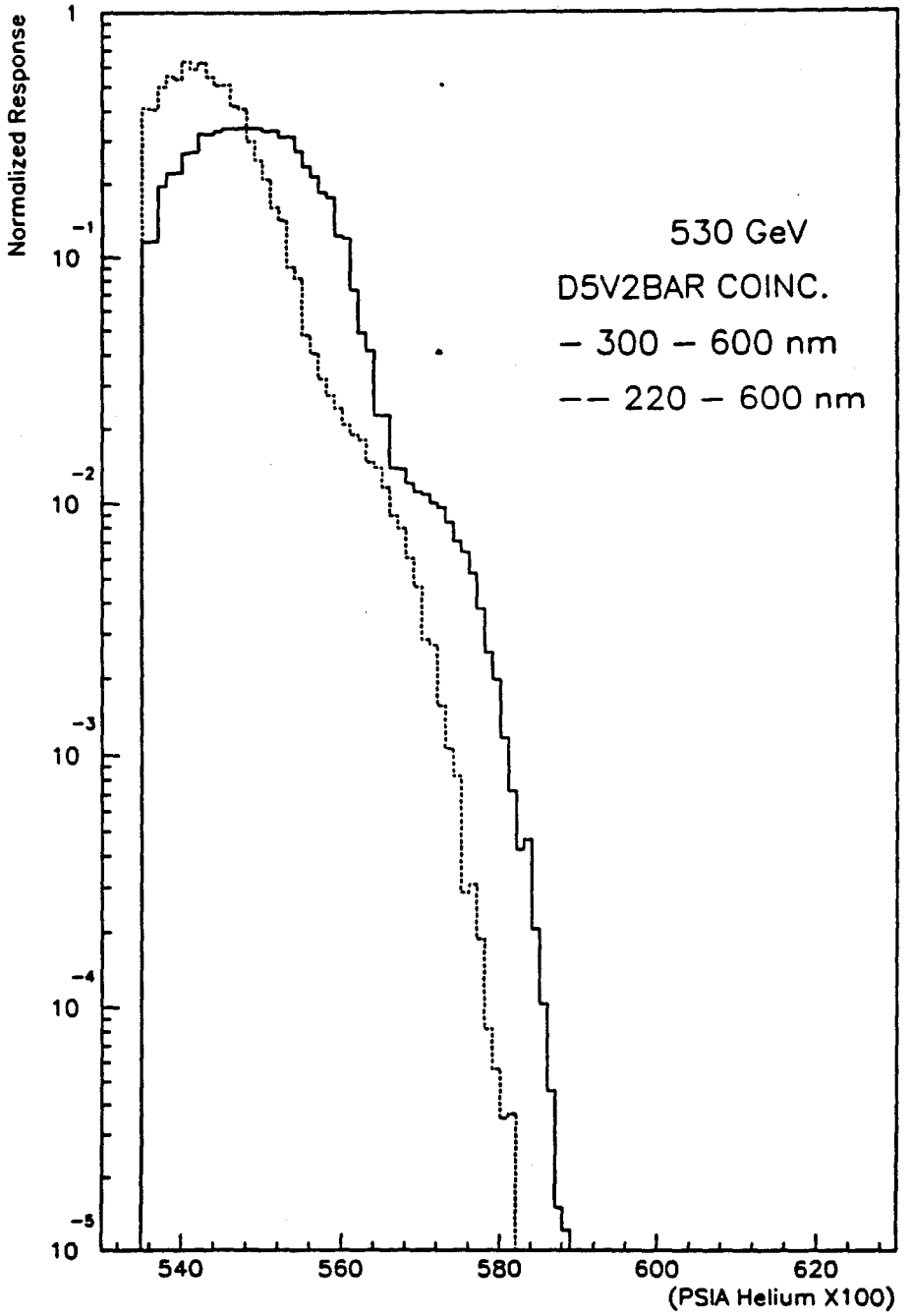

Figure 48: Effect of the accepted wavelength range on the resolution of the Cherenkov counter at -530 GeV. (top): 220-600 nm. (bottom): 300-600 nm.(97% πs and 3% Ks)

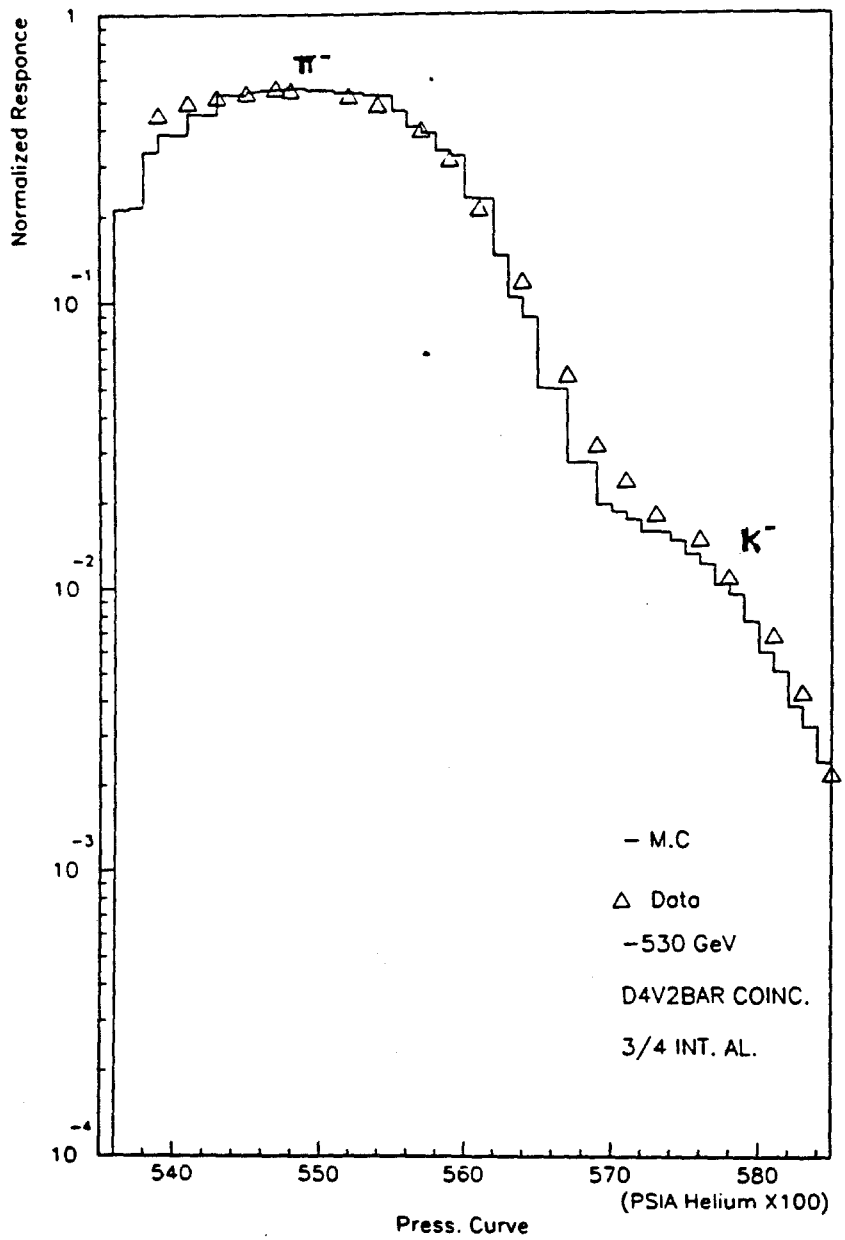

Figure 49: Comparison of the Monte Carlo pressure curve to the experimental data one at -530 GeV for the 3/4 interaction length Al target and the $D4\overline{V}2$ coincidence level.

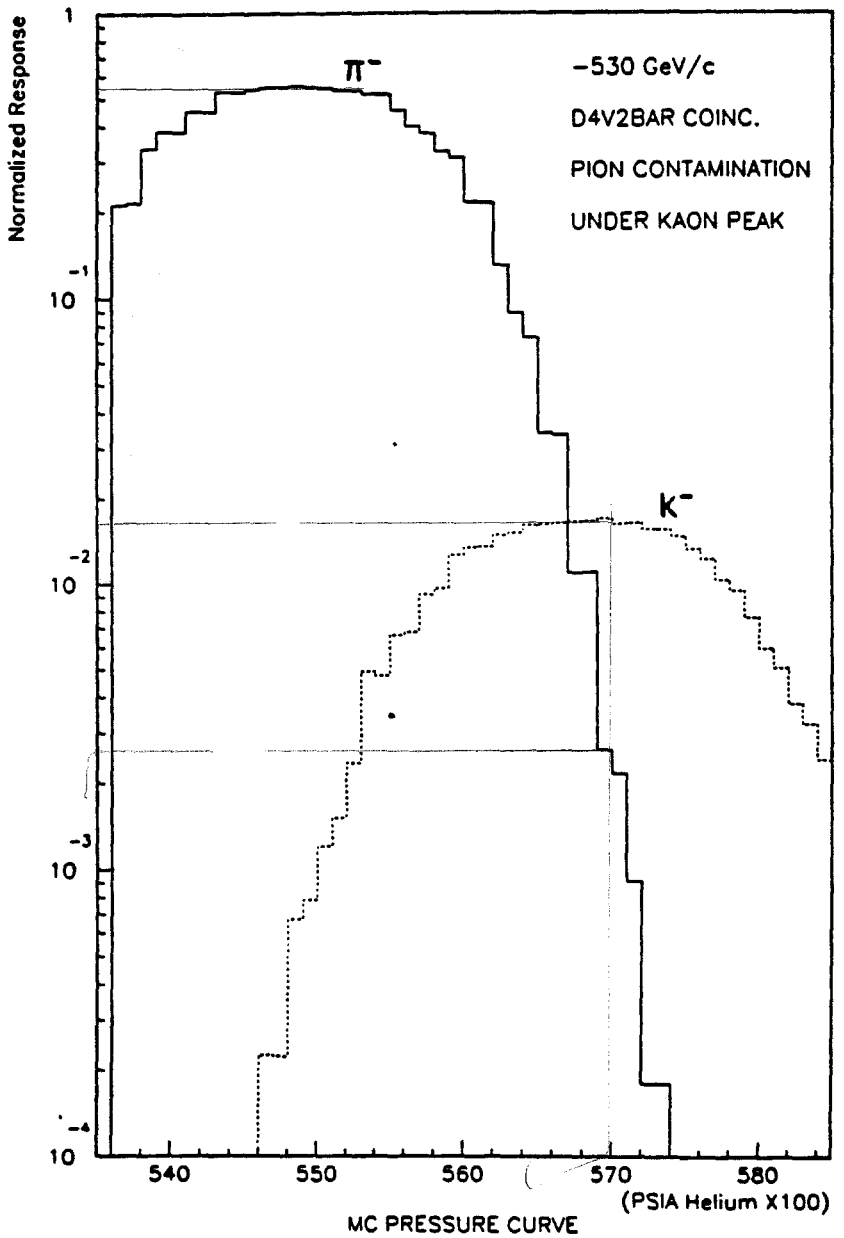

Figure 50: π^- contamination under the K^- peak at -530 GeV for the 3/4 interaction Al target and the $D4\overline{V2}$ coincidence level.

requirement (Fig. 47). The composition was determined to be: $(2.90 \pm 0.2)\%$ K^-, $(96.9 \pm 0.2)\%$ π^-, $(0.20 \pm 0.01)\%$ $\bar{p}$(the percentage of electrons and muons is on the order of 1%). The Monte Carlo with the fixed particle ratios and beam parameters was then used to to estimate the contamination to the K^-s due to the π^-s at the operating pressure point for the $D4\overline{V2}$ coincidence level (Fig. 50). The experimental $D4\overline{V2}$ pressure curve with the Monte Carlo curve superimposed on it is shown in Fig. 49. Since there were two negative runs, and the pressure points where the counter was set were not exactly the same (mainly due to different temperatures), the percentage of the beam tagged as K^- and the contaminations were run dependent.

For the first negative run (16-25 Jan. 1988), the Cherenkov counter was 58% efficient using the $D4\overline{V2}$ coincidence requirement, and 1.20% of the beam particles were tagged as K^- with less than 0.5% contamination due to π^- (less than 0.5% of the 1.20% tagged as K^- were π^- as was determined by Monte Carlo). For the second negative run (9-14 Feb. 1988), the Cherenkov efficiency was the same and 1.65% of the beam particles were tagged as K^- with less than 5% contamination due to π^-. In both runs everything that was not tagged as a K^- was called a π^-. The contamination of the π^-s by K^-s was less than 1%.

4.4.3 Positive Beam Tagging

The positive 530 GeV beam was composed mostly of protons ($\sim$ 90%), some π^+ ($\sim$ 7%) and a few K^+ ($\sim$ 1.5%). In this case, it was not possible to use

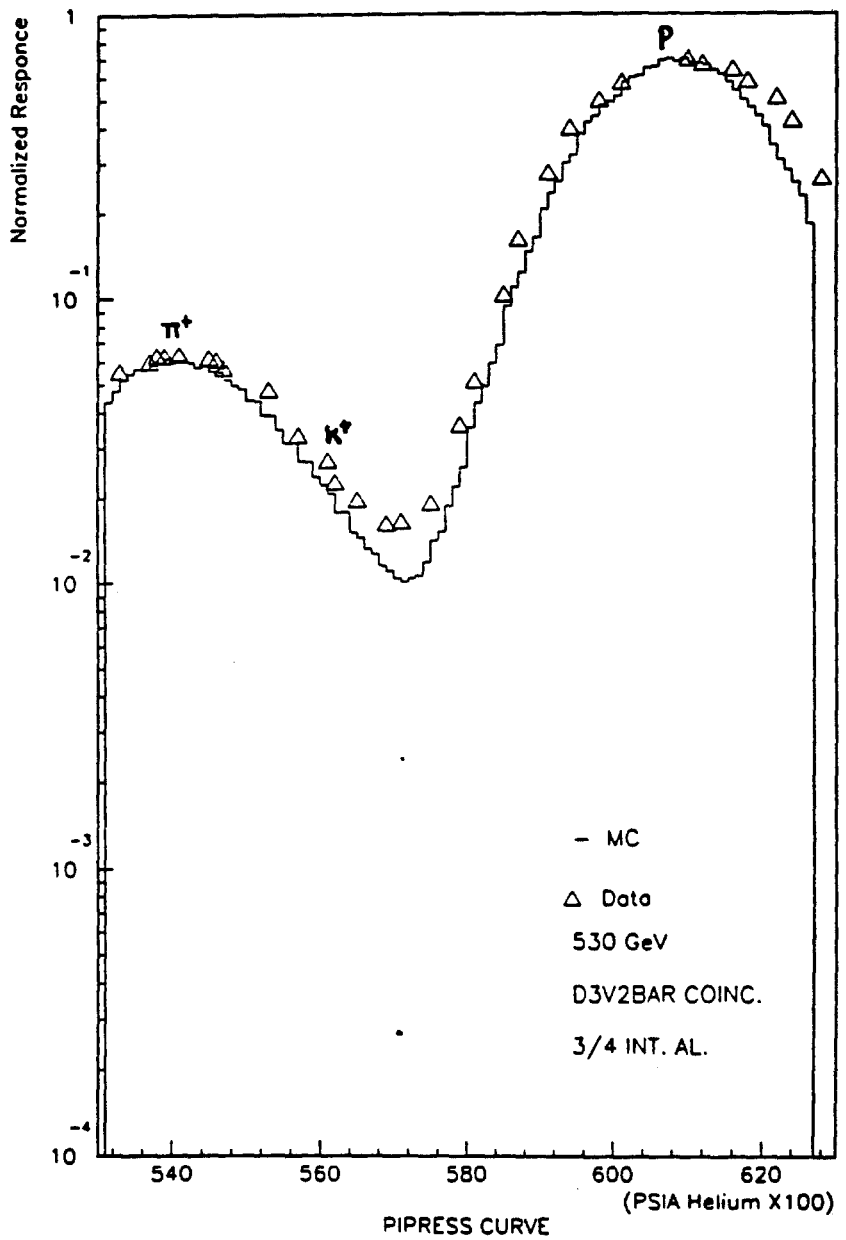

Figure 51: Comparison of the Monte Carlo pressure curve to the experimental data one at 530 GeV for the 3/4 interaction length Al target and the $D3\overline{V}2$ coincidence level.

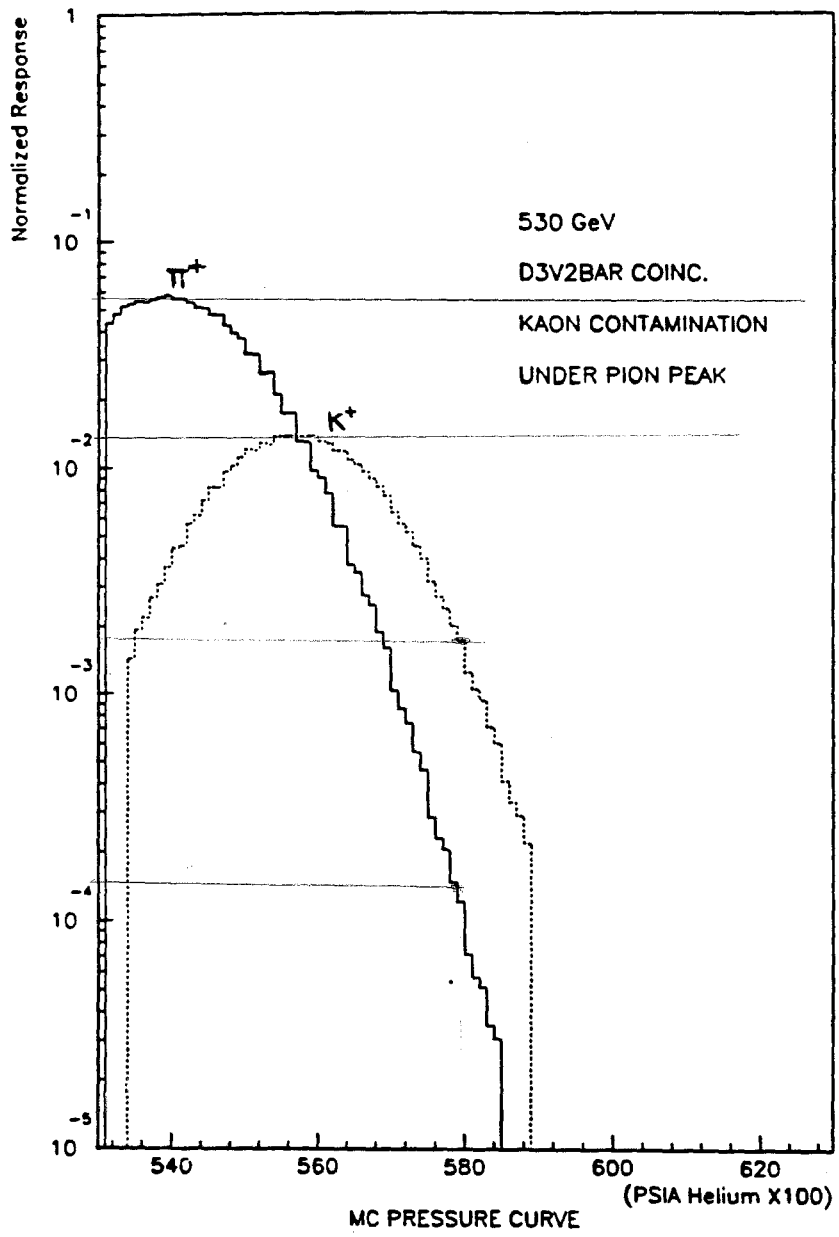

Figure 52: K^+ contamination under the π^+ peak at 530 GeV for the 3/4 int. length Al target and the $D3\overline{V2}$ coincidence level.

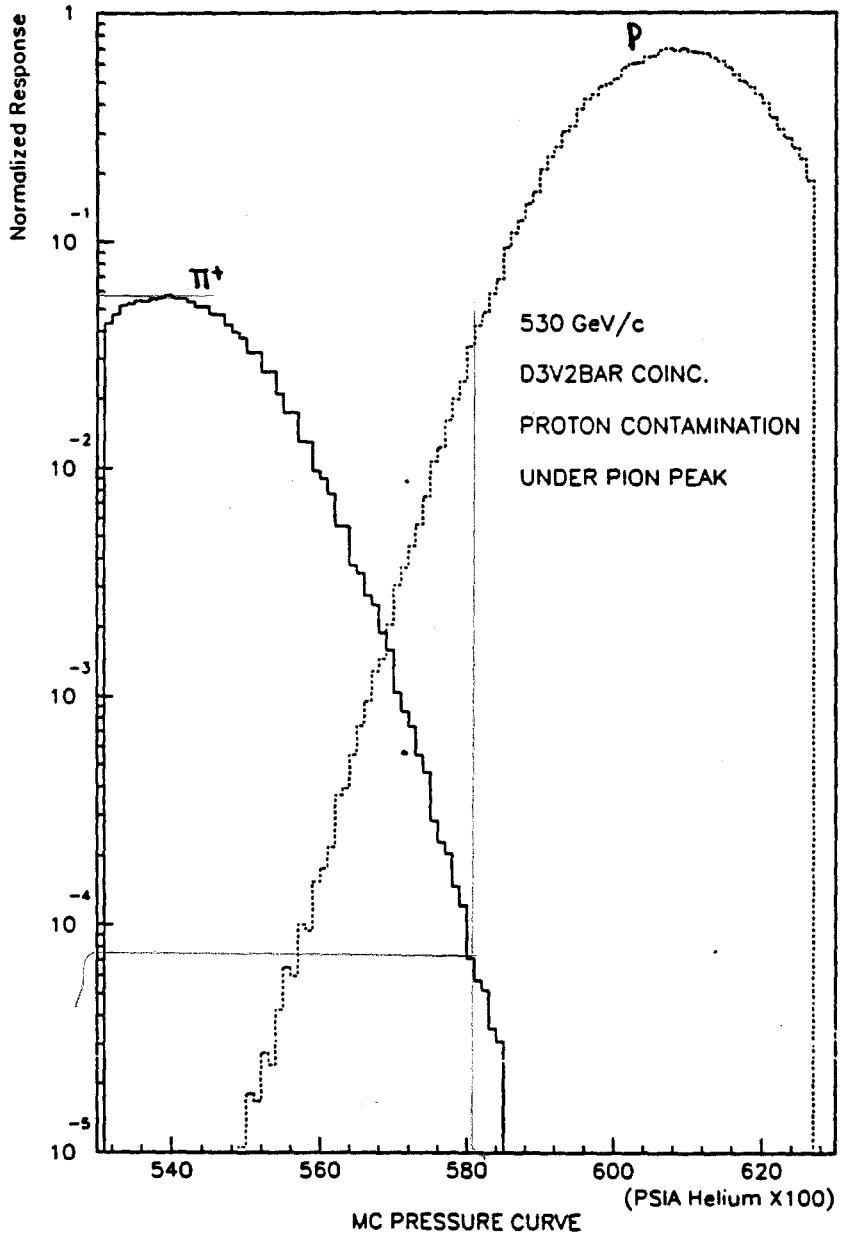

Figure 53: p contamination under the π^+ peak at 530 GeV for the 3/4 int. Al target and the $D3\overline{V2}$ coincidence level.

the Cherenkov counter to tag kaons as in the case of the negative beam, unless we wanted to have a dedicated kaon run because both the proton and pion fluxes were large. Instead, we used the Cherenkov to tag π^+s, considering the K^+s negligible and calling all the particles that were not tagged as π^+, protons.

The Cherenkov pressure was set at the pion peak and then we selected the coincidence requirement, $D3\overline{V2}$, which had the biggest efficiency and the smallest contamination.

The composition of the positive beam was determined as before by first fitting the $D5\overline{V2}$ curve (Fig. 48). The beam population was determined to be: $(7.2 \pm 0.2)\%$ π^+, $(1.7 \pm 0.1)\%$ K^+, and $(91.2 \pm 0.1)\%$ p(The percentage of electrons and muons was smaller than 0.5%). The contamination under the π^+ peak due to K^+ for the $D3\overline{V2}$ coincidence was determined from the Monte Carlo to be about 8%, while the contamination due to protons was negligible (Fig. 52 ,53). The experimental $D3\overline{V2}$ pressure curve with the Monte Carlo curve superimposed on it is shown in Fig. 51.

At the $D3\overline{V2}$ coincidence level we were 78.0% efficient and $(6.3 \pm 0.1)\%$ of the beam was tagged as π^+ with 8.0% contamination due to K^+. So the measured fraction of π^+s in the beam is:

$$\pi^+\% = \frac{(6.3 - 6.3 \times 0.08)}{0.78}\% = (7.4 \pm 0.1)\% \tag{4.37}$$

5. PARTICLE PRODUCTION DATA ANALYSIS

In this chapter, I will describe all the corrections made to the raw Cherenkov pressure curves in order to calculate the single particle inclusive invariant cross sections $Ed^3\sigma/dp^3$.

5.1. INTRODUCTION

Three different targets (Al, Be, W) were used to measure the A-dependence of the single particle inclusive invariant cross sections at ±530 GeV. The negative data were taken at a 0° production angle. The positive data had to be taken at a 1.4 mrad production angle. Cross sections were also measured at -200 and -400 GeV at 0° on Al and W (The main reason for not using more targets was the fact that the primary target fixture allowed only two targets at a time). The physical dimensions of the different targets used are listed in Table 11 below

TABLE 11

MATERIAL	W (cm)	H (cm)	L (cm)	$L/L_{INT.}$
BERYLIUM (Be)	1.18	0.89	7.34	0.18
ALUMINUM (Al)	0.97	0.96	3.06	0.08
ALUMINUM (Al)	0.97	0.96	30.54	0.77
TUNGSTEN (W)	0.96	0.96	0.95	0.10

TABLE 11: Physical Dimensions of the various targets used for the particle

production data. (W=Width; H=height; L=length; L_{INT}=the interaction length in the materials indicated.)

Production angles were selected according to the procedure described in Chapter 2. The transverse momentum acceptance Δp_T is determined by the horizontal and vertical beam acceptance. The beam angular acceptances are determined by the collimator openings. The typical transverse momentum acceptance for our data is given by:

$$\Delta p_T(MeV) = 0.4 \times p \tag{5.1}$$

where p is the secondary beam momentum in GeV. The average p_T of our negative data is estimated to be:

$$< p_T >_- (MeV) = 0.2 \times p \tag{5.2}$$

with p being the secondary momentum in GeV. Since all the positive data are taken at the secondary momentum of 530 GeV and production angle of 1.4 mrad, the average p_T for the positive data is:

$$< p_T >_+ = 720 MeV \tag{5.3}$$

The Cherenkov counter pressure curves taken at ±530 GeV for each target were fitted with the curves generated by the Monte Carlo program to extract the ratios of the various particles in the beam. At the other energies, the different particle peaks were well separated so that these ratios could be determined directly without fitting.

5.2. Beam Momentum

The determination of the momentum of the secondary beam relies on knowing the excitation curves of the bending magnets. These are known to within an error of about 1%. The exact values of the beam momenta as determined by the currents in the bending magnets were given in Chapter 3. An independent determination of the beam momentum was done by using the Monte Carlo pressure curves. The input momentum in the Monte Carlo program was varied in order to get the same separation between the particle peaks as in the measured pressure curves. The results are listed in Table 12 along with the momentum values determined from the magnet currents.

TABLE 12		
BEAM MOMENTUM		
Nominal Value	M.C. Value	Magnet Value
-200	$-190. \pm 1.$	$-189. \pm 1.$
-400	$-380. \pm 5.$	$-379. \pm 3.$
± 530	$\pm 512. \pm 6.$	$\pm 508. \pm 5.$

TABLE 12: Beam momentum values.

The numbers in Table 12 show that there is a good agreement in the values determined by the two methods. Note that the values in Table 12 refer to the central momentum of the beam, the errors, $\pm$ indicate the uncertainty in the central momentum, not the momentum bite of the beam. Also throughout this thesis I refer to the beams by their Nominal Values rather than their actual ones.

5.3. Acceptance Calculations

The MW beamline, as was mentioned in Chapter 2, had an angular acceptance of 0.61 μsr and a momentum acceptance of 12.5%. For the particle production data we used the collimators in the beamline to reduce the angular and momentum acceptances of the MW beamline. The reduced collimator openings also improved the Cherenkov resolution and efficiency by reducing the beam divergence and the momentum bite. The collimator openings used were chosen from the collimator curves (beam flux as a function of one collimator opening, the other three remaining open) that were taken at the beginning of the run. The collimator curves were also used to determine the offsets in the positions of each collimator.

Two basic collimator configurations were used for the ±530 GeV data, but for the -200 and -400 GeV data there were four different configurations. The acceptances for each configuration were calculated with the TURTLE program with the actual collimator positions and an isotropic production model. A large number of particle rays (80,000) were generated at the beginning of the beamline and then were traced through the magnetic elements to the Cherenkov detector. The fraction N/N_0, the number of particles that reached the detector with the limiting collimator openings divided by the number of particles that reached the detector with open collimators (for the same number of incident particles) gave us the fraction of the maximum beam acceptance used in the particular configuration. The collimator openings for each beam configuration along with the corresponding acceptances are listed in Table 13.

TABLE 13						
	COLLIMATOR OPENINGS (cm)					
TARGETS AND ENERGIES	MW7CH1	MW7CV1	MW7CH2	MW7CV2	N/N_0	A (μsr%
-530 GeV Al,W	4.01	2.43	1.28	2.52	0.200	3.05
530 GeV Be,Al,W	2.54	0.81	2.54	10.00	0.110	1.68
-400 GeV Al	1.10	1.33	1.55	1.96	0.046	0.71
-400 GeV W	0.85	0.68	0.91	10.00	0.011	0.16
-200 Gev Al	1.27	1.27	1.27	1.27	0.046	0.69
-200 GeV W	0.80	0.32	1.24	10.00	0.0066	0.099

TABLE 13: Collimator openings and acceptances for the various beam configurations used.

5.4. Background Subtraction

For each target, energy and beam configuration, the background was measured by moving the primary target out of the beam and measuring the coincidence of the two scintillation counters upstream and downstream of the Cherenkov counter normalized by the number of incident protons (The incident proton flux was measured with a secondary emission monitor located just upstream of the target). The "empty target" position was determined by the target scans which were done regularly. The results of a typical target scan is shown in Fig. 54.

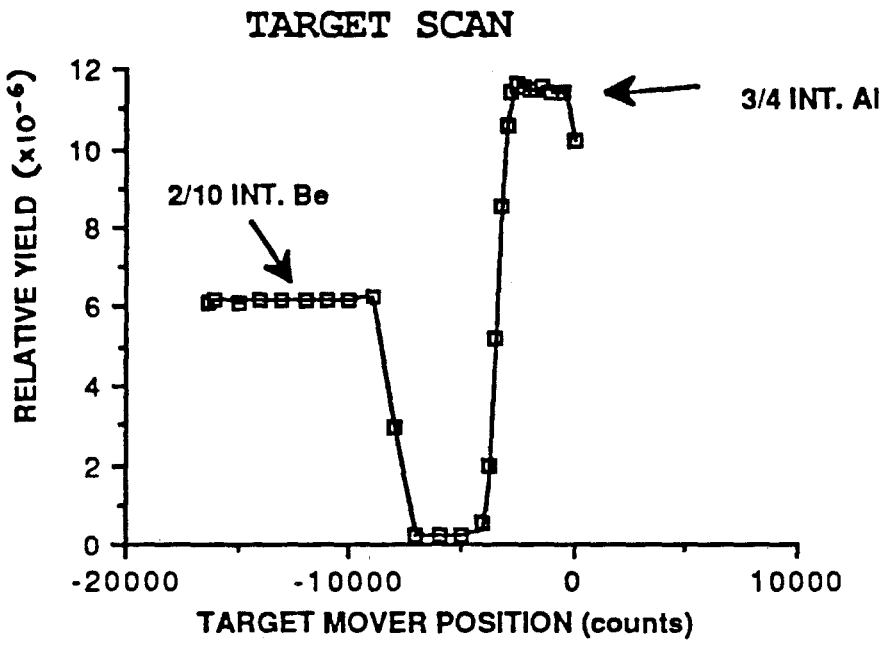

Figure 54: Typical target scan.

The measured background varied from 2% for the long Al target and the negative 530 GeV data to 18.0% for the W target and the negative 200 GeV data. All the background measurements were taken with the same beam configuration as the data; the results are listed in Table 14.

TABLE 14				
	BACKGROUND AT EACH ENERGY (%)			
TARGET	+530 GeV	-530 GeV	-400 GeV	-200 GeV
Be	4.0	5.0	-	-
Al (3.06 cm)	-	10.0	-	-
Al (30.54 cm)	2.9	2.0	2.5	2.0
W	14.2	9.0	18.0	18.0

TABLE 14: Measured background at each momentum.

5.5. Particle Decays and Absorption in the Beam

The Cherenkov counter was 190.8 m from the primary production target so unstable particles (π, K) could decay before reaching the counter. The probability that a particle of mass m and proper mean life τ_0 goes a distance greater than x before decaying is:

$$Prob.(> x) = e^{-x/\gamma\beta c\tau_0} = e^{-mx/pc\tau_0} \tag{5.4}$$

where p is the particle momentum. In Table 15 I list this probability for $x > 19080$ cm for the πs and Ks.

TABLE 15		
Momentum	Prob($x > 19080$ cm) ($\pi^{\pm}$)	Prob($x > 19080$ cm) ($K^{\pm}$)
200	0.9826	0.8778
400	0.9913	0.9369
530	0.9936	0.9531

TABLE 15: Probability for the πs and Ks to reach the end of the Cherenkov counter.

Care was taken not to have any extra material in the beam. Most of the beamline was enclosed in a vacuum pipe. For practical reasons it was necessary to break the beam vacuum in some places in order to place scintillators and beam locating devices. Table 16 lists all the material in the beam up to the end of the Cherenkov counter. The interaction length listed in the Table 16 is for protons. For pions and kaons the interaction length is about 25% larger.

5.6. Muon and Electron Contamination

At the energies at which the particle production data were taken, electrons and muons were indistinguishable from pions in the Cherenkov counter. Thus, the pion data had to be corrected for this contamination.

The muons in the beam were measured using the two pairs of collimators (MW7CH1-V1, MW7CH2-V2). The first pair (MW7CH1,V1) was located 135 ft (41.15m) downstream from the primary target, while the second pair (MW7CH2,

TABLE 16			
Material and Length	**Center in z (ft)**	λ_I (%)	L_R (%)
Air 59.92 ft	29.96	2.578	5.992
Beam Pipe Window 6 mil Ti	59.92	0.0550	0.430
Beam Pipe Window 6 mil Ti	354.0	0.0550	0.430
Air 1 ft	354.5	0.0430	0.100
MW7WC2 + 1/8" G-10	354.5	0.799	1.500
Beam Pipe Window 6 mil Ti	355.0	0.0550	0.430
Beam Pipe Window 6 mil Ti	625.5	0.0550	0.430
1/8" S2 scintillator	625.8	0.390	0.750
MW8WC1 + 1/8"G-10	626.2	0.799	1.500
Air 1.75 ft	626.4	0.075	0.175
Cherenkov Window 10 mil Ti	626.5	0.092	0.710
He 138.12 ft ($\rho = 0.0624 g/l$)	708.4	0.400	0.270
Cherenkov Mirror 100 mil Glass	793.5	0.580	2.00
Cherenkov Window 10 mil Ti	794.5	0.092	0.710
Air 3.25 ft	796.1	0.140	0.325
MW8WC2 + 1/8" G-10	795.0	0.799	1.50
Total up to the end of the Counter		**7.00**	**17.25**

TABLE 16: Material at the MW-beamline up to the end of the Cherenkov counter, expressed as a fraction of the proton nuclear interaction length λ_I and the radiation length L_R.

CV2) was 360 ft (109.73m) downstream from the primary target. Each collimator consisted of 2.4 m of steel. When the collimator was closed only the muons get through the beamline. For each beam configuration, we first measured the flux at the Cherenkov counter ($S2 \cdot S3/MW6SEM$). Then we closed the first pair of collimators, leaving the rest of the beamline unchanged, and again measured the flux at the Cherenkov. Last we opened the first pair to their previous settings and we closed the second pair of collimators and measured the flux one more time. The first of the measurements determined the number of muons coming from the beam dump area. The second determined to with 20% the increase in muon flux due to π and K decays in the space between the two collimator pairs. The muon flux at the end of the Cherenkov counter was estimated to be the flux measured with the second set of collimators closed plus the muons coming from pion and kaon decays in the space between the second set of collimators and the end of the Cherenkov counter (128 m). The percentage of muons in the beam up to the end of the Cherenkov counter for the various beam energies is listed in Table 17.

TABLE 17		
BEAM ENERGY (GeV)	ELECTRONS (%)	MUONS (%)
-200	5.7	2.5
-400	1.0	1.2
-530	-	1.0
530	-	0.14

TABLE 17: Percentage of electrons and muons in the beam for the different beam momenta.

The electrons in the beam were determined by using the calorimeter as was

described in Chapter 3. At ±530 GeV beam energy, there was no detectable electron signal in the calorimeter. The percentages of electrons in the beam for the various beam energies are listed in Table 17.

5.7. Accidental Coincidences

A correction was made for accidental coincidences between the two counters S2, S3 used to define the beam going through the Cherenkov. The singles rate in each counter was measured to be 10% larger than the coincidence rate and the time resolution of the system was 13 ns. The accidental coincidences were calculated to be 0.4% of the coincidence rate.

5.8. Target Thickness Correction

The measured cross sections were obtained for zero target thickness by correcting for absorption of the primary and secondary particles inside the target. For this correction we used a simplified reabsorption model in which the produced secondaries are reabsorbed in the target without producing additional particles. For a target of length L, this model gives a target production efficiency f^s, described

by:

$$f^s(L) = \frac{\epsilon^{-L/\lambda(s)} - \epsilon^{-L/(p)}}{1 - \frac{\lambda(p)}{\lambda(s)}} \tag{5.5}$$

where $\lambda(s)$ is the absorption length for the secondary s, and $\lambda(p)$ is the absorption length for protons. For secondary proton production, $\lambda(s) = \lambda(p)$ and the formula becomes:

$$f^s(L) = \frac{L}{\lambda(p)}\epsilon^{-L/\lambda(p)} \tag{5.6}$$

The absorption length in cm is given by:

$$\lambda(s) = \frac{A(\mathrm{gm}) \cdot 10^4}{6.023\sigma(s)(\mathrm{mb})\rho(\mathrm{gm/cm^3})} \tag{5.7}$$

where A is the atomic weight for the target material and $\sigma(s)$ is the absorption cross section for the secondary s and the target material. Absorption cross sections have been measured by Carrol et.al.[57] for several different materials. The production efficiencies f^s for the secondary s and for all of our targets are listed in Table 18.

TABLE 18						
TARGET	**LENGTH (cm)**	$f^{\pi^\pm}$	f^{K^-}	f^{K^+}	f^p	$f^{\bar{p}}$
BERYLLIUM (Be)	7.34	0.1460	0.1598	0.1598	0.1550	0.1416
ALUMINUM (Al)	3.06	0.0714	0.0878	0.0878	0.0706	0.0710
ALUMINUM (Al)	30.54	0.3861	0.3978	0.3978	0.3558	0.3540
TUNGSTEN (W)	0.960	0.0909	0.0910	0.0911	0.0900	0.0900

TABLE 18: Production efficiencies for the production targets and secondary particles.

The short aluminum target was used to test this target thickness correction. The model predicts that, the ratio of the π^- fluxes from the two targets at the Cherenkov counter should be equal to the ratio of the two corresponding f^s factors i.e,

$$\frac{[S2 \cdot S3/MW6SEM](3.06cm\ Al)}{[S2 \cdot S3/MW6SEM](30.54cm\ Al)} = \frac{f^{\pi^-}_{Al}(3.06cm)}{f^{\pi^-}_{Al}(30.54cm)} = 0.1849 \qquad (5.8)$$

This flux ratio was measured to be 0.1846, in very good agreement with the predicted value.

5.9. SEM Calibration

The MW6SEM secondary emission monitor immediately upstream of the MW primary target was used to measure the intensity in terms of protons per spill of the 800 GeV primary proton beam reaching the MW primary target. This is a crucial beam counting device for the particle production data since it provides the normalization for all particle production data.

Since proper calibration of the SEM was essential and MW6SEM was last calibrated two years before the '87-'88 fixed target run, we did another calibration at the end of the run. The calibration was carried out using the foil packet activation technique. A foil packet consisting of a 0.005" thick copper foil with two 0.0007" cover foils was placed directly in front of the SEM for 15 minutes while beam was running. The amount of activity in the copper foil was then measured and compared to the readings given by the SEM during the test.

TABLE 19					
p (GeV)	p_T (MeV)	Target Material	π^+ (%)	K^+ (%)	p (%)
530	720	Be	6.9 ± 0.4	1.3 ± 0.1	91.8 ± 0.5
530	720	Al	7.1 ± 0.4	1.5 ± 0.2	91.4 ± 0.5
530	720	W	6.6 ± 0.4	2.3 ± 0.3	91.1 ± 0.5

TABLE 19: Positive particle contents of the beam for various targets at 530 GeV.

TABLE 20					
p (GeV)	p_T (MeV)	Target Material	π^- (%)	K^- (%)	$\bar{p}$ (%)
-530	0	Be	96.5 ± 0.4	3.2 ± 0.3	0.25 ± 0.02
-530	0	Al	96.9 ± 0.3	2.9 ± 0.3	0.20 ± 0.02
-530	0	W	97.2 ± 0.3	2.6 ± 0.3	0.19 ± 0.02
-400	0	Al	95.7 ± 0.3	3.8 ± 0.2	0.45 ± 0.04
-400	0	W	95.9 ± 0.3	3.3 ± 0.2	0.75 ± 0.06
-200	0	Al	93.0 ± 0.4	5.8 ± 0.3	1.20 ± 0.06
-200	0	W	93.8 ± 0.4	5.1 ± 0.3	1.10 ± 0.06

TABLE 20: Negative particle contents of the beam for different targets and momenta.

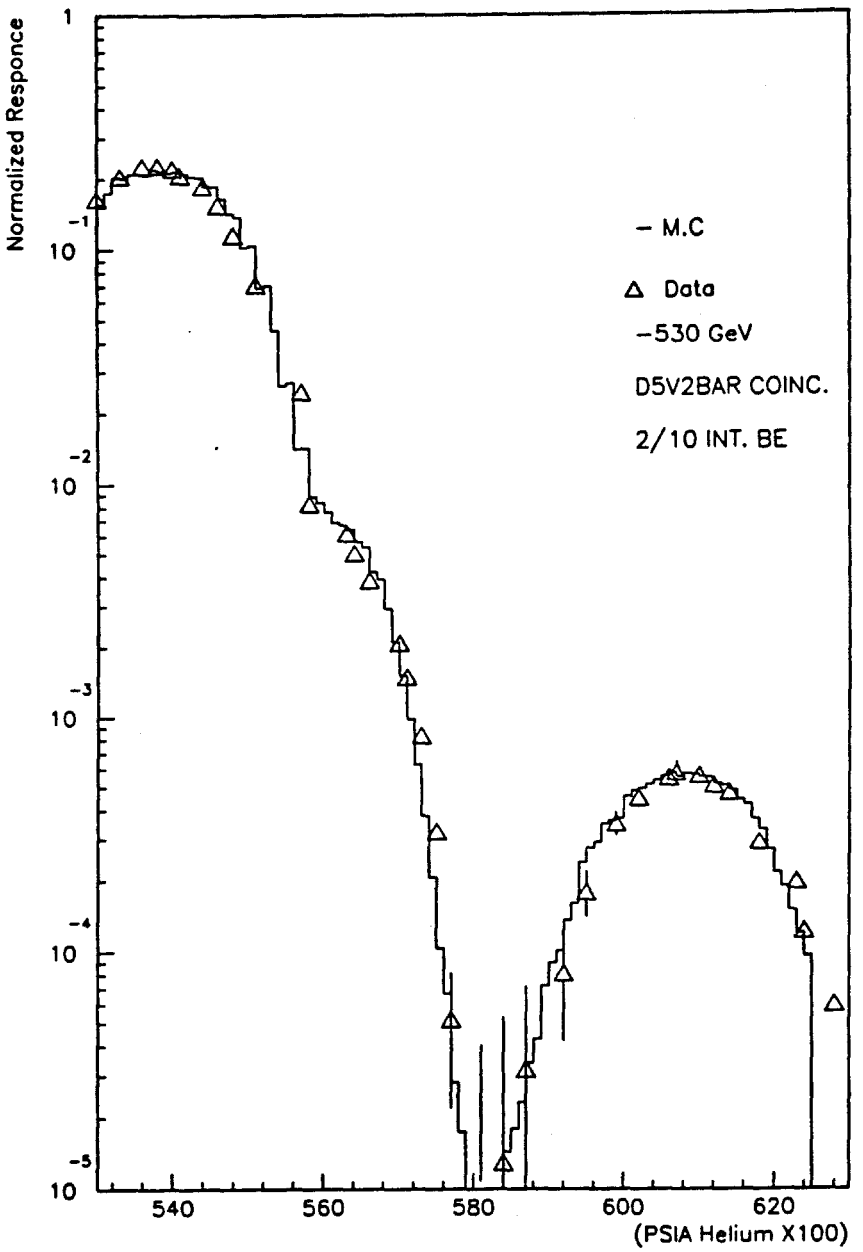

Figure 55: Monte Carlo fit for the $D5\overline{V2}$ Be pressure curve at -530 GeV.

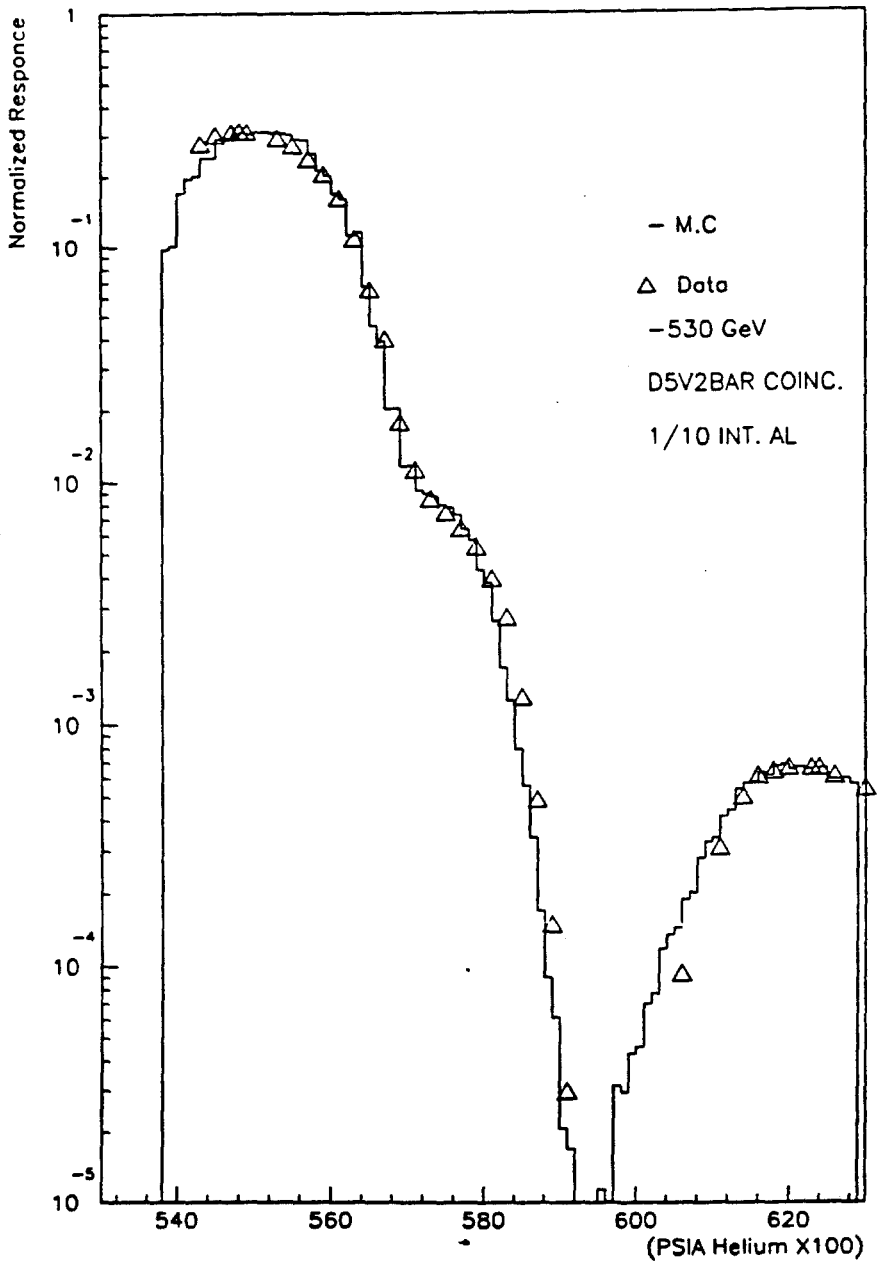

Figure 56: Monte Carlo fit for the $D5\overline{V2}$ Al pressure curve at -530 GeV.

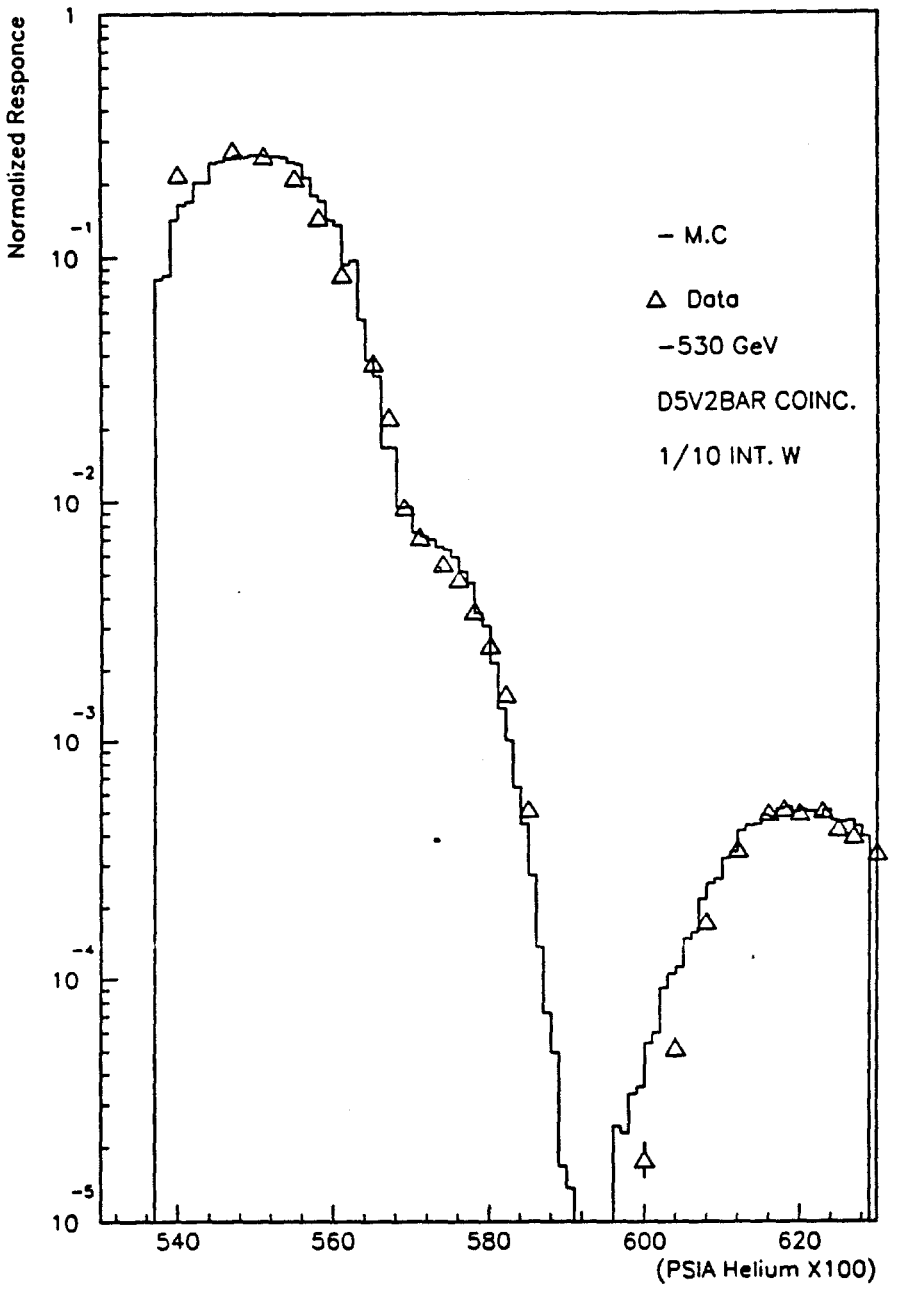

Figure 57: Monte Carlo fit for the $D5\overline{V2}$ W pressure curve at -530 GeV.

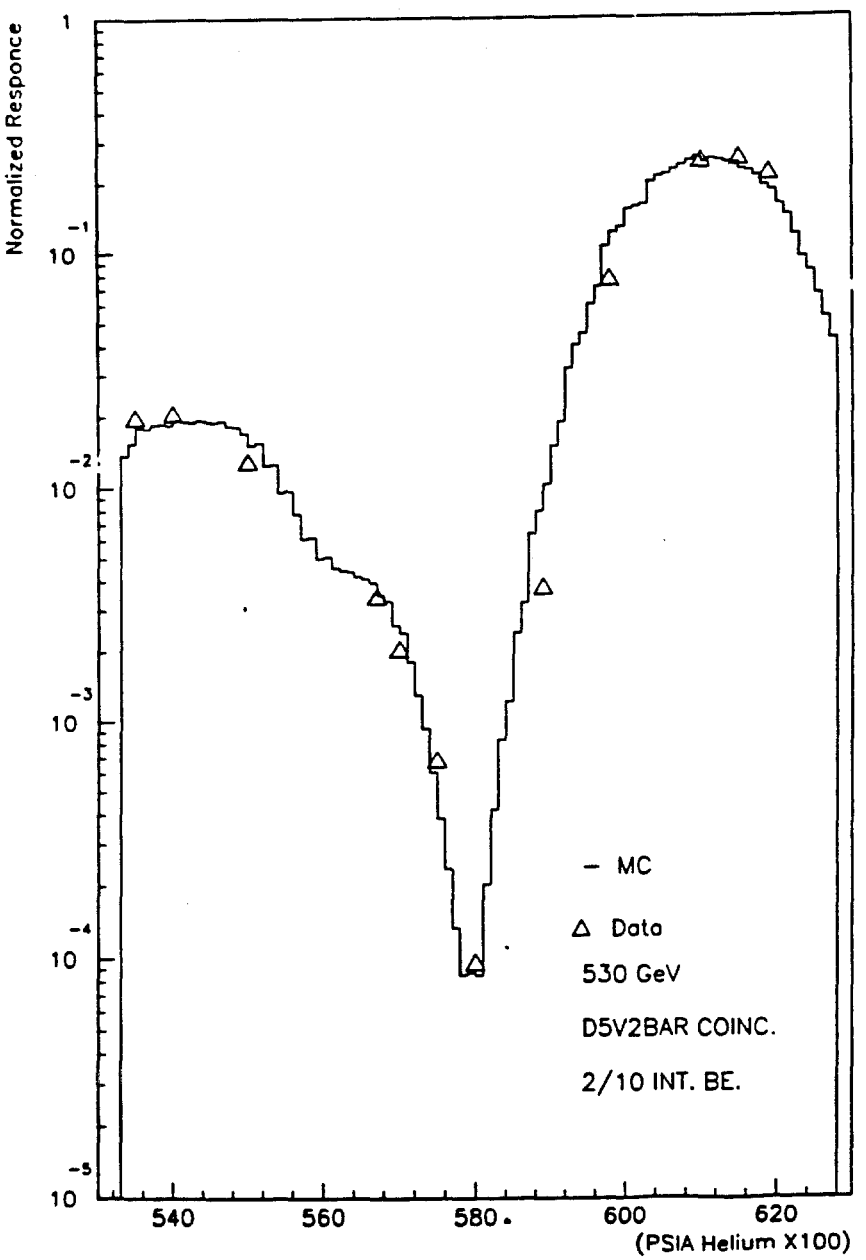

Figure 58: Monte Carlo fit for the $D5\overline{V2}$ Be pressure curve at 530 GeV.

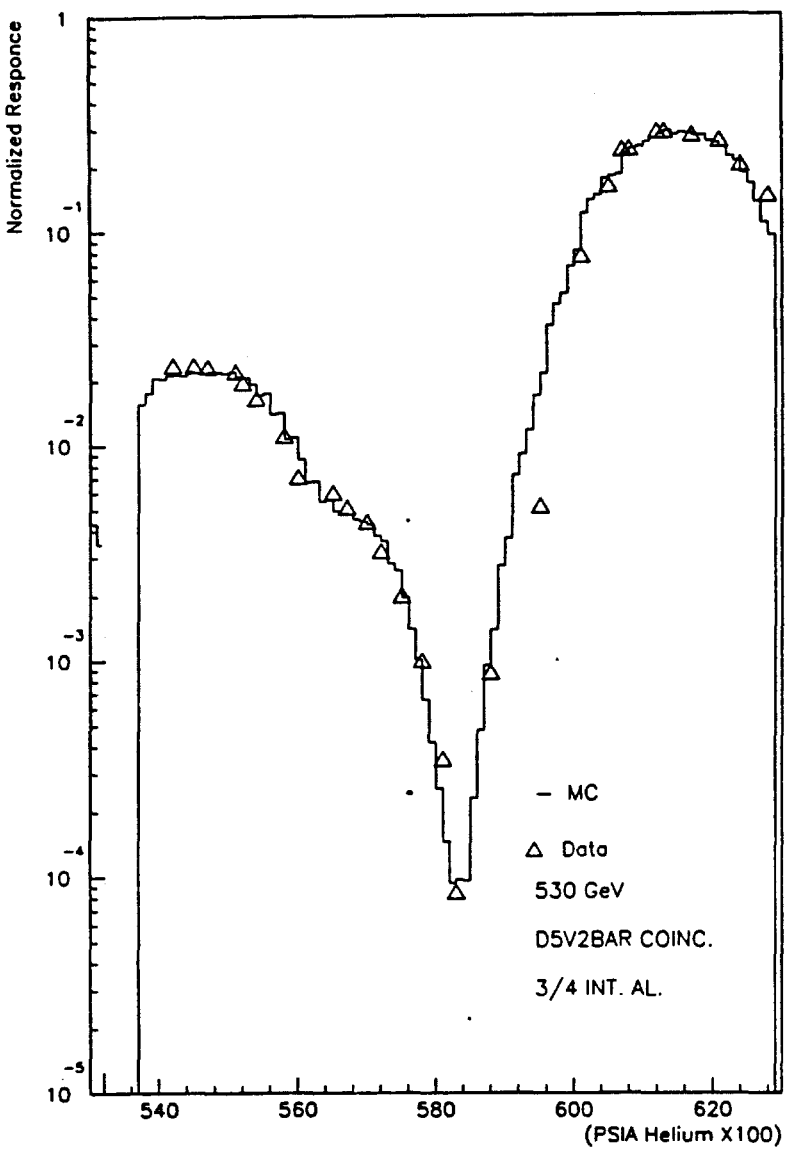

Figure 59: Monte Carlo fit for the $D5\overline{V2}$ Al pressure curve at 530 GeV.

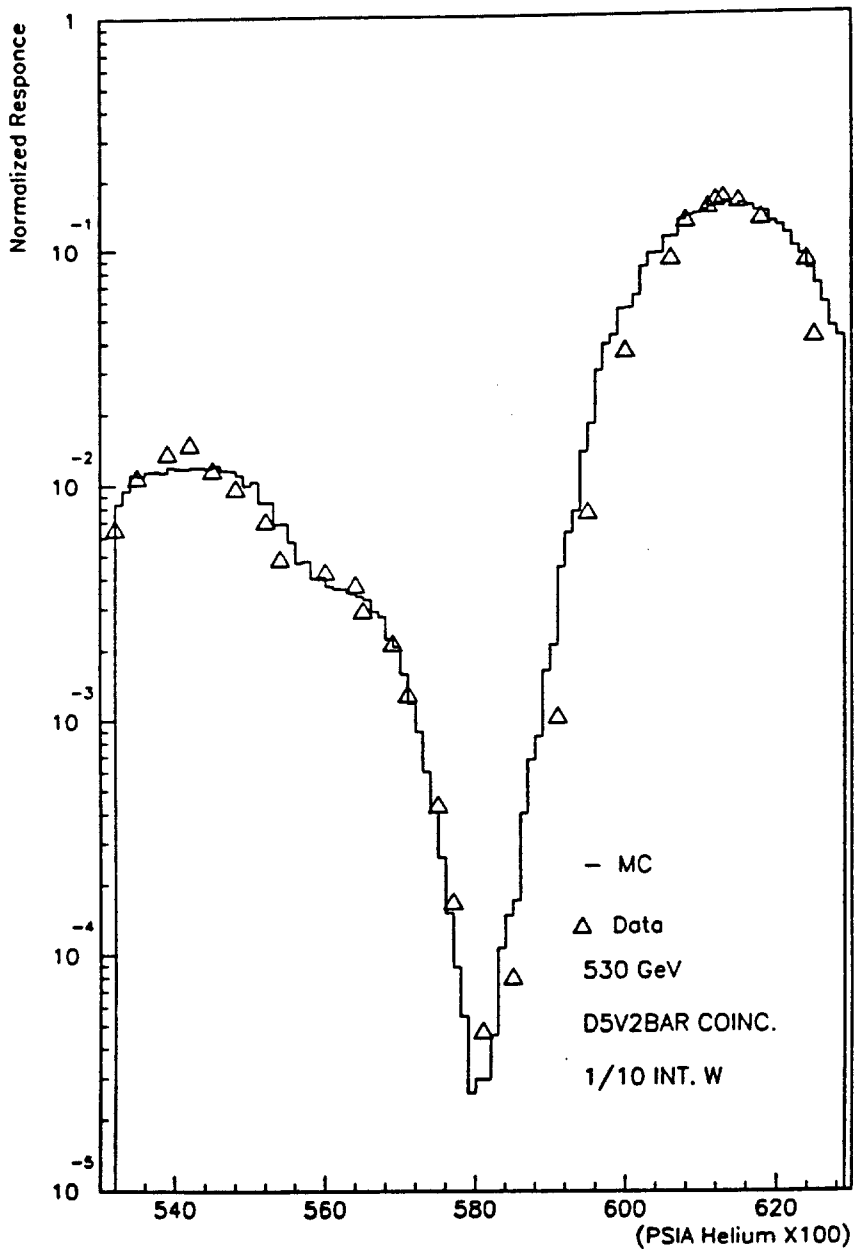

Figure 60: Monte Carlo fit for the $D5\overline{V2}$ W pressure curve at 530 GeV.

The result of the calibration was the following:

$$\text{Beam Protons} \quad (6.15 \pm 0.13) \times 10^{13} \qquad \text{SEM Counts} \quad 8.016 \times 10^{13} \tag{5.9}$$

The error in the proton flux measurement includes both systematic and statistical errors.

5.10. Estimation of Particle Ratios

The particle ratios were determined from the Cherenkov pressure curves. We used the pressure curves with the $D5\overline{V2}$ coincidence requirement in order to have good efficiency and to be less affected by errors. At the -200 and -400 GeV beam energies, we had complete separation of all three particle types (π, K, p), so the particle ratios were measured directly from the pressure curves. The $D5\overline{V2}$ rates have been averaged over the measured points on the pressure peaks and the r.m.s error evaluated was taken as the statistical error.

At $\pm$530 GeV beam energies the π-K separation was not complete, and we used the Monte Carlo simulation program to fit the data and determine the particle ratios and the Cherenkov's efficiency. The 530 GeV data were taken with two different beam configurations (Table 13). The corresponding two sets of input parameters (beam divergence and momentum bite) in the Monte Carlo program were determined by the TURTLE program. Assuming that the beam contained only one type of particle we obtained three different Monte Carlo curves, one for

each particle with the $D5\overline{V2}$ coincidence requirement. Then the three curves were added with variable coefficients in order to fit the $D5\overline{V2}$ data curve. The set of coefficients that gave the best fit was used to determine the relative particle ratios and the overall efficiency. The results of the fits are shown in Fig. 55-60. The particle contents of the beam for each energy and target are listed in Tables 19 and 20.

6. RESULTS AND CONCLUSIONS

In this chapter, I present the measured inclusive single particle cross sections at -200, -400 and ±530 GeV. I also present the energy dependence of π^-, K^- and $\bar{p}$ cross sections for Al and Be and the A-dependence of the three particles at ±530 GeV. Our results are compared with the previous data and the predictions of some theoretical models.

6.1. Calculations of Cross Sections

The invariant cross sections presented here are for reactions of the form p $A \rightarrow c$ X and are calculated from:

$$\begin{aligned} E\frac{d^3\sigma(p,c)}{dp^3} &= \frac{E}{p^2}\frac{d^3\sigma(p,c)}{dpd\Omega} \\ &= \frac{Y(p,c)}{F(p)}\frac{E}{p^3}\frac{A}{\Delta\Omega(\Delta p/p)N_0\rho l}\frac{l}{\lambda_A^p}\frac{1}{f_A^c} \end{aligned} \tag{6.1}$$

where $\Delta\Omega(\Delta p/p)$ is the acceptance, N_0 is Avogadro's number, ρ is the target's density, l is the target's length, $F(p)$ is the proton flux, A is the atomic number of the target material, E, p are the energy and momentum of the produced particle c in the laboratory frame, f_A^c is the target production efficiency for secondary c and λ_A^p is the proton's interaction length for the specific target. The normalized yield Y($p \rightarrow c$), as was mentioned in the previous chapter, was corrected for SEM

calibration, absorption and decays in the beam. The last term $\frac{l}{\lambda_A^T}\frac{1}{f_A^c}$ accounts for absorption in the target. The corrections mentioned above were relatively small.

Table 21 lists the the value of $A/\rho l N_0$ for each target used.

TABLE 21				
MATERIAL	LENGTH cm	A gm	ρ gm/cm^3	$A/N_0\rho l$ cm^2
Be	7.34	9.01	1.85	1.103×10^{-24}
Al	3.06	26.98	2.70	5.423×10^{-24}
Al	30.54	26.98	2.70	5.433×10^{-25}
W	0.95	183.85	19.30	1.653×10^{-23}

TABLE 21: Values of $A/\rho l N_0$ for each target.

6.2. Systematic Errors

The statistical errors in the measured cross sections are relatively small. Systematic errors are more significant. The data were taken over a period of several months, whenever beam became available during the run of E706, and they were therefore susceptible to changes in the properties of the beam extracted from the Tevatron. The largest systematic error comes from drifts of the SEM calibration with time which is estimated to be about 6% to 7%. The systematic errors in the calculations of the acceptances are estimated to be about 5%. In addition to the systematic errors quoted, we estimate an overall normalization uncertainty of

±20% for all the cross sections. In the following tables I quote only the statistical errors.

6.3. Cross Sections at -200 and -400 GeV

The calculated invariant cross sections for π^-, K^-, and $\bar{p}$ from Al and W targets at -200 and -400 GeV are listed in Table 22. I also list the K^-/π^- and $\bar{p}/\pi^-$ ratios in Table 23. These ratios are relative measurements that are not subject to most of the systematic errors. The quoted errors are statistical, only.

TABLE 22					
			$Ed^3\sigma/dp^3$ mb/GeV^{2}sr		
p GeV	$< p_T >$ MeV	Target Material	π^-	K^-	$\bar{p}$
-200	40	Al	55 ± 1	4.1 ± 0.2	0.86 ± 0.05
-200	40	W	301 ± 5	20.4 ± 0.7	4.1 ± 0.2
-400	80	Al	5.1 ± 0.1	0.2 ± 0.1	0.026 ± 0.002
-400	80	W	20.2 ± 0.5	0.76 ± 0.02	0.17 ± 0.02

TABLE 22: Calculated invariant differential cross sections for Al and W at -200 and -400 GeV.

TABLE 23				
p GeV	$< p_T >$ MeV	Target Material	K^-/π^- %	$\bar{p}/\pi^-$ %
-200	40	Al	6.24 ± 0.3	1.29 ± 0.07
-200	40	W	5.44 ± 0.3	1.17 ± 0.06
-400	80	Al	4.0 ± 0.2	0.47 ± 0.05
-400	80	W	3.4 ± 0.20	0.78 ± 0.06

TABLE 23: Particle ratios for Al and W at -200 and -400 GeV.

6.4. Cross Sections at ±530 GeV

Tables 24 and 25 list the particle ratios at -530, and +530 GeV respectively. The positive 530 GeV invariant cross sections are listed in Table 26 and the negative ones in Table 27. The positive 530 GeV cross sections correspond to 1.4 mrad production angle (p_T=720 MeV) and the negative 530 cross sections correspond to 0° production angle (p_T=0 MeV). The errors quoted are statistical ones, only.

TABLE 24				
p GeV	$< p_T >$ MeV	Target Material	K^-/π^- %	$\bar{p}/\pi^-$ %
-530	106	Be	3.3 ± 0.3	0.26 ± 0.03
-530	106	Al	3.0 ± 0.3	0.21 ± 0.02
-530	106	W	2.7 ± 0.3	0.20 ± 0.02

TABLE 24: Particle ratios at -530 GeV.

TABLE 25				
p GeV	$< p_T >$ MeV	Target Material	π^+/p %	K^+/p %
530	720	Be	7.6 ± 0.3	1.7 ± 0.3
530	720	Al	7.8 ± 0.4	1.6 ± 0.2
530	720	W	7.2 ± 0.4	2.1 ± 0.2

TABLE 25: Particle ratios at 530 GeV

TABLE 26					
			$Ed^3\sigma/dp^3$ mb/GeV^{2}sr		
p GeV	$< p_T >$ MeV	Target Material	π^+	K^+	p
530	720	Be	0.45 ± 0.02	0.10 ± 0.02	5.7 ± 0.2
530	720	Al	0.77 ± 0.04	0.16 ± 0.02	10.9 ± 0.3
530	720	W	2.1 ± 0.1	0.64 ± 0.09	30.4 ± 0.9

TABLE 26: Invariant cross sections at 530 GeV.

TABLE 27					
			$Ed^3\sigma/dp^3$ mb/GeV^{2}sr		
p GeV	$< p_T >$ MeV	Target Material	π^-	K^-	$\bar{p}$
-530	106	Be	0.48 ± 0.01	0.015 ± 0.002	0.0013 ± 0.0002
-530	106	Al	0.73 ± 0.02	0.019 ± 0.003	0.0016 ± 0.0002
-530	106	W	2.58 ± 0.07	0.073 ± 0.008	0.0052 ± 0.0007

TABLE 27: Invariant cross sections at -530 GeV.

6.5. Energy Dependence

The invariant cross sections for $p \rightarrow \pi^-$ X, $p \rightarrow K^-$ X and $p \rightarrow \bar{p}$ X for the Al and W targets are plotted as a function of Feynman x in Fig. 61, 62 and 63. The agreement with the data of Barton et al.[24] at 100 GeV beam momentum is generally good (Fig. 64, 65, 66). For this comparison we have to note that Barton's data are taken at a fixed p_T of 0.3 GeV. Our negative data are taken at a fixed production angle of 0° and with large p_T acceptance (see Chapter 5). The difference due to the different p_T is estimated to be a factor of 1.41-1.46 for the π^- data, and a factor of 1.32-1.36 for K^- and $\bar{p}$ data.

I also plotted the K^-/π^- and $\bar{p}/\pi^-$ ratios as a function of secondary momentum for the Al and W targets (Fig. 67, 68).

6.6. A-Dependence

We were only able to measure the A-dependence for ±530 GeV. The invariant cross sections were fitted to the empirical form:

$$E\frac{d^3\sigma}{dp^3} = \sigma_0 A^\alpha \tag{6.2}$$

The fits for the negative 530 GeV data are shown in Fig. 69 and the fits for the positive 530 GeV in Fig. 70. The results of all the fits are given in Table 28. The errors quoted are only statistical.

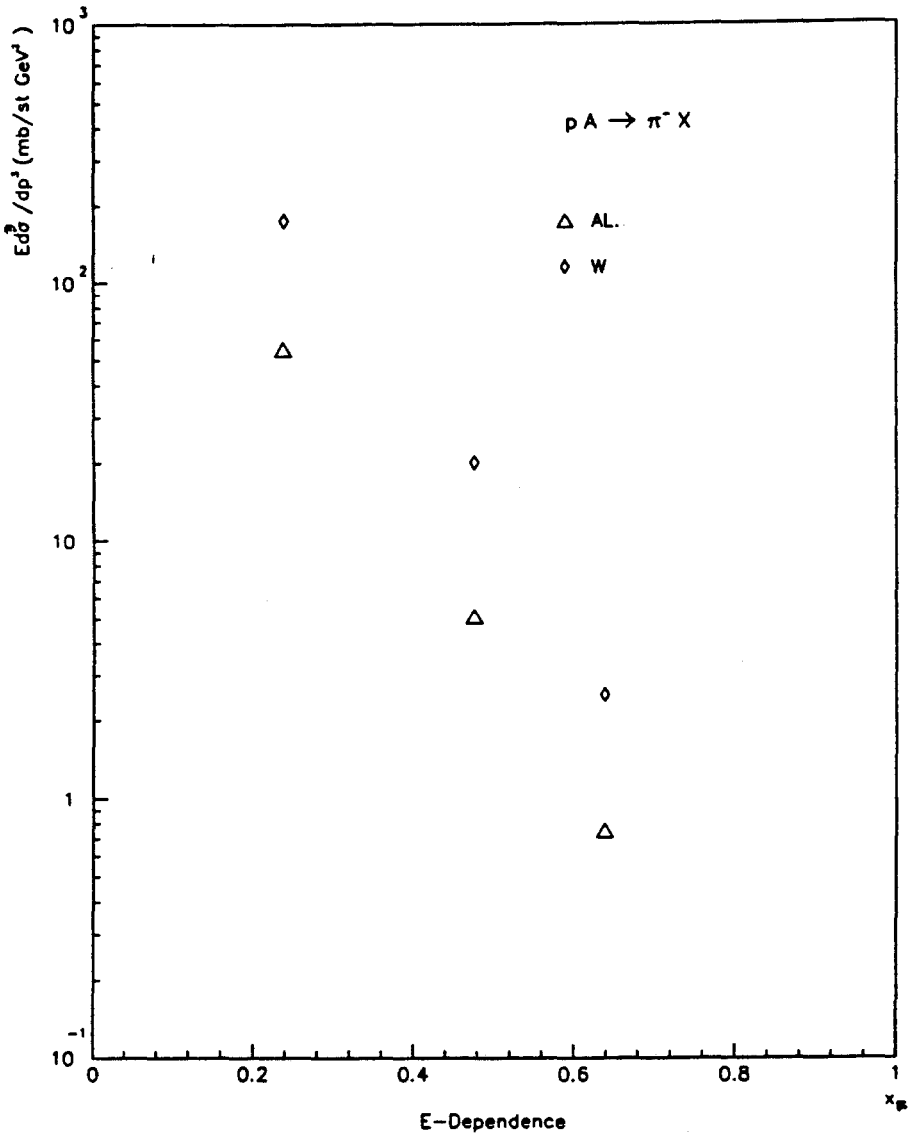

Figure 61: The invariant differential cross section for p $A \rightarrow \pi^-$ X plotted as a function of x_F.

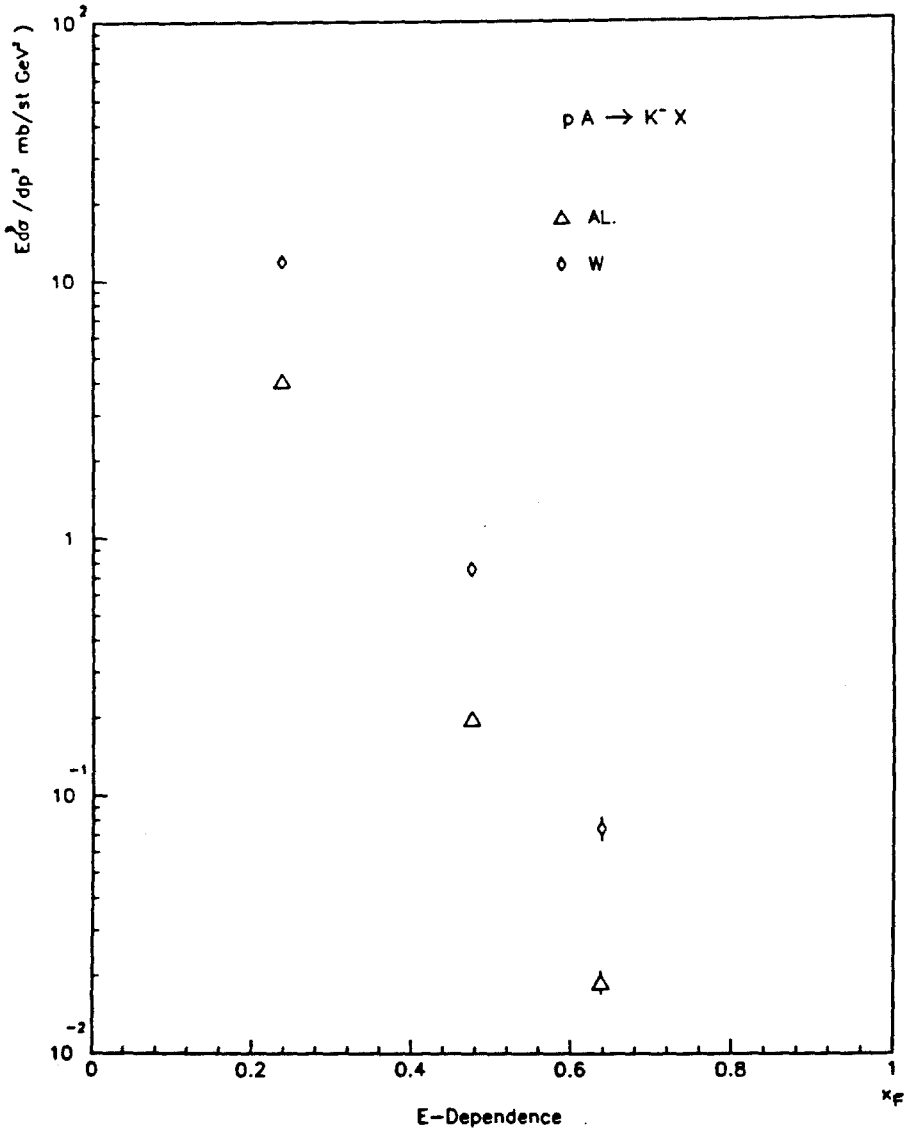

Figure 62: The invariant differential cross section for p $A \rightarrow K^-$ X plotted as a function of x_F.

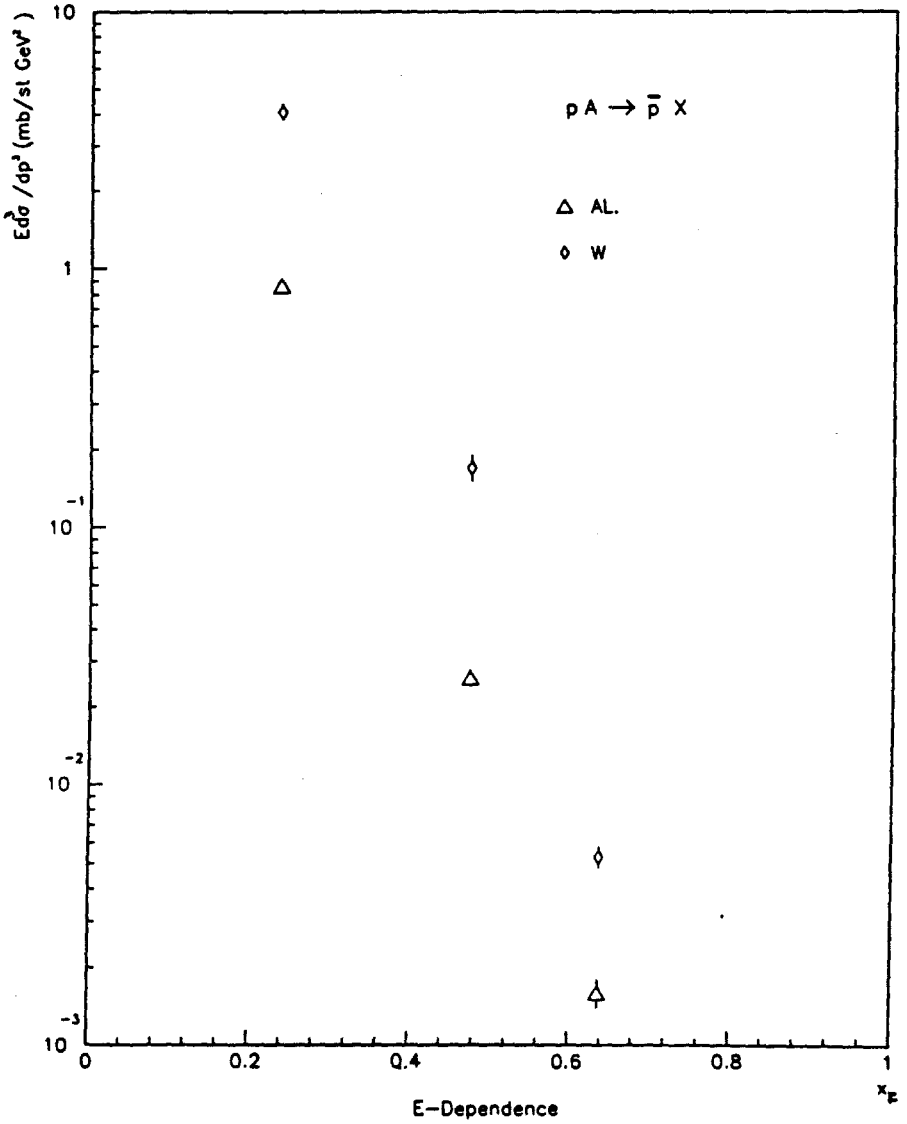

Figure 63: The invariant differential cross section for p $A \rightarrow \bar{p}$ X plotted as a function of x_F.

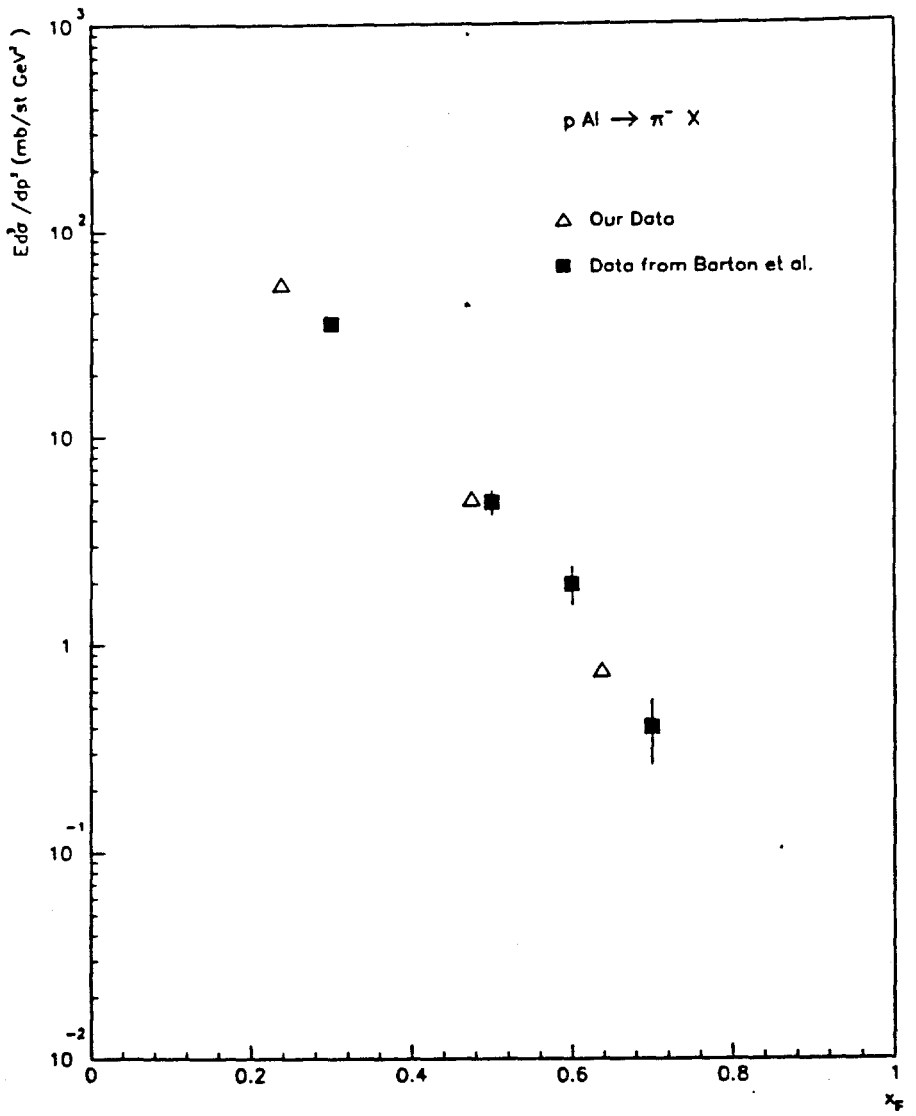

Figure 64: The measured invariant differential cross sections for p Al→ π^- X compared with the ones from Barton et al.[24] at 100 GeV for various values of x_F.

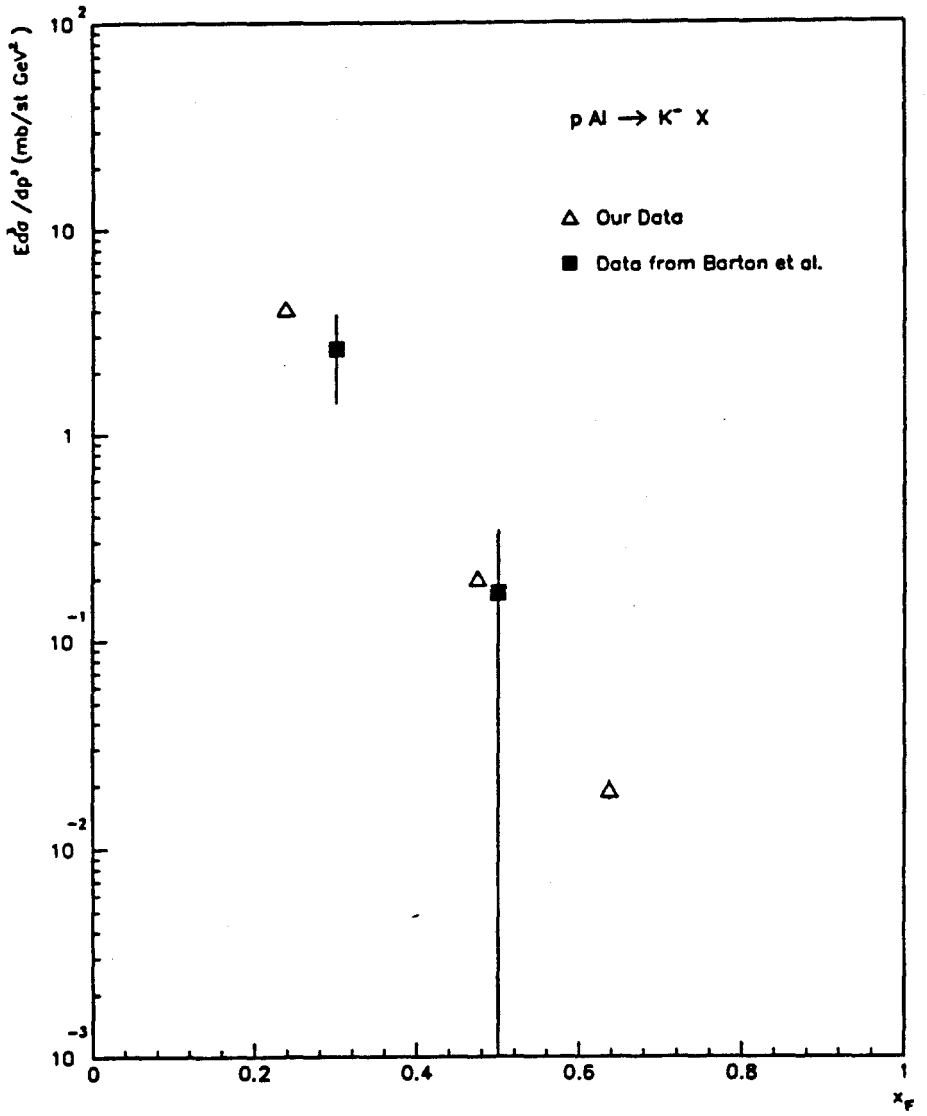

Figure 65: The measured invariant differential cross sections for p Al→ K^- X compared with the ones from Barton et al.[24] at 100 GeV for various values of x_F.

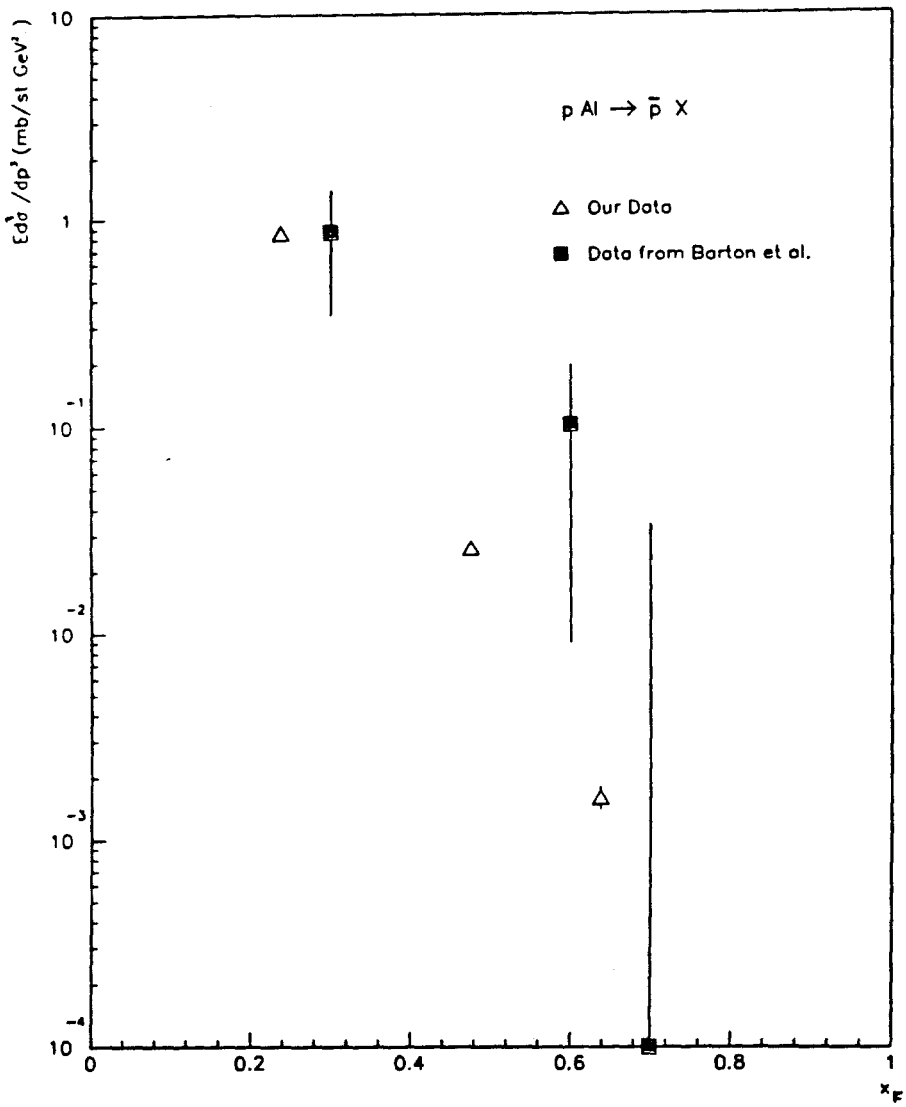

Figure 66: The measured invariant differential cross sections for p Al→ $\bar{p}$ X compared with the ones from Barton et al.[24] at 100 GeV for various values of x_F.

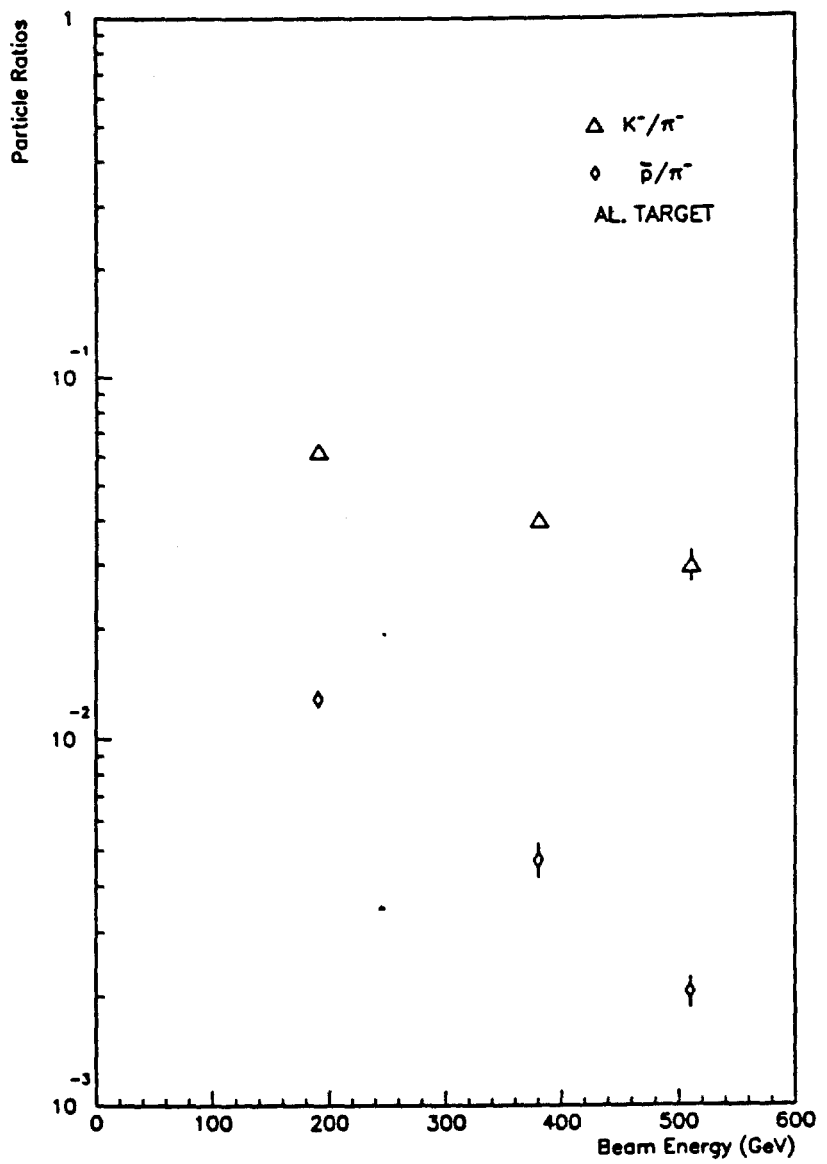

Figure 67: Particle ratios for Al as a function of the secondary momentum.

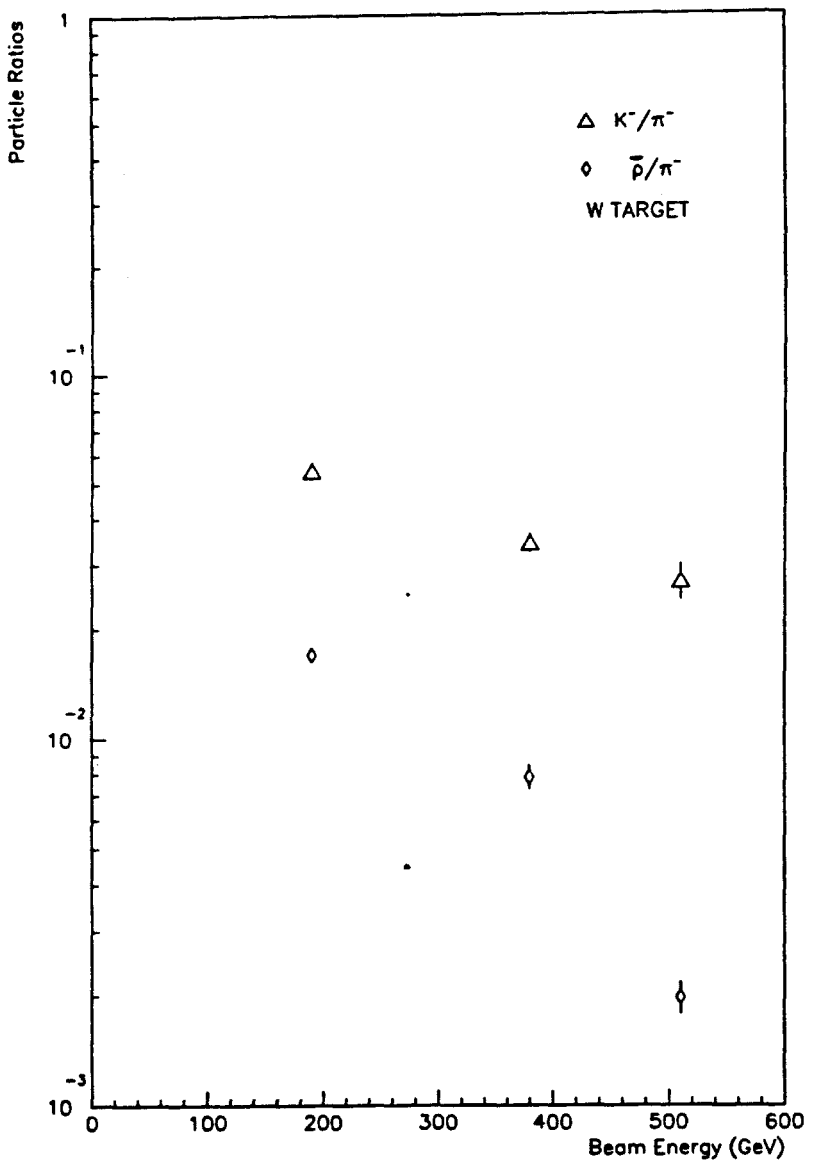

Figure 68: Particle ratios for W as a function of the secondary momentum.

TABLE 28		
Particle	σ_0 (mb/GeV^2sr)	α
π^+	0.14 ± 0.01	0.53 ± 0.02
π^-	0.134 ± 0.005	0.56 ± 0.02
K^+	0.022 ± 0.007	0.64 ± 0.08
K^-	0.0039 ± 0.0009	0.55 ± 0.05
p	1.82 ± 0.1	0.54 ± 0.02
$\bar{p}$	0.00038 ± 0.00009	0.49 ± 0.06

TABLE 28: Parameters obtained by fitting the invariant differential cross sections to the form $\sigma_0 A^\alpha$

Figures 71, 72 and 73 show general agreement of our 800 GeV data with earlier measurements at 24 GeV[22] and 100 GeV[24].

6.7. Conclusions

We measured for the first time the A-dependence at ±530 GeV for $\pi^\pm$, $K^\pm$ p, $\bar{p}$ production and for 800 GeV incident protons. The negative data were taken at 0 degrees production angle and the positive at 1.4 mrad production angle (p_T=0.7 GeV). We also measured the x_F-dependence for π^-, K^- and $\bar{p}$ production at 0 degrees.

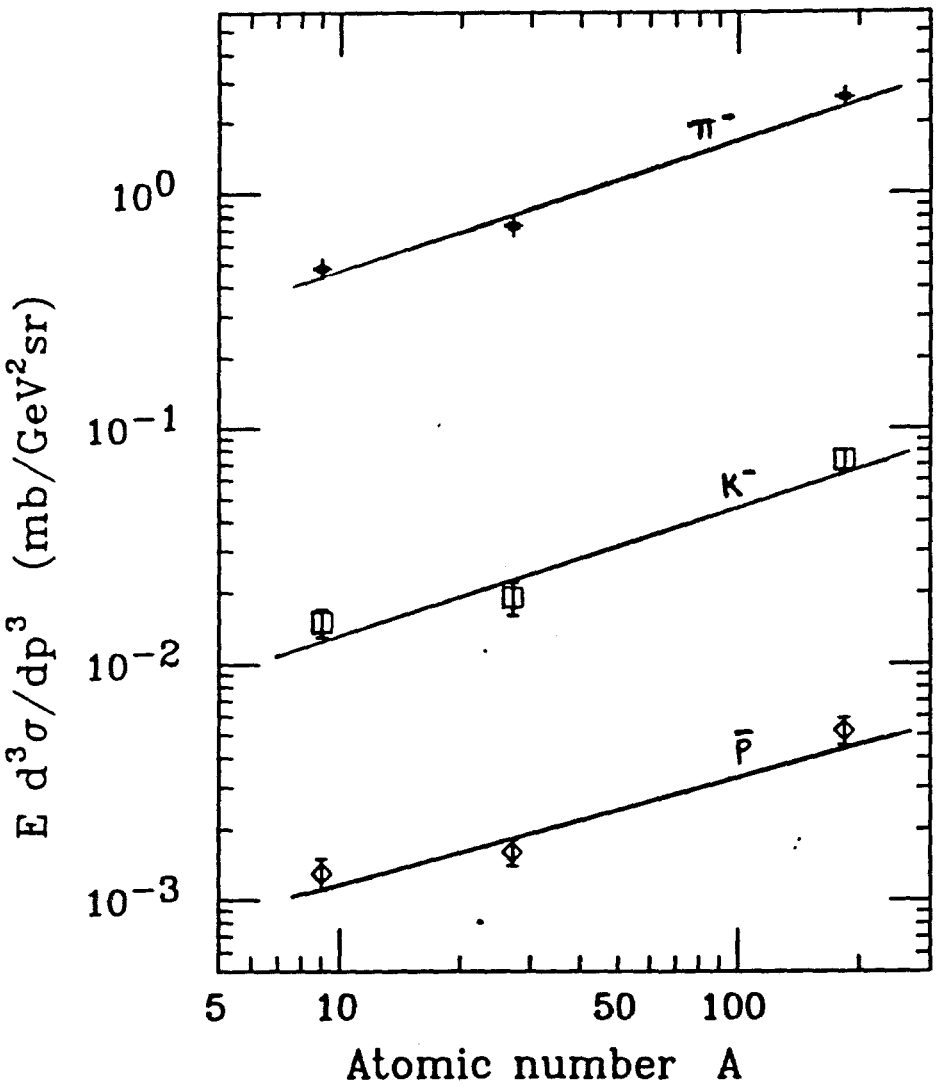

Figure 69: Invariant differential cross sections for negative particles with fits of the form $\sigma_0 A^\alpha$.

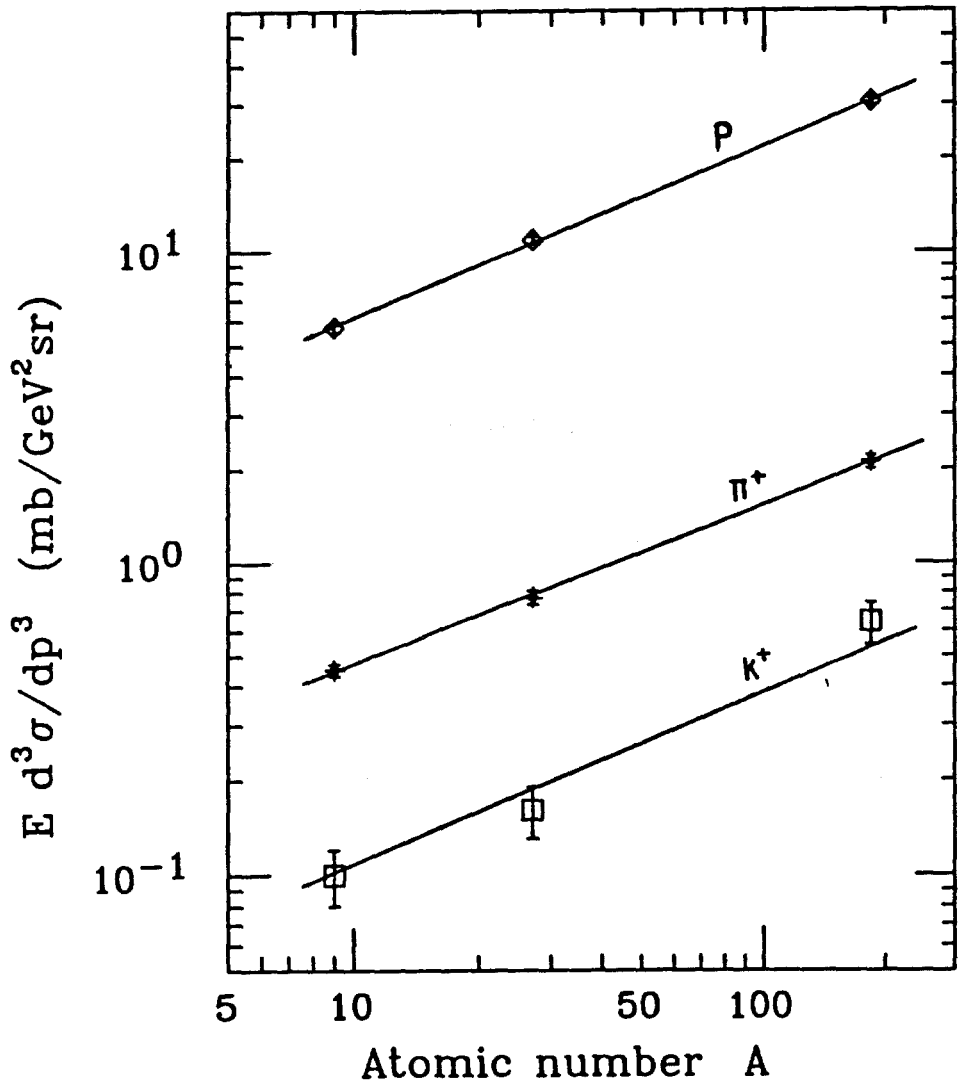

Figure 70: Invariant differential cross sections for positive particles with fits of the form $\sigma_0 A^\alpha$.

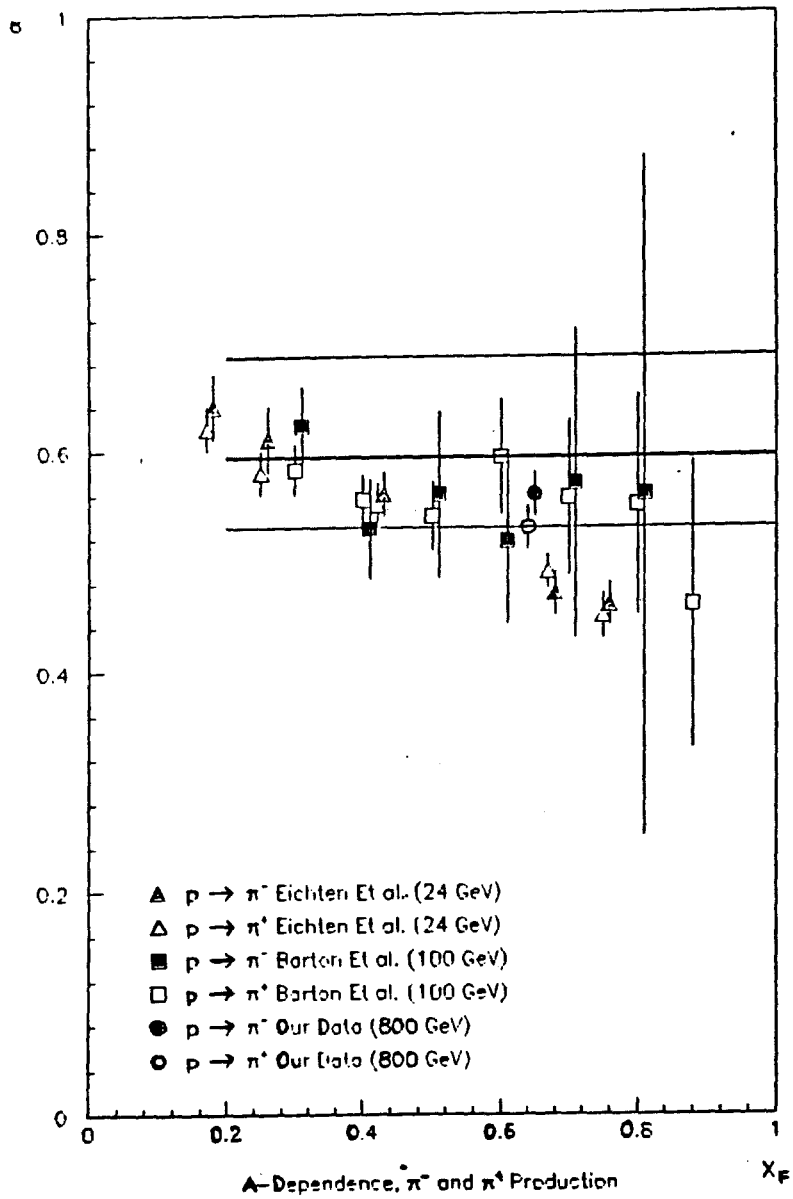

Figure 71: A-dependence: π^-, π^+ production. The middle thick line represents the theoretical prediction of additive quark model. The upper and lower thin lines represent the theoretical predictions with two different sets of input parameters.

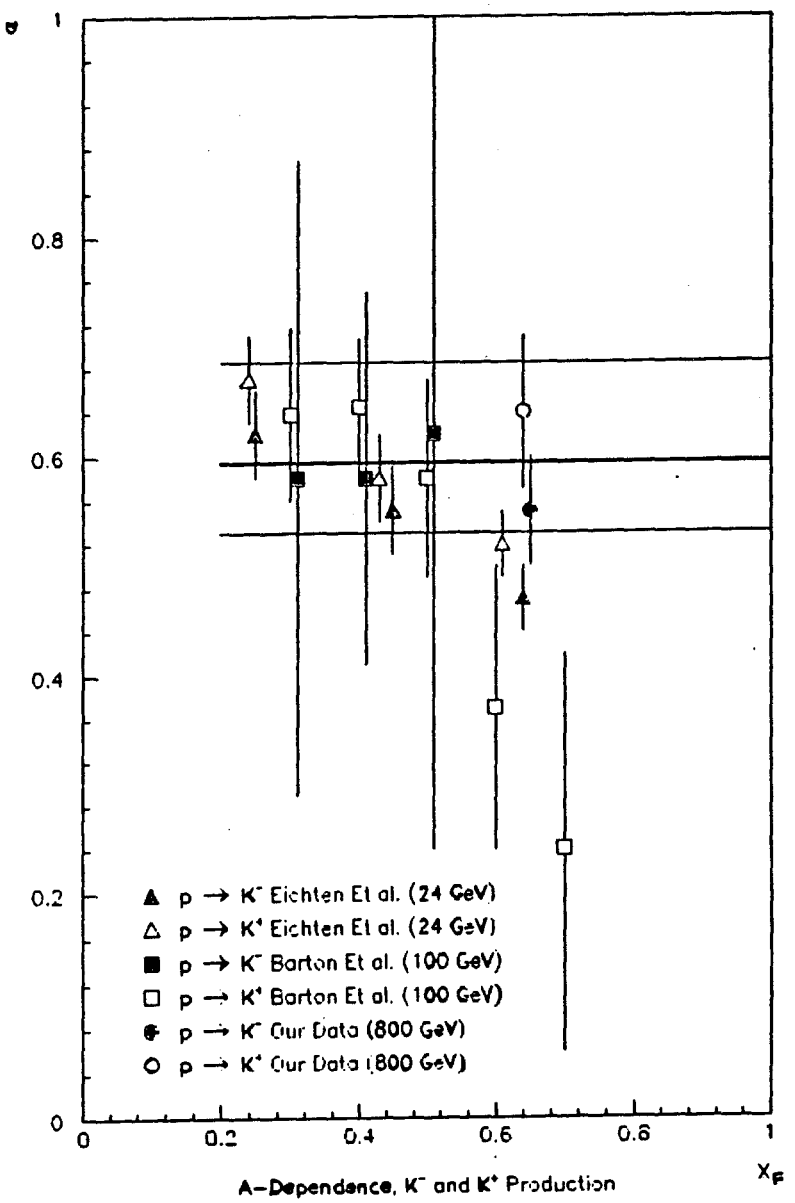

Figure 72: A-dependence: K^-, K^+ production. The middle thick line represents the theoretical prediction of additive quark model. The upper and lower thin lines represent the theoretical predictions with two different sets of input parameters.

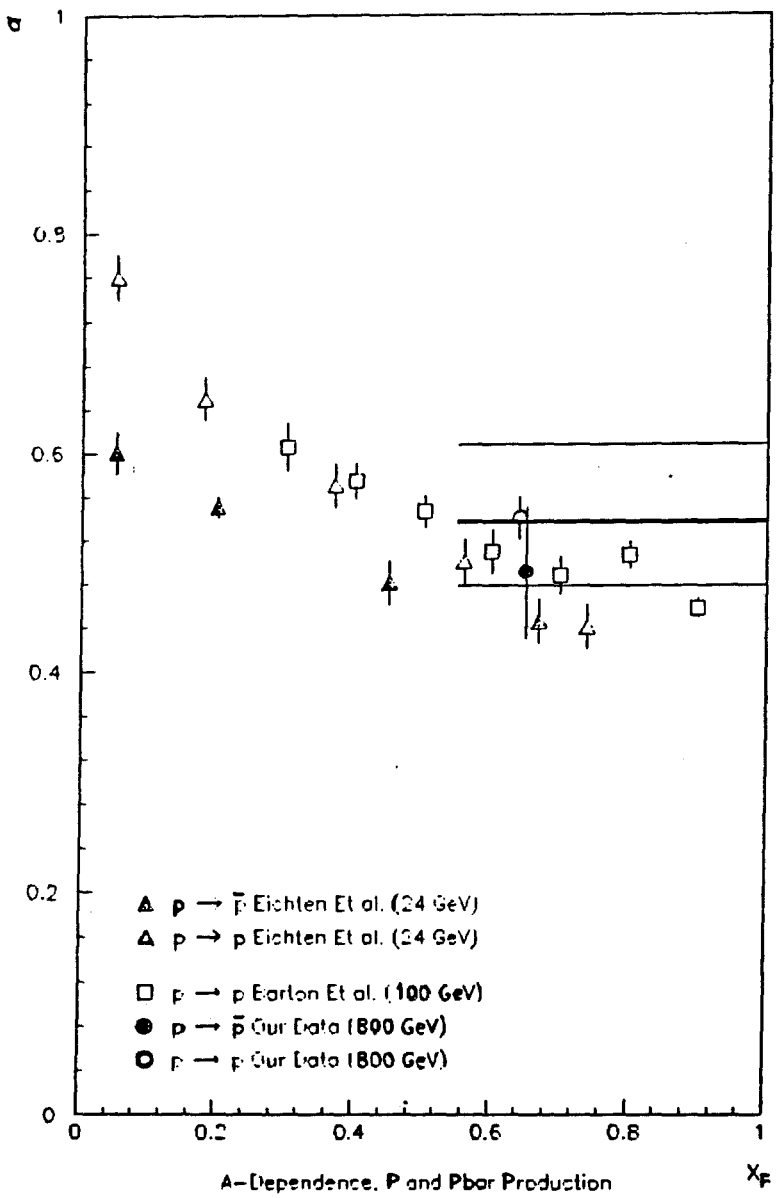

Figure 73: A-dependence: p, $\bar{p}$ production. The middle thick line represents the theoretical prediction of additive quark model. The upper and lower thin lines represent the theoretical predictions with two different sets of input parameters.

At large values of $\sqrt{s}$ like ours we would expect the hypothesis of limiting fragmentation[27] i.e that the invariant cross sections approach a limiting value that is a function of p_T and Feynman x. The data of Barton et al[24] at 100 GeV were compared with the data of Eichten et al. at 24 GeV and were found to be slightly lower. We compared our measured negative cross sections on Al with the ones from Barton et al. at 0.3 GeV p_T which was the smallest p_T available for comparison over the x_F region. Since the p_T is not the same we could not test the hypothesis of limiting fragmentation at our energies but we could see that our cross sections at 800 GeV show the same qualitative behavior with x_F as the cross sections of Barton, et al. at 100 GeV with the possible exception of the cross section for $\bar{p}$ production where the errors are rather large for a conclusion.

The our measured A-dependencies are in very good agreement with the ones measured at 100 and 24 GeV and at 0.3 GeV p_T (Fig. 71-73). The only exception is the A-dependence of the K^+ production at 0.7 GeV p_T where the exponent α is rather larger than the ones measured at different energies and for other particles, implying that the nuclei are more transparent in the K^+. It would be interesting to repeat this measurement as well as measure the A-dependence for the strange particles in other values of x_F. The higher value of the parameter α for protons compared with the one for $\bar{p}$ can be explained in the framework of the formation zone model[69]. Because absorption cross sections for antiquarks and $\bar{p}$ are larger than those for quarks and p's, the nuclei absorb with larger probability the intermediate states producing antibaryons, than baryons. The model predicts that at higher energies the final state absorption effects (and therefore the difference in α for p and $\bar{p}$ production) should vanish.

Our data for the A-dependence are compared with the predictions of the additive quark model[12],[13] (Fig. 71, 72, 73) which assumes that the hadrons produced in the projectile fragmentation region are dominated by the products of hadronization (fragmentation and recombination) of the leading quarks from the projectile. Basic parameters in this model are the total inelastic cross sections for h-A and q-A collisions, where h is a hadron and q is the constituent quark. Although the h-A cross sections were measured experimentally the q-A cross sections had to be calculated adding some uncertainty to the model predictions. The values of the exponent α predicted from the model depend on the choice of a pair of nuclei A_1 and A_2. The middle line in our figures (Fig. 71, 72, 73) corresponds to a χ^2 fit of the model predictions to a power law for five A values. The upper line corresponds to a model prediction for A_1=12 A_2=27, while the lower line corresponds to the prediction for A_1=118, A_2=207. The agreement of our data to the model predictions appears to be good for all the secondary particles measured.

The accuracy of our data does not permit definite conclusions to be drawn at this time. This study is going to be continued during the next fixed target run of the Tevatron. At this time a larger selection of nuclei will be used; these will be inserted into the proton beam on successive pulses of the accelerator, eliminating most of the systematical errors. We also plan to study the A-dependence at different Feynman x for both positive and negatives secondaries.

REFERENCES

1. L.D.Landau and I. Ya. Pomeranchuk, Doklady Acad. Nauk. SSSR, 92 (1953) 535.
2. E.L. Feinberg, Phys. Reports 5 (1972) 237.
3. W. Busza, Proceedings XV International Symposium on Multiparticle Dynamics, Lund, 1984, pg. 66.
4. N. N. Nikolaev, Sov. J. Part. Nucl. 12, 63 (1981).
5. G. Berlad, A. Dar, and G. Eilam, Phys. Rev. D 13, 161 (1976).
6. K. Gottfried, Phys. Rev. Lett. 32, 957 (1974).
7. C. Quigg, "Gauge Theories of the Strong, Weak, and Electromagnetic Interactions", Frontiers in Physics. The Benjamin-Cummings Publishing Company, Inc., 1983.
8. N. N. Nikolaev and A. Ya. Ostapchuck, CERN Report TH. 2575-CERN, 1978.
9. A. Cappella and J. Tran Thanh Van, Phys. Lett. 93*B*, 146 (1980).
10. A. Cappela and J. Tran Thanh Van, Z. Phys. C 10, 249 (1981).
11. V. V. Anisovich, Yu. M. Shabelski and V. M. Shekhter, Nucl. Phys. *B*133 (1978), 477.
12. A. Dar and F. Takagi, Phys. Rev. Lett. 44 (1980), 768.
13. F. Takagi, Prog. Theor. Phys. 65, 1350 (1981).
14. A. Bialas and E. Bialas, Phys. Rev. *D*20 (1979), 2854.

15. G. Berlad, A. Dar and G. Eilam, Phys. Rev. *D22* (1980), 1547.

16. F. Takagi, Z. Phys. C 28, 439 (1985).

17. I. Otterlund, Nucl. Phys. *A418*, 87c, (1984).

18. K. G. Gulamov, Proceedings XVI International Symposium on Multiparticle Dynamics Seewinkel, Austria 1986 pg. 751.

19. S. Fredriksson, G. Eidam and G. Berlad, Phys. Rep. 144, 187 (1987)

20. W. Busza, Acta Phys. Polon. *B8*, 333 (1977)

21. W. F. Baker et al., Phys. Lett. 51*B*, 303 (1974); Fermilab Report 78/79-Exp. (1978)

22. T. Eichten et al., Nucl. Phys. *B44*, 333 (1978).

23. H. W. Atherton et al., CERN Report 80 – 07, SPS division (1980).

24. D. S. Barton et al., Phys. Rev. D27, 2580 (1983).

25. C. De Marzo et al. Phys. Rev. D26 1019 (1982)

26. K. Abe et al., Phys. Lett. B200, 266 (1988)

27. J. Benecke et al, Phys. Rev. 188, 2159 (1961)

28. D. Johnson, L. Spires, R. Zimmermann, and A. Nallenweg, "Experimental Areas Beamline Control System Operator's Guide", (2d Rev.), Fermilab Publication (1983).

29. V. Frohne, "A Short Guide to The EPICS Beam Line Control System", Fermilab Publication (1985).

30. S. Butala "Meson West Interlock System", Internal Fermilab Memo, May 5, 1985.

31. S. Butala "Meson West Intelock Update" Internal Fermilab Memo, Feb. 3, 1987.

32. S. Butala "MWest Radiation Safety", Internal Fermilab Memo, Feb. 14, 1986.

33. S. Butala "MWest Experimental Hall Shielding", Internal Fermilab Memo. Sep. 7, 1985.

34. S. Butala "MWest Shield Upgrade for E706/672" Internal Fermilab Memo. May 9, 1988.

35. R. Tokarek "Primary Beam Dumping Modes in the M-West Dump". Internal Fermilab Memo, Jan. 29, 1987.

36. R. Tokarek "Suggested Operating Conditions for MW Positive Secondary Running Mode", Internal Fermilab Memo, Dec. 29, 1987.

37. "AGREEMENT E-706", Internal E-706 Memo, E706-069, 1983.

38. E. Engels, et al., NIM, A253, 523, (1987).

39. E. Engels, et al., NIM, A279, 272, (1989).

40. F. Lobkowicz, et al., NIM, A235, 332, (1985).

41. J. Huston, et al., Paper Submitted to XXIV International Conference on High energy Physics, Munich (1988).

42. C. Bromberg, E-706 Internal Memo, E706-094.

43. P. Lukens, K. Ruddick, E-706 Internal Memo, E706-141.

44. W. Baker, D. Carey and R. Tokarek, "MWest Beam Upgrade", Internal Fermilab Memo, Jan 26, 1989.

45. S. Butala, "Pinhole Collimators at NE and MW", Internal Fermilab Memo, Aug. 26, (1988).

46. D. C. Carey, "The Optics of Charged Particle Beams", Harwood Academic Publishers, New York, 1987

47. H. Vollnik, "Optics of Charged Particles", Academic Press, 1987.

48. K. L. Brown, F. Rothacker, D. C. Carey and C. Iselin, "TRANSPORT Appendix", Fermilab PM-0008 (1977)

49. K. L. Brown, "A First and Second Order Matrix Theory for the Design of Beam Transport Systems and Charged Particle Spectrometers", SLAC-75 (1967).

50. K. L. Brown, F. Rothacker, D. C. Carey and C. Iselin, "TRANSPORT-A Computer Program for Designing Charged Particle Transport Systems", CERN-80-04 (1980).

51. D. C. Carey, "New Features in TRANSPORT", Fermilab TM-1064, (1981).

52. D. C. Carey, K. L. Brown, and C. Iselin, "DECAY TURTLE, a Computer Program for Simulating Charged Particle Beam Transport System, including Decay Calculations", SLAC-246 (1982).

53. A. J. Malensek, "Empirical Formula for Thick Target Particle Production", Fermilab FN-341 (1981).

54. A. J. Malensek, "Addenum to Empirical Formula for Thick Target Particle Production", Fermilab FN-341A (1982).

55. T. Toohig, "Fermilab Magnets, Power Supplies, and Auxiliary Devices: Technical Data", Fermilab TM-632 (1975).

56. E. C. Sedman, "Design of Beam Transport Systems", MPS Internal Report 62-23 (1962).

57. A. S. Carrol et al., Phys. Lett. 80*B*, 319 (1979)

58. P. A. Cherenkov, Docl. Akad. Nauk. SSSR 2,451 (1934), S. I. Vavilov, Docl. Akad. Nauk. SSSR 2,457 (1934); ibid (1956).

59. I. E. Tamm, I. M. Frank, Dokl. Akad. Nauk. SSSR 14,107 (1937).

60. V. L. Ginsburg, Zh. Eksp. Teor. Fiz 10(6), 589 (1940).

61. M. Benot, J. Litt and R. Meunier, NIM 105, 431 (1972).

62. D. D. Yovanovitch et al., NIM 100, 545 (1972).

63. J. V. Jelley, "Cherenkov Radiation and its Applications", London:Pergamon (1958).

64. V. P. Zrelov, "Cherenkov Radiation in High-Energy Physics", Moscow: Atomizdat. (1968).

65. C. R. Mansfield and E. R. Peck, J. Opt. Soc. Am. 59, 199 (1969).

66. D. Dalgarno and A. E. Kingston, Proc. Phys. Soc. (London) 259*A*, 424 (1960).

67. B. Rossi, K. Greisen, Rev. Mod. Phys. 13, 240 (1941).

68. K. G. Dedrick, Phys. Rev. 87, 891 (1952).

69. A. Bialas, Z. Phys. C 26, 301-306 (1984).

70. A. Bialas and W. Czyz, Nucl. Phy. *B*194, 21 (1982).